

Lappeenrannan teknillinen korkeakoulu
Lappeenranta University of Technology

Arttu Reunanen

Experimental and Numerical Analysis of Different Volute in a Centrifugal Compressor

*Thesis for the degree of Doctor of Science (Technology)
to be presented with due permission for public
examination and criticism in the Auditorium of the
Student Union House at Lappeenranta University of
Technology, Lappeenranta, Finland on the 12th of
December, 2001, at 1 p.m.*

Acta Universitatis
Lappeenrantaensis

118

ISBN 951-764-607-0

ISSN-1456-4491

Lappeenrannan teknillinen korkeakoulu

Digipaino 2001

ABSTRACT**Arttu Reunanen****Experimental and Numerical Analysis of Different Volute in a Centrifugal Compressor**

Lappeenranta 2001

150 p.

Acta Universitatis Lappeenrantaensis 118

Diss. Lappeenranta University of Technology

ISBN 951-764-607-0, ISSN-1456-4491

In a centrifugal compressor the flow around the diffuser is collected and led to the pipe system by a spiral-shaped volute. In this study a single-stage centrifugal compressor with three different volutes is investigated. The compressor was first equipped with the original volute, the cross-section of which was a combination of a rectangle and semi-circle. Next a new volute with a fully circular cross-section was designed and manufactured. Finally, the circular volute was modified by rounding the tongue and smoothing the tongue area. The overall performance of the compressor as well as the static pressure distribution after the impeller and on the volute surface were measured. The flow entering the volute was measured using a three-hole Cobra-probe, and flow visualisations were carried out in the exit cone of the volute. In addition, the radial force acting on the impeller was measured using magnetic bearings.

The complete compressor with the circular volute (inlet pipe, full impeller, diffuser, volute and outlet pipe) was also modelled using computational fluid dynamics (CFD). A fully 3-D viscous flow was solved using a Navier-Stokes solver, Finflo, developed at Helsinki University of Technology. Chien's $k-\varepsilon$ model was used to take account of the turbulence.

The differences observed in the performance of the different volutes were quite small. The biggest differences were at low speeds and high volume flows, i.e. when the flow entered the volute most radially. In this operating regime the efficiency of the compressor with the modified circular volute was about two percentage points higher than with the other volutes. Also, according to the Cobra-probe measurements and flow visualisations, the modified circular volute performed better than the other volutes in this operating area.

The circumferential static pressure distribution in the volute showed increases at low flow, constant distribution at the design flow and decrease at high flow. The non-uniform static pressure distribution of the volute was transmitted backwards across the vaneless diffuser and observed at the impeller exit. At low volume flow a strong two-wave pattern developed into the static pressure distribution at the impeller exit due to the response of the impeller to the non-uniformity of pressure.

The radial force of the impeller was the greatest at the choke limit, the smallest at the design flow, and moderate at low flow. At low flow the force increase was quite mild, whereas the increase at high flow was rapid. Thus, the non-uniformity of pressure and the force related to it are strong especially at high flow. The force caused by the modified circular volute was weaker at choke and more symmetric as a function of the volume flow than the force caused by the other volutes.

Keywords: centrifugal compressor, volute, computational fluid dynamics, radial force

UDC 621.515

PREFACE

I have done this study while working as a researcher at Lappeenranta University of Technology in 1998 - 2001. The study is a part of the high speed technology research program, which has been going on in the Laboratory of Fluid Dynamics of the Department of Energy Technology since 1980.

I wish to express my sincere thanks to professor Jaakko Larjola, my supervisor and the leader of the high speed technology research group. His continuous enthusiasm, guidance and encouragement have been vital for this work.

I wish to thank all my colleagues and the team members of the high speed technology research group for indispensable assistance. In particular the contribution of M.Sc. Teemu Turunen-Saaresti to the numerical calculations has been very important. Also the encouragement and numerous comments of Dr. Jari Backman have been of significant help. I thank M.Sc. Hannu Esa and Mr. Jukka Lattu for their help in the designing and manufacturing of the volute. I express my thanks also to the laboratory staff, Petri Pesonen, Ilpo Taipale and Erkki Nikku, for their effort in assembling the instrumentation and the test equipment.

I would like to express my thanks also to professor Timo Siikonen from the Laboratory of Applied Thermodynamics, Helsinki University of Technology for his fruitful co-operation with the Finflo flow solver. Thanks are also due to M.Sc. Harri Heiska for the assistance with the grid generation.

Special thanks are due to the reviewers, professor Manfred Rautenberg of Hannover University and associate professor Abraham Engeda of Michigan State University, for their valuable comments.

This research work has been funded by High Speed Tech Oy Ltd, Sundyne Corporation, the National Technology Agency (Tekes) and the Research Foundation of Lappeenranta University of Technology. The computer resources for the numerical work have been provided by CSC - Scientific Computing Ltd. The financial support is gratefully acknowledged.

The dearest thanks belong to Hanna. She has encouraged and supported me in so many ways during this work that short words like these cannot express my feelings and gratitude.

Lappeenranta, November 2001.

Arttu Reunanen

CONTENTS

ABSTRACT	3
PREFACE.....	5
CONTENTS	7
NOMENCLATURE	9
1 INTRODUCTION	13
2 RADIAL COMPRESSOR AND VOLUTE	15
2.1 Radial compressor	15
2.2 Volute.....	17
2.3 Literature survey on the volute.....	20
2.3.1 The overall performance of the volute and its effect on the performance of the compressor	21
2.3.2 Theoretical prediction of the overall performance of the volute	36
2.3.3 The mechanical effects of the volute on the compressor.....	39
2.3.4 Detailed flow investigations in the volute	42
3 EXPERIMENTAL FACILITIES.....	49
3.1 Test compressor	49
3.2 Volute	50
3.2.1 Original volute	50
3.2.2 Circular volute	50
3.2.3 Modified circular volute	52
3.3 Measuring equipment and data acquisition.....	52
3.3.1 Compressor test stand.....	52
3.3.2 Pneumatic probe and static pressure taps	54
3.3.3 Flow visualisation.....	55
4 EXPERIMENTAL RESULTS	57
4.1 Performance map of the compressor.....	57
4.2 Efficiency of the compressor.....	61
4.3 Static pressure distribution in the diffuser, volute and exit cone	64
4.4 Results of the Cobra-probe measurements at the volute inlet.....	71
4.5 Overall performance of the volute and exit cone	77
4.6 Flow visualisation in the exit cone.....	81
4.7 Conclusions from the experimental work	85
5 NUMERICAL CALCULATION	88
5.1 General	88
5.2 Governing equations and their solution method	89
5.3 Turbulence modelling	92
5.4 Geometry and grid.....	95
5.5 Boundary conditions and numerical parameters	99
6 NUMERICAL RESULTS	100
6.1 Calculated cases and convergence	100

6.2	Overall performance of the compressor and the volute	104
6.3	Circumferential distribution of the flow variables in the diffuser and the volute .	108
6.4	Flow structure in the volute and the exit cone	116
6.5	Conclusions from the numerical analysis.....	120
7	RADIAL FORCES	122
7.1	Force measurement using magnetic bearings.....	122
7.1.1	Magnetic bearings as force measuring devices.....	122
7.1.2	Calibration of the magnetic bearings	123
7.1.3	Magnetic bearing force measurement	125
7.1.4	Results of the magnetic bearing measurements	128
7.2	Impeller force from the pressure measurements	131
7.3	Analysis of the force measurement and comparison of different methods	132
7.4	Conclusions from the radial force measurements	136
8	CONCLUSION.....	137
	REFERENCES	139
	APPENDICES	147
	APPENDIX A Calibration documents for the Cobra-probe	
	APPENDIX B Guidelines for the interpretation of the tuft movements	
	APPENDIX C Grid size in the different blocks	

NOMENCLATURE

Capital letters

A	area, m^2
C_μ	coefficient in the k - ε turbulence model, dimensionless
C_1	coefficient in the k - ε turbulence model, dimensionless
C_2	coefficient in the k - ε turbulence model, dimensionless
C_{pr}	static pressure recovery coefficient, dimensionless
E	total energy per volume, J/m^3
F	force, N
F, G, H	flux vectors in x -, y - and z -directions
I	electric current, A
K_E	exit cone loss coefficient by Weber and Koronowski, dimensionless
K_p	total pressure loss coefficient, dimensionless
K_r	radial force coefficient, dimensionless
K_T	volute loss coefficient by Weber and Koronowski, dimensionless
N	rotational speed, 1/s
N_s	specific speed, dimensionless
P	production of the kinetic energy of turbulence per volume, W/m^3
Q	source term vector
R	specific gas constant, $J/(kgK)$
R_a	surface roughness, μm
S	surface, area of the surface S , m^2
S	swirl number, dimensionless
T	temperature, K
T_u	turbulence intensity, dimensionless
U	vector of conservative variables
V	volume, m^3
\vec{V}	velocity vector
X, Y	co-ordinates of the magnetic bearings

Small letters

a	distance between the radial bearings, m
b	diffuser height, m
b	distance in general, m
c	distance of the force of the motor from the lower bearing, m
c	absolute velocity, m/s
c_p	specific heat capacity in constant pressure, $J/(kgK)$
c_v	specific heat capacity in constant volume, $J/(kgK)$
d	diameter, m
e	specific internal energy, J/kg
h	specific enthalpy, J/kg
i	imaginary unit
k	kinetic energy of turbulence, J/kg
l	length, m
\vec{n}	unit normal vector

p	pressure, Pa
q_i	heat flux in i direction, W/m ²
q_m	mass flow rate, kg/s
q_v	volume flow rate, m ³ /s
r	radius, m
s	specific entropy, J/(kgK)
t	time, s
t	clearance between the impeller and the tongue of the volute, m
u_τ	friction velocity, m/s
u, v, w	velocity components in x -, y - and z -directions, m/s
u_i	velocity component in i -direction, m/s
x, y	co-ordinates of the volute
x, y, z	Cartesian co-ordinates (in general)
y_n	normal distance from the wall, m
y^+	non-dimensional normal distance from the wall, dimensionless

Greek letters

α	absolute flow angle measured from axial/radial direction, °
γ	ratio of the specific heats $\gamma = c_p/c_v$, dimensionless
δ	Kronecker's delta function
Δ	difference
ε	dissipation of the kinetic energy of turbulence, W/kg
$\tilde{\varepsilon}$	dissipation of the kinetic energy of turbulence in Chien's model, W/kg
η	efficiency, dimensionless
θ	circumferential angle of the volute, $\theta \in [0, 360]$, °
λ	swirl parameter $\lambda = c_u/c_r$, dimensionless
μ	dynamic viscosity, kg/(ms)
μ_T	turbulent viscosity, kg/(ms)
μ_k	diffusion coefficient of k , kg/(ms)
μ_ε	diffusion coefficient of ε , kg/(ms)
ξ	friction loss coefficient, dimensionless
π	pressure ratio, dimensionless
π	ratio of the circumference and diameter of a circle $\pi \approx 3.14$, dimensionless
ρ	density, kg/m ³
σ_k	coefficient in the k - ε turbulence model, dimensionless
σ_ε	coefficient in the k - ε turbulence model, dimensionless
τ	shear stress, N/m ²
ϕ	flow coefficient, dimensionless
ϕ	angle of the radial force in x, y (volute) co-ordinates, $\phi \in [-180, 180]$, °
Φ	angle of the radial force in X, Y (magnetic bearing) co-ordinates, $\Phi \in [-180, 180]$, °
Ω	angular velocity, rad/s

Subscripts

0	zero load
1	compressor inlet
2	impeller outlet / diffuser inlet
3	diffuser outlet / volute inlet
3←3.5	fictive quantity at point 3 based on the conditions at 3.5
3←4	fictive quantity at point 3 based on the conditions at 4
3.5	in the volute at the point where 50% of the mass flow is collected
4	volute 360°
4'	exit cone at the volute tongue
5	exit cone outlet
d	upper bearing
des	design
e	exit cone
f	friction
h	hydraulic
i	impeller
i	index
i, j, k	grid co-ordinate directions
ij	ij-component of a matrix
in	inlet
k	kinetic energy of turbulence
m	electric motor
mvdl	meridional velocity dump loss
n	component normal to the surface
n	index
n	lower bearing
out	outlet
p	pull
r	radial component
ref	reference state
s	isentropic
swirl	swirl
T	turbulent, turbulence
t	total state
t-s	total-to-static
t-t	total-to-total
through	through flow
tvdl	tangential velocity dump loss
u	tangential component
w	wall
v	viscous
X, Y	(components) in the direction of the X- and Y -axes
x, y, z	(components) in the direction of the x-, y- and z-axes
ε	dissipation of the kinetic energy of turbulence

Superscripts

^	convective value
"	fluctuating component
–	averaged quantity
→	vector

Abbreviations

AC	alternating current
ASME	The American Society of Mechanical Engineers
CFD	computational fluid dynamics
CPU	central processing unit
DDADI	diagonally dominant alternating direction implicit (time integration method)
DIN	Deutsches Institut für Normung e.V.
DNS	direct numerical simulation
exp.	experiment, experimental
HUT	Helsinki University of Technology
ISA	International Federation of the National Standardizing Associations (ISA was succeeded by ISO in 1946)
ISO	International Standardization Organization
LES	large eddy simulation
LUT	Lappeenranta University of Technology
MUSCL	monotone upwind schemes for conservation laws
PC	personal computer
RANS	Reynolds-averaged Navier-Stokes
VDI	Verein Deutscher Ingenieure

1 INTRODUCTION

Centrifugal compressors are used in applications where gas has to be compressed continuously to a higher pressure, for example in process industry, oil and gas industry, refrigeration plants, compressed air networks, turbochargers and aeration plants. High compressor efficiency is naturally required in order to save energy and to keep the operating costs low, but often a wide operating range and good efficiency also at off design conditions is of utmost importance. Thus a suitable balance between high peak efficiency and adequate off-design performance has to be established. On the other hand, in several applications cheap manufacturing costs and compact size are required. Then a suitable compromise between performance and costs has to be found.

This study focuses on one component of a radial compressor, the volute. In a radial compressor the flow behind the diffuser has still a reasonably high velocity (usually 100 - 150 m/s). This flow has to be collected and led to the pipe system with minimum losses and preferably so that a part of the remaining kinetic energy can be recovered. This is usually done by a spiral shaped volute also known as a scroll.

It could be argued that the volute is only the third important component of the compressor after the impeller and the diffuser. Probably due to this reason not so much research had been focused on the volute earlier. In the 1990s, however, the volute has been the subject of numerous research projects. The reason for this is simple. The volute strongly affects the overall performance of the compressor. Stability, operating range and the location of the best efficiency point are influenced by the volute design. The radial force on the impeller is a result of the pressure non-uniformity caused by the volute. In addition, the volute is the bulkiest component of the compressor and thus manufacturers are seeking for more compact designs for the volute.

On the other hand, centrifugal pump volutes were studied fairly frequently during the 20th century. The performance of the pump is more strongly affected by the volute than the performance of the compressor, since pumps do not generally have a diffuser between the impeller and the volute. Naturally there exists a strong analogy between the pump and compressor volutes, as both are radial flow machines. This study, however, is limited to single-stage centrifugal compressors only. Pump volutes are not investigated in detail, but

some important pump studies are presented, because the results and research methods are analogous and can to some extent be applied for the compressor volutes as well.

In this study a single-stage centrifugal compressor with three different volutes is investigated. The test compressor was first equipped with the original volute, the cross-section of which was a combination of a rectangle and semi-circle. Next a new volute with a fully circular cross-section was designed and manufactured. Finally, the circular volute was modified by rounding the tongue and smoothing the tongue area. The experimental survey of the volute has been carried out using static pressure measurements, two-dimensional three-hole probe measurements, flow visualisations and magnetic bearing force measurements. Three-dimensional flow measurements have not been done due to the available resources.

As a part of the study the complete compressor with the circular volute (inlet pipe, full impeller, diffuser, volute and outlet pipe) has also been simulated using computational fluid dynamics. A fully 3-D viscous flow has been solved using a Navier-Stokes solver, Finflo, developed at Helsinki University of Technology.

The aim of this study is to:

1. Gain further understanding on the volute flow.
2. Gain further understanding on the effect of the volute asymmetry on the performance of the compressor and the radial forces.
3. Compare the different volute geometries.
4. Improve the compressor performance especially at high mass flow.

Several studies concerning the volute have been investigated, see chapter 2.3. The present work supplements the earlier research in the following ways: In this work a standard industrial compressor is investigated at its design speed and pressure ratio. Special attention is paid to the effects of the tongue shape, tongue gap and the interaction between the volute and the exit cone. The radial forces caused by the volute are measured using magnetic bearings and investigated together with the volute flow. In addition, the numerical analysis is comprehensive because the flow in the complete compressor has been calculated as viscous and turbulent.

2 RADIAL COMPRESSOR AND VOLUTE

2.1 Radial compressor

The main components of a radial compressor and the notations used in this work are shown in figure 1. First, the flow enters the impeller, which transfers energy to the gas. After the impeller the flow has high velocity and thus high kinetic energy. The flow is then decelerated in the diffuser, which increases the static pressure but causes some unavoidable total pressure loss. After the diffuser the flow has still a reasonably high speed, about 100 - 150 m/s. This high speed flow has to be collected around the circumference of the diffuser and led to the pipe system with minimal losses, and preferably so that a part of the remaining kinetic energy can be recovered. Most often this is accomplished with a volute, which is shown in grey in figure 1.

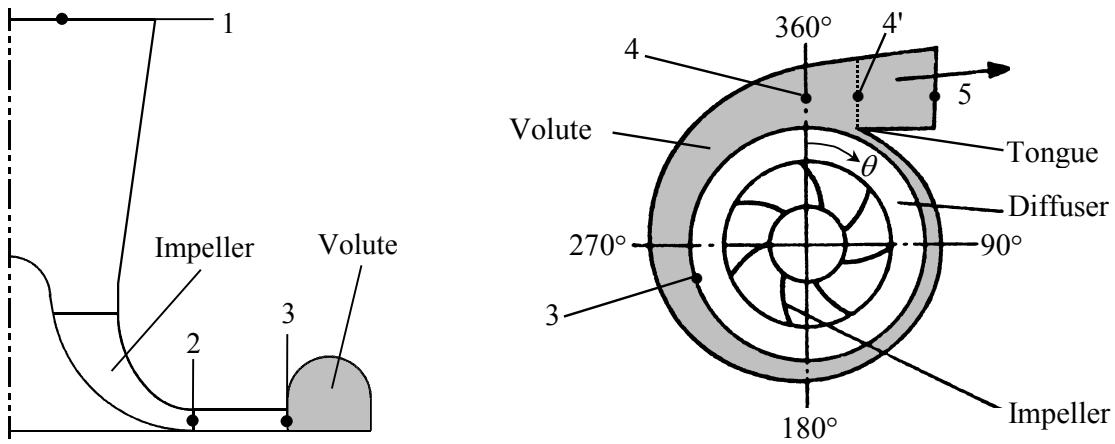


Figure 1. The main components of a radial compressor and the notations used in this work.

The compression is assumed to be adiabatic in the calculations as well as in the analyses of experimental data. The isentropic efficiency of the compressor is defined by comparing the actual compression to the ideal i.e. isentropic compression. Two different assumptions can be made while doing this. The compression can be examined either from the total inlet state to the total outlet state or from the total inlet state to the static outlet state. The first approach assumes that the kinetic energy after the compressor is accounted as useful energy, whereas the second approach assumes that the kinetic energy after the compressor is lost. The total-to-total isentropic efficiency η_{s-t-t} is defined with equation (1),

$$\eta_{s-t-t} = \frac{h_{t5s} - h_{t1}}{h_{t5} - h_{t1}} \approx \frac{T_{t5s} - T_{t1}}{T_{t5} - T_{t1}} \quad (1)$$

and the total-to-static isentropic efficiency $\eta_{s\ t-s}$ with equation (2)

$$\eta_{s\ t-s} = \frac{h_{5s} - h_{t1}}{h_{t5} - h_{t1}} \approx \frac{T_{5s} - T_{t1}}{T_{t5} - T_{t1}} \quad (2)$$

where h is the specific enthalpy and T the temperature with subscript t referring to the total state and subscript s referring to the isentropic compression. In experimental analysis the specific heat and enthalpy of the moist air is calculated from a third degree polynomial fit (Backman 1996), and thus the calculation of the efficiency is done in the exact way using the enthalpies. In numerical analysis a constant specific heat c_p is given, and thus the efficiency is calculated using the temperatures in equations (1) and (2). This simplification is negligible in comparison to other inaccuracies in the numerical calculation.

The outlet temperature of the isentropic compression needed in equations (1) and (2) is calculated from the measured or numerically predicted pressure ratio as follows:

$$\frac{T_{t5s}}{T_{t1}} = \left(\frac{p_{t5}}{p_{t1}} \right)^{\frac{R}{c_p}} \quad (3)$$

$$\frac{T_{5s}}{T_{t1}} = \left(\frac{p_5}{p_{t1}} \right)^{\frac{R}{c_p}} \quad (4)$$

where p is the pressure and R the specific gas constant. In equations (3) and (4) an average specific heat $\overline{c_p}$ between the inlet and outlet state is used. Equations (1) - (4) can be used between any states of the compressor, for example to determine the efficiency of the impeller (1→2) or the impeller diffuser combination (1→3).

The performance of the compressor depends on the inlet state. Reference values must be used in order to compare the measurements done at different ambient conditions with each other and with the numerical data. The reference mass flow $q_{m\ ref}$ and reference speed N_{ref} are calculated according to equations (5) and (6).

$$q_{m\ ref} = q_m \frac{p_{t1\ ref}}{p_{t1}} \sqrt{\frac{T_{t1} R}{T_{t1\ ref} R_{ref}}} \quad (5)$$

$$N_{ref} = N \sqrt{\frac{T_{t1\ ref} R_{ref}}{T_{t1} R}} \quad (6)$$

where q_m is the mass flow and N is the rotational speed in the actual conditions, and the quantities with the subscript *ref* the values in the chosen reference conditions. In industrial applications volume flow is often used instead of mass flow. This is well suited for vacuum compressor applications, since the radial compressor is a volume flow machine by nature. The volume flow q_v is scaled to the reference conditions according to equation (7).

$$q_{v\ ref} = \frac{q_{m\ ref}}{\rho_{1\ ref}} = q_{m\ ref} \frac{T_{t1\ ref} R_{ref}}{P_{t1\ ref}} = q_v \sqrt{\frac{T_{t1\ ref} R_{ref}}{T_{t1} R}} \quad (7)$$

where ρ is the density.

2.2 Volute

The grey part in figure 1 contains two distinct parts. Between states 3 and 4 is the volute, which collects the flow around the diffuser, and between states 4 and 5 is the exit cone, which further decelerates the flow before it enters the pipe system. The beginning of the exit cone between states 4 and 4' is partially connected to the diffuser and to the small volute channel through the tongue gap. The term volute is used in the literature to mean either only the part between states 3 and 4 or the whole grey part between states 3 and 5. In this work the term volute means only the part between states 3 and 4. The volute and the exit cone have to be examined closely together, however, since the performance of the exit cone greatly depends on the flow field produced by the volute and especially on the flow disturbances originating from the tongue area. In addition, the whole grey part is most often cast as a single piece, so it can be considered as a single component from the manufacturer's point of view.

The volute is often designed according to one-dimensional calculation, in which the flow in the volute is assumed to be frictionless and incompressible. The radial and tangential velocity components after the diffuser, c_{r3} and c_{u3} , are calculated first. The through flow velocity in the volute cross-section is then calculated assuming constant angular momentum. The area of the cross-section in each circumferential position is calculated using the continuity equation so that the through flow velocity stays constant as more flow enters the volute at velocity c_{r3} . In this way the static pressure in the volute is constant around the circumference. (Larjola 1988, Eck 1957)

When the compressor operates outside its design point, the through flow velocity in the volute cannot stay constant any longer. At small mass flow less fluid enters the volute than at the design point. This leads to a decrease of the through flow velocity and to an increase of the static pressure, since the area of the cross-section grows more rapidly than needed. Accordingly, at high mass flow the through flow velocity speeds up and the static pressure falls down along the circumference. This velocity and pressure non-uniformity may be present even at the design flow, if the volute has been poorly designed. When a vaneless diffuser is used, the non-uniform pressure distribution acts back on the diffuser and the impeller, and can be noticed even at the leading edge of the impeller blades (Sorokes et al. 1998). This causes pressure, velocity and flow angle oscillations in the diffuser and in the impeller blade passages, which leads to a decrease in efficiency and additional noise. The stable operating range of the compressor is also decreased (Ayder 1993). The pressure non-uniformity also causes radial force on the impeller and unsteady forces on the blades, which can lead to excessive loadings on the bearings and to blade vibrations. Diffuser vanes considerably attenuate the effect of the volute pressure distortion on the impeller (Cui 2000).

According to Stiefel (1972) the matching of the impeller, vaneless diffuser and volute becomes a challenging task, since the pressure ratio of a single-stage radial compressor can vary greatly depending on the operating point. Thus one has to consider the whole design domain of the compressor instead of a single point. In an overpressure compressor a constant static pressure distribution in the volute is achieved at different flows at different pressure ratios, but at any pressure ratio there is only one flow rate, which produces constant pressure distribution.

The overall performance of the volute can be analysed using the total pressure loss and static pressure recovery coefficients. The total pressure loss coefficient is defined as follows:

$$K_p = \frac{P_{t\ in} - P_{t\ out}}{P_{t\ in} - P_{in}} \quad (8)$$

and the static pressure recovery coefficient as follows:

$$C_{pr} = \frac{P_{out} - P_{in}}{P_{t\ in} - P_{in}} \quad (9)$$

where $p_{t\ in}$ is the total pressure and p_{in} is the static pressure at the inlet of the component under investigation, and $p_{t\ out}$ and p_{out} are the total and static pressures at the outlet. The coefficients

K_p and C_{pr} can be calculated for example for the volute alone (3→4) or for the volute and exit cone combination (3→5). Their value varies depending on the operating point of the volute, and thus the coefficients are sometimes presented as a function of mass flow (Fahua et al. 2000), volute inlet flow angle α_3 (Hagelstein et al. 2000) or volute inlet swirl parameter λ_3 (Japikse 1996), which is defined as a ratio of the tangential and radial velocity at the volute inlet, equation (10).

$$\lambda_3 = \frac{c_{u3}}{c_{r3}} \quad (10)$$

The swirl parameter λ_3 that Japikse uses describes the intensity of the swirl in relation to the rotational axis of the compressor. However, the radial velocity that enters the volute forces the flow to the swirl inside the volute channel. Therefore, from the volute point of view, the inverse of the swirl parameter better describes the swirl that develops into the volute channel. Thus for example Ayder (1993) presents the overall performance of the volute as a function of $1/\lambda$.

Typically, the total pressure loss of the volute increases together with the mass flow, since the flow angle at the volute inlet becomes more radial, resulting in stronger swirl inside the volute, and the velocities increase, resulting in higher friction losses. Simultaneously the static pressure recovery of the volute decreases rapidly due to the flow acceleration and increased losses. Figure 2 shows the overall performance of the volute measured by Ayder (1993) and Hagelstein et al. (2000). The results of Ayder (1993) have been obtained between states 3 and 4', so they describe the performance of the volute alone. The results of Hagelstein et al. (2000) contain the performance of both the volute and exit cone (states 3→5), which explains the clearly higher static pressure recovery.

When the mass flow decreases well below the design flow, some authors, such as Ayder (1993), report still decreasing total pressure loss. However, depending on the volute and exit cone design, the loss might also increase at low flow, like Hagelstein et al. (2000) and Fahua et al. (2000) report. This is typically a result of flow separation either in the volute itself or in the exit cone.

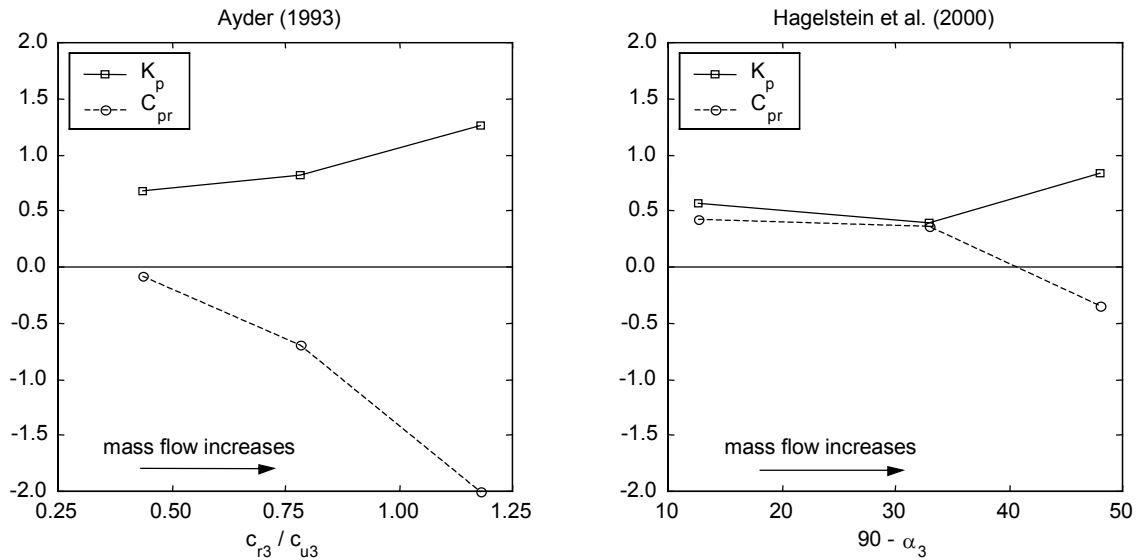


Figure 2. Typical overall performance of the volute at different operating points. The measurements of Ayder (1993) on the left and Hagelstein et al. (2000) on the right.

2.3 Literature survey on the volute

In the field of radial compressor research fairly little work had focused on the volute in comparison to the other components prior to mid 1980's. The lack of information on the volute flow was recognised, which resulted in a considerable increase in publications on the volute in the late 1980's and the 1990's. The literature survey on the volute is divided into four main categories in this work:

1. The overall performance of the volute and its effect on the performance of the compressor
2. Theoretical prediction of the overall performance of the volute
3. The mechanical effects of the volute to the compressor (radial forces, vibrations etc.)
4. Detailed flow field investigations in the volute

The above categorisation has been adapted from Ayder (1993). Publications concerning centrifugal pumps are included in this work to a lesser degree, and are reviewed only in cases where they bring substantial additional information.

2.3.1 The overall performance of the volute and its effect on the performance of the compressor

According to Ayder (1993) the overall performance of the volute is affected mainly by the following five geometric parameters:

1. Area of the cross-section
2. Shape of the cross-section
3. Radial location of the cross-section
4. Location of the volute inlet
5. Tongue geometry

2.3.1.1 Area of the cross-section

Correct circumferential increase in the area of the cross-section provides uniform through flow velocity in the volute and uniform distribution of the flow variables at the diffuser exit, when the volute operates at the design pressure and at the design flow. At any other flow rate, or when the volute is poorly designed, a non-uniformity of the flow variables exists, which has numerous effects on the compressor.

Bowerman and Acosta (1957) have investigated a centrifugal pump with three different double volutes, one designed for 75%, one for 100% and the third for 120% of the nominal flow of the impeller. The volutes were two-dimensional (i.e. the volute height was the same as that of the impeller flow passage) so the circumferential increase in the cross-sectional area was controlled solely by the form and location of the volute outer wall. Figure 3 shows the overall performance of the pump with the different volutes. It is clearly seen how the point of maximum efficiency can be shifted towards lower flow by decreasing the volute area and towards higher flow by increasing it.

Bowerman and Acosta (1957) have also measured the performance of the impeller. The curves resemble very much those in figure 3. On the basis of the impeller and torque measurements the authors comment that: "The significant result is that the performance is controlled by the influence of the volute shape on the impeller operation rather than by the addition of losses to the fluid within the volute." The loss inside the volute itself is found to be relatively small.

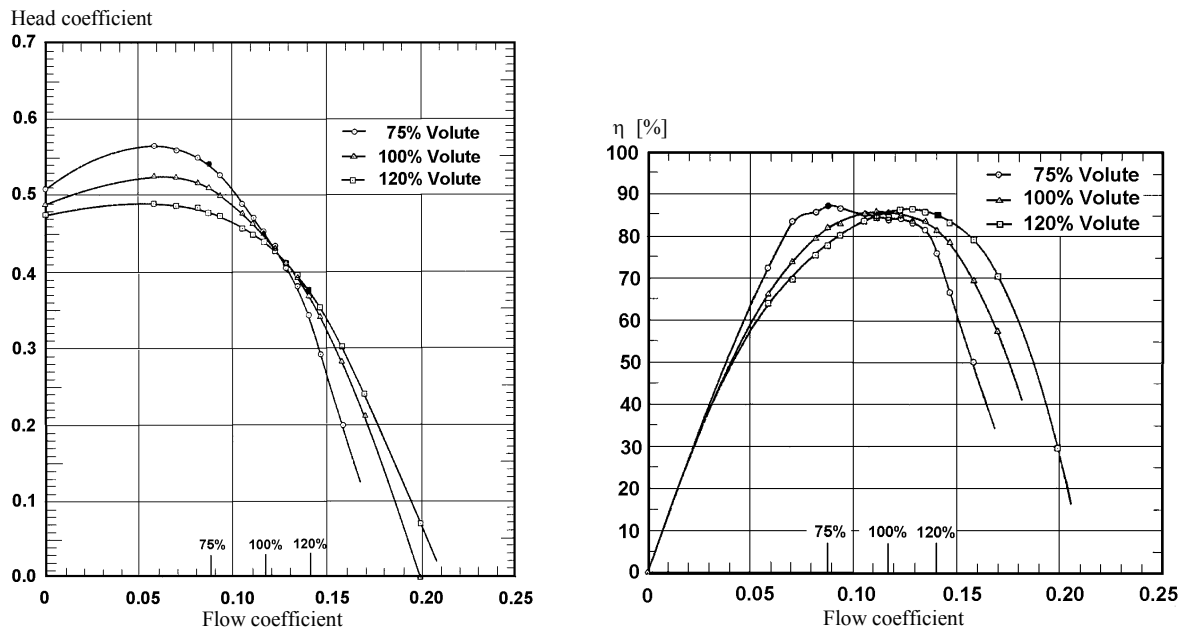


Figure 3. The effect of the volute cross-sectional area on the pump overall head and efficiency. (Bowerman and Acosta 1957)

Stiefel (1972) has investigated a large number of different impeller - diffuser - volute configurations. He shows that the area of the cross-section of the volute has a major influence on the shape of the performance map and on the stable operating range of the compressor. A larger volute, designed for a compressor pressure ratio $p_{t5}/p_{t1} = 3.8$ according to the frictionless flow, gives the highest compressor efficiency around the pressure ratio of 2, see the left side of figure 4. It also gives reasonably wide operating range at pressure ratios up to 3.5, but causes unstable operation, if the pressure ratio exceeds 4. The stable operating range is extended up to the pressure ratio of 7.2, when the same compressor is equipped with a smaller volute, which is designed for a pressure ratio of 6.0, see the right side of figure 4. The smaller volute also shifts the maximum efficiency of the compressor to the pressure ratio of 3.5 and considerably increases the efficiencies at higher pressure ratios. Simultaneously the use of the smaller volute shifts the whole operating map towards lower flow and narrows the range of operation.

Stiefel (1972) also claims that generally the best compressor efficiency is achieved, when the volute cross-sectional area is 10 - 15% smaller than the area calculated according to the frictionless flow.

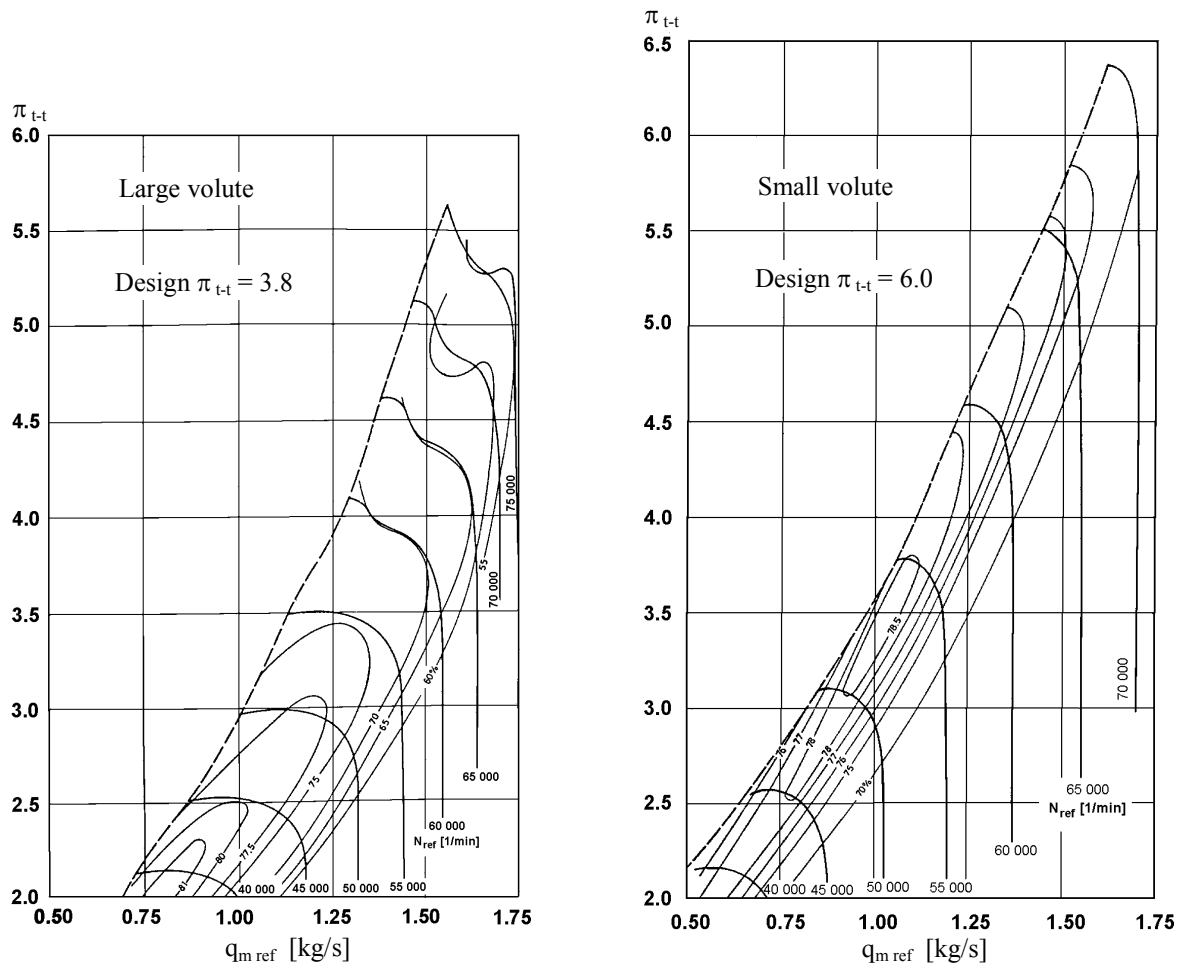


Figure 4. The effect of the volute cross-sectional area on the compressor performance map. (Stiefel 1972)

Whitfield and Roberts (1983) present a study in which two alternative volutes to a standard turbocharger compressor were manufactured and measured. Because the vaneless diffuser could not be further improved, a proposal was made to improve the overall diffusion by transferring a part of it from the diffuser to the exit cone of the volute or to the volute itself. The first new volute, P1, was designed so that it did not allow any diffusion in the volute, but the diffusion took place in the exit cone. To enable this the cross-sectional area of the volute P1 was smaller than the area of the standard volute. The radius ratio of the vaneless diffuser was reduced from 1.625 to 1.4 for the volute P1. The second new volute, P2, had a larger cross-sectional area than the standard volute to allow diffusion inside the volute, and the radius ratio of the diffuser increased along the circumference from 1.4 to 1.625 for the volute P2.

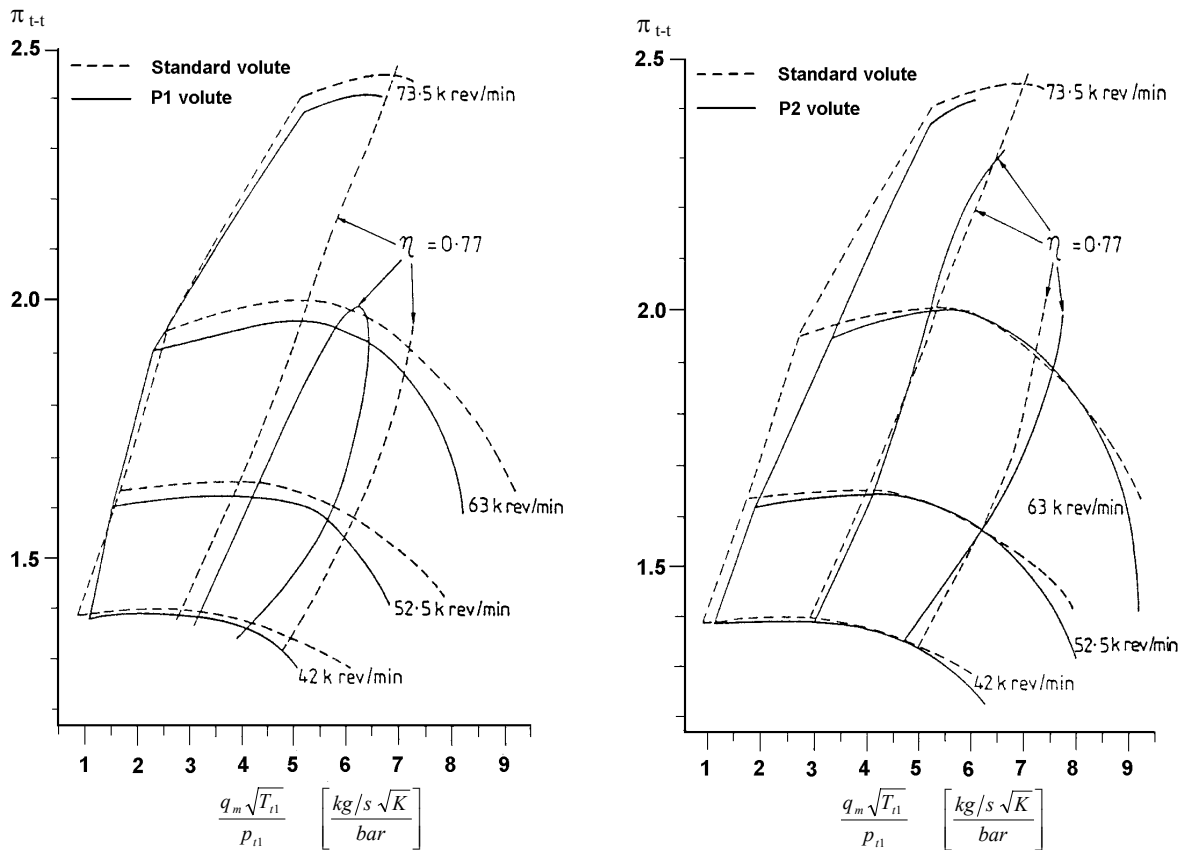


Figure 5. Performance maps of the compressor with volute P1 (left) and volute P2 (right) and comparison to the standard configuration. (Whitfield and Roberts 1983)

Figure 5 shows the performance maps of the compressor with the new volutes and comparison to the standard configuration. It is seen that both of the new configurations have a negative effect on the performance. The compressor with the volute P1 is reported to produce a lower pressure ratio mainly due to the increased losses in the volute, because it has to collect the flow around the diffuser at high velocity. The compressor with the volute P2 delivers an almost equal pressure ratio, but the stall limit is shifted towards higher flow. This is mainly due to the greatly increased non-uniformity of the pressure distribution at off-design conditions. The notable decrease in the performance with both new volutes at high flow can be attributed to the increased pressure non-uniformity. Whitfield and Roberts (1983) give also the difference in the tongue geometry as a possible reason for the poor performance of the new volutes.

Mishina and Gyobu (1978) have carried out an experimental survey on the performance of a single-stage centrifugal compressor. Their experiments included seven different volutes shown in figure 6. The parameters investigated were the circumferential area distribution, the cross-sectional shape and the radial position of the cross-section. The circumferential static

pressure distribution at the design flow is presented for the volutes s-1, s-6 and s-7 in figure 7 on the left. It is seen how the static pressure increases along the circumference with the volute s-1 indicating that the cross-sectional area grows more rapidly than needed for the uniform flow. The area distribution of the volute s-6 leads to more uniform through flow velocity at the design flow rate, although some diffusion is observed in the volute s-6 as well. Oddly enough, a rather constant static pressure distribution is reported with the constant area collector s-7.

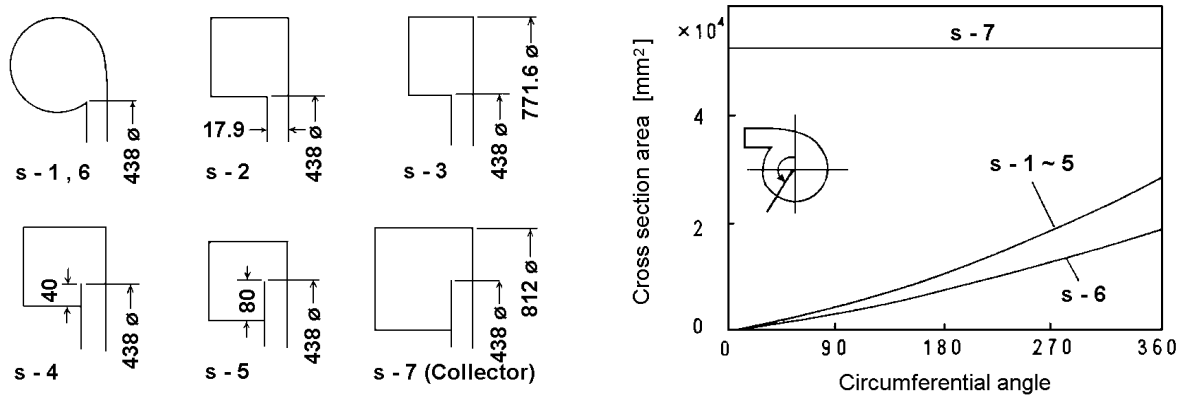


Figure 6. Different volutes tested by Mishina and Gyobu (1978).

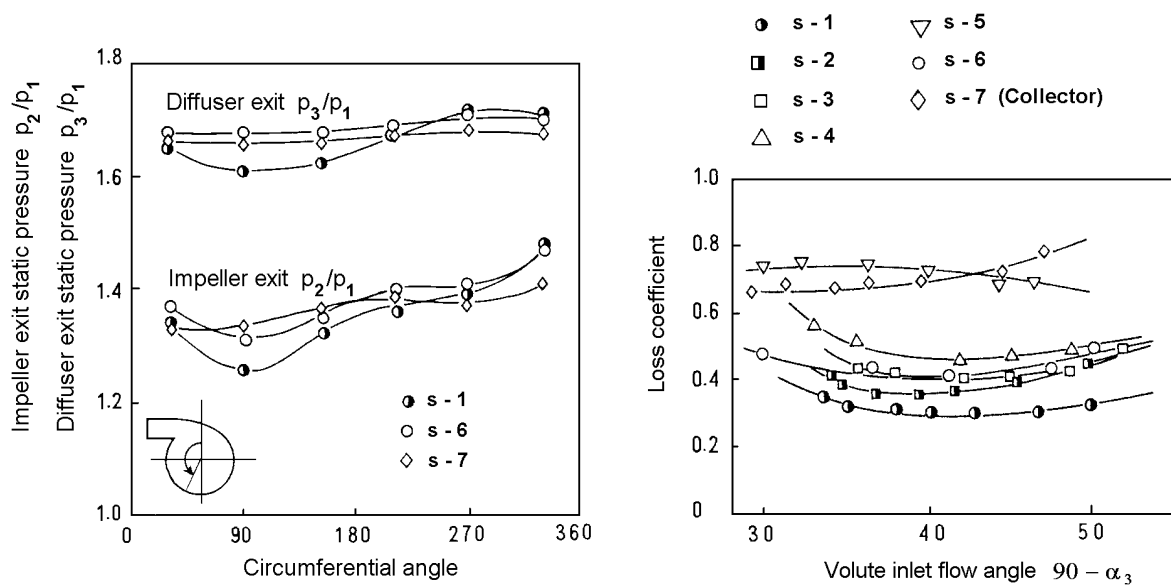


Figure 7. Circumferential static pressure distribution (left) and loss coefficient (right) of the different volutes tested by Mishina and Gyobu (1978).

The measured loss coefficients of the different volutes are shown in figure 7 on the right. The circular volute s-1 has clearly smaller losses than the circular volute s-6 due to the bigger increase in the cross-sectional area in the volute s-1. This is an interesting observation

showing how the over-dimensioned increase in the cross-sectional area leads to low losses inside the volute. Unfortunately no information is presented about the overall performance of the compressor, so no conclusion can be made about the possible negative effects of the static pressure distortion caused by the volute over-sizing.

Brown and Bradshaw (1947) examined a mixed flow compressor, and report a notable increase in the efficiency (3-12 percentage points), a substantial increase in the pressure coefficient and extension of the operating range towards high flow, when a constant area collector was replaced by a volute with a circumferentially increasing cross-sectional area.

Hagelstein et al. (1997) have analysed the effect of circumferential static pressure non-uniformity on the compressor flow. They show how a collecting chamber with a constant area of cross-section produces a substantial pressure distortion even at nominal flow. This pressure distortion propagates backwards through the vaneless diffuser and is clearly seen near the impeller exit. It can be attenuated by diffuser vanes or a throttling ring at the end of the vaneless diffuser. When a volute with an increasing cross-section is used, the pressure distribution is uniform at the design flow. At off-design conditions the volute produces a pressure distortion of the same order of magnitude as the collecting chamber. Asymmetrically adjusted diffuser vanes are shown to have a favourable effect on the non-uniform pressure field.

Sorokes et al. (1998) have made experiments and numerical simulations on a six-stage centrifugal gas re-injection compressor operating at over 400 bar pressure. They show that the pressure non-uniformity originating from the volute of the third stage of the compressor is fairly analogous to the one observed in a single-stage machine by Hagelstein et al. (1997). Non-uniformity is observed at the impeller inlet as well.

Qi et al. (1996) have presented a two-dimensional inverse method for the design of the volutes of centrifugal fans. According to their findings, the conventional design resulted in a non-uniform distribution of the flow parameters (e.g. p_3 , c_3 , α_3 etc.) at the volute inlet due to non-axisymmetrical volute geometry and the influence of the tongue. With the method developed by them the area distribution of the volute could be redesigned. Figure 8 shows how in their case the area of the cross-section had to be increased in the beginning of the volute. The new inverse method allowed a uniform flow angle α_3 distribution at the volute inlet to be achieved

at the design point. The redesign of the volute resulted in a slight increase in the efficiency and in a considerable reduction in the noise throughout the whole operating range.

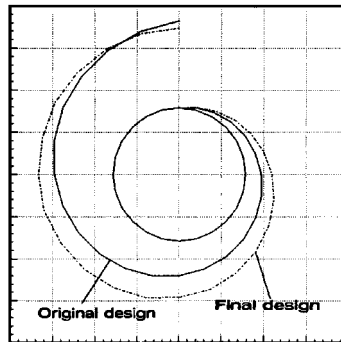


Figure 8. The redesign of the volute according to Qi et al. (1996)

Hillewaert and Van den Braembussche (1999) have developed a numerical code to study impeller - volute interaction in a centrifugal compressor. The method couples a three-dimensional unsteady flow calculation in the impeller with a three-dimensional time-averaged flow calculation in the volute through an iterative updating of the boundary conditions on the interface of both calculation domains. An inviscid flow solver with correction terms to take account for the effects of friction has been used, and only one blade passage of the impeller has been modelled in order to save computing time and memory.

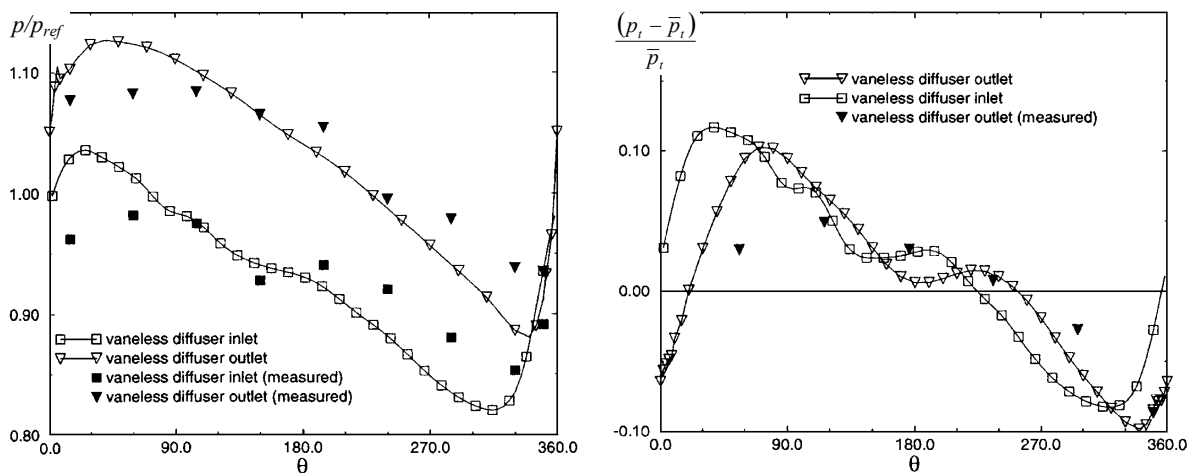


Figure 9. Circumferential variation of the static pressure (left) and total pressure (right) in the vaneless diffuser at high flow. (Hillewaert and Braembussche 1999)

The simulation made by Hillewaert and Van den Braembussche (1999) at high mass flow shows a static pressure variation with one wave along the circumference and no phase shift in this wave between the vaneless diffuser inlet and outlet, see the left side of figure 9. The calculation indicates that the strongest static pressure distortion is located around the tongue

region, which creates a separated flow into the exit cone onto the suction side of the tongue. The circumferential variation of the total pressure shows a phase shift between the diffuser inlet and outlet. Also additional weaker waves with two and four periods per rotation are observed, see the right side of figure 9. Fatsis et al. (1997) explain the two-wave pattern to be a result of pressure waves that travel back and forth in the impeller blade passages and reflect from the leading edges of the full blades. The weaker four-wave pattern is reported to be a result of the same phenomenon with the splitter blades.

2.3.1.2 Shape of the cross-section

Brown and Bradshaw (1947) have made experiments with different volutes and diffusers on a mixed flow compressor. They designed four double volutes with different cross-sectional shapes, figure 10, and manufactured them by sand casting. The aim, a constant circumferential pressure distribution at the design point, was achieved. In addition, a fifth volute similar to the volute (b) in figure 10 was manufactured by plaster casting in order to investigate the effect of the surface roughness. The volutes were tested with a mixed flow impeller and a vaneless diffuser, and the overall performance of the compressor was reported. Brown and Bradshaw (1947) conclude that both the cross-sectional shape and the surface quality have a negligible effect on the performance of the compressor.

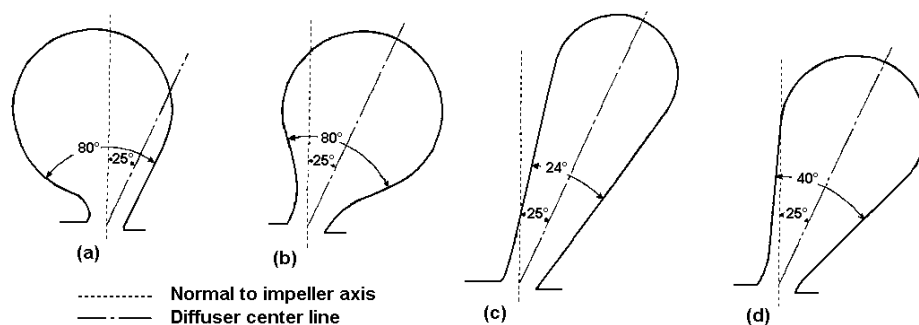


Figure 10. Different volute cross-sections tested by Brown and Bradshaw (1947).

Mishina and Gyobu (1978) have investigated the effect of shape of the volute cross-section on the total pressure loss of the volute. Although they comment that the effect of the cross-sectional shape is relatively small, one can still see a clear trend in the results, see figures 6 and 7. The volute s-1 with a circular cross-section has the lowest loss. The volute s-2 with a square cross-section has somewhat increased loss and the volute s-3 with a rectangular cross-section the highest loss among the external volutes.

Ayder (1993) reports that the shape of the volute cross-section should be symmetric. If the height and width of the volute channel are unequal, then the swirl velocity inside the volute has to accelerate and decelerate in turns, which causes additional losses. Ayder also concludes that a volute with an elliptic cross-section is more efficient than a volute with a rectangular one.

2.3.1.3 Radial location of the cross-section

The radial location of the cross-section has a strong influence on the performance of the volute. According to the conservation of the angular momentum, the tangential velocity in a swirling flow is inversely proportional to the radius. If the volute channel is located above the diffuser at a smaller radius than the diffuser outlet, then the tangential velocity inside the volute channel is higher than at the diffuser outlet. In other words, the flow which is first decelerated in the diffuser, is accelerated again in the volute. This causes additional losses and undesired static pressure drop.

Mishina and Gyobu (1978) measured three volutes: s-2, s-4 and s-5 with identical cross-sectional shape and area distribution but different radial location, see figure 6. The results presented in figure 7 show clearly that the radial location of the volute channel has a strong effect on the volute loss. The volute s-4 has high and the volute s-5 very high loss, because these volute channels are located at small radii.

Stiefel (1972) reports measurements carried out using two different volutes with almost circular cross-sections, see the left side of figure 11. Although the difference in the radial position of the volute channel was fairly small, the effect on the performance of the compressor was big. The optimum efficiency of the compressor was about 4 percentage points lower with the volute I, which had the channel at a smaller radius than the volute II, see the right side of figure 11.

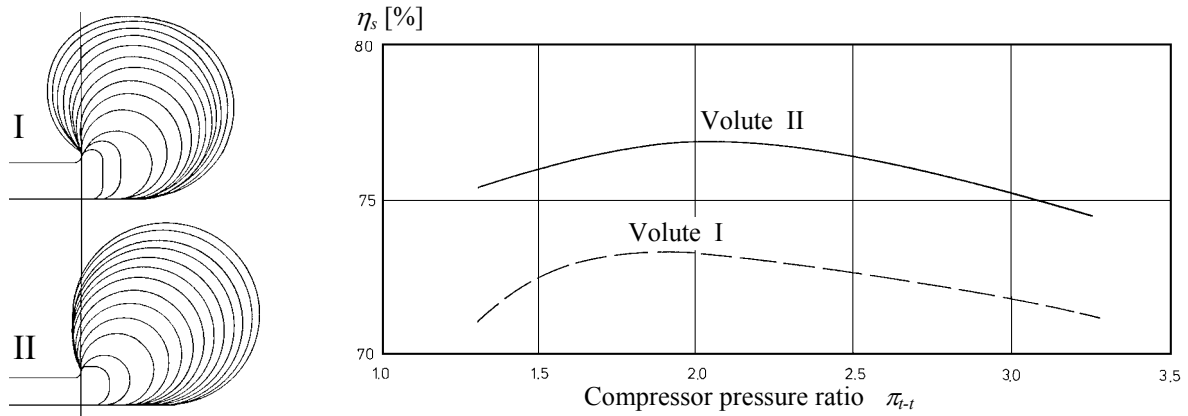


Figure 11. Left: different volutes tested by Stiefel. Right: optimum efficiency of the compressor as a function of the pressure ratio with the different volutes. The performance with the volute I is lower, because it is located at a smaller radius. (Stiefel 1972)

Ayder (1993) gives the following reasons for the poor performance of the internal volutes:

- The reduction of the radius of the volute cross-section causes a re-acceleration of the fluid and partially destroys the static pressure rise achieved in the diffuser.
- The accumulation of the low energy fluid on the volute inner wall and the decreasing curvature radius of the inner wall favour flow separation in the volute.
- Apart from the operation at high flow, a part of the low energy fluid on the inner wall recirculates in the volute through the tongue gap, which augments the above mentioned tendency for separation.

2.3.1.4 Location of the volute inlet

Lendorff and Meienberg (1944) report results from numerous product development tests carried out in multi-stage centrifugal compressors. The volute of the final stage was one of the investigated items. Figure 12 shows three different volute shapes and the performance of the final stage with those volutes. It is seen how the volute with tangential inlet (overhung volute) gives favourable performance in comparison to the symmetric volutes. However, the area of the cross-section varies as well, so it is not certain whether the improvement is caused by the location of the volute inlet alone.

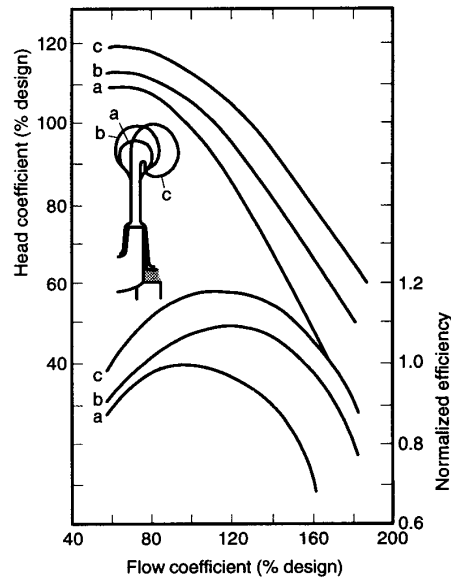


Figure 12. Different volute cross-sections tested by Lendorff and Meienberg (1944). The volute with the tangential inlet (c) gives the best performance.

Hübl (1975) has investigated a single-stage radial compressor. The tests with two different circular volutes, see figure 13, show clearly that the tangential inlet works better than the symmetric one.

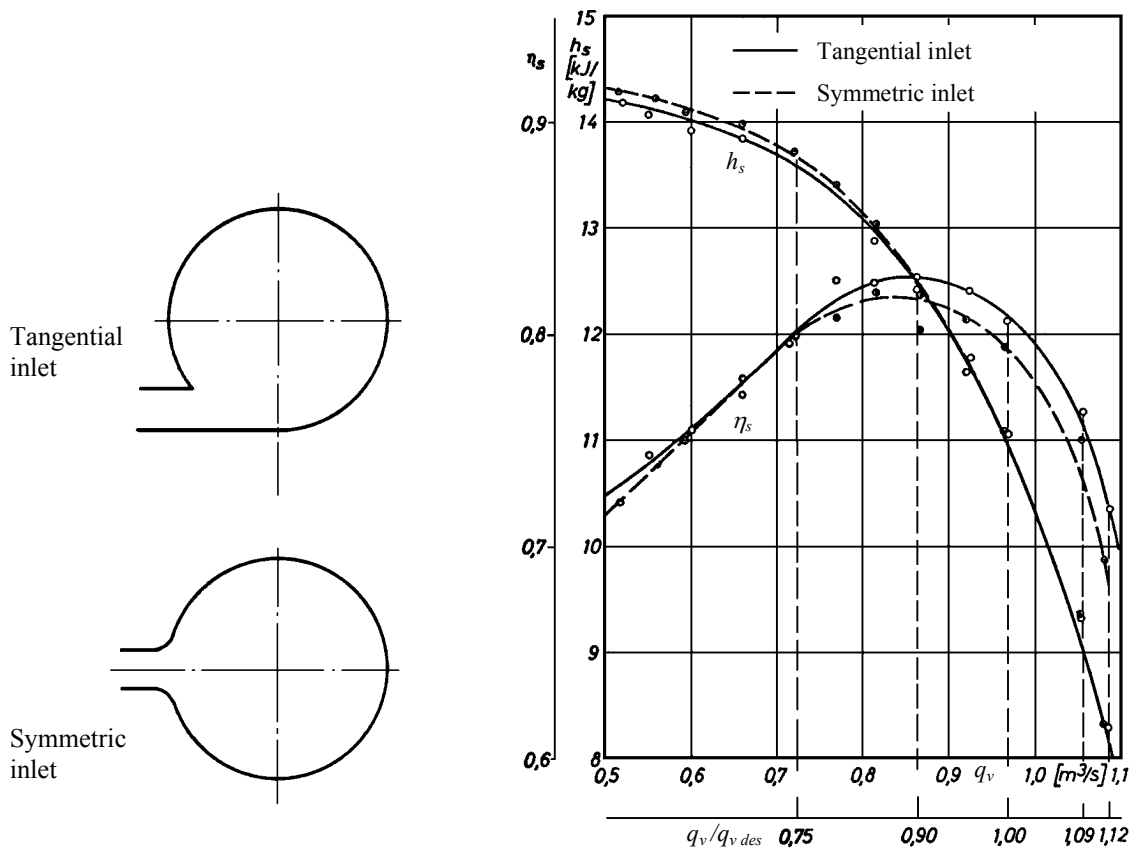


Figure 13. The volutes with tangential and symmetric inlet tested by Hübl (left) and the overall performance of the compressor with the different volutes (right). The tangential inlet gives higher efficiency. (Hübl 1975)

2.3.1.5 Tongue geometry

The flow around the tongue region has been widely investigated in radial flow pumps. Pumps usually do not have a diffuser between the impeller and volute, so the impeller-volute interaction and the effect of the tongue on the performance is far stronger than in compressors.

Lipski (1979) has made experiments on a single-stage centrifugal pump equipped with a movable and easily changeable tongue of the volute, see the left side of figure 14. According to Lipski the pump head and efficiency strongly depend on the position and shape of the tongue, see the right side of figure 14. Also the force acting on the tongue depends on the operating point of the pump and the tongue angle. The force on the tongue becomes zero close to the point of maximum efficiency.

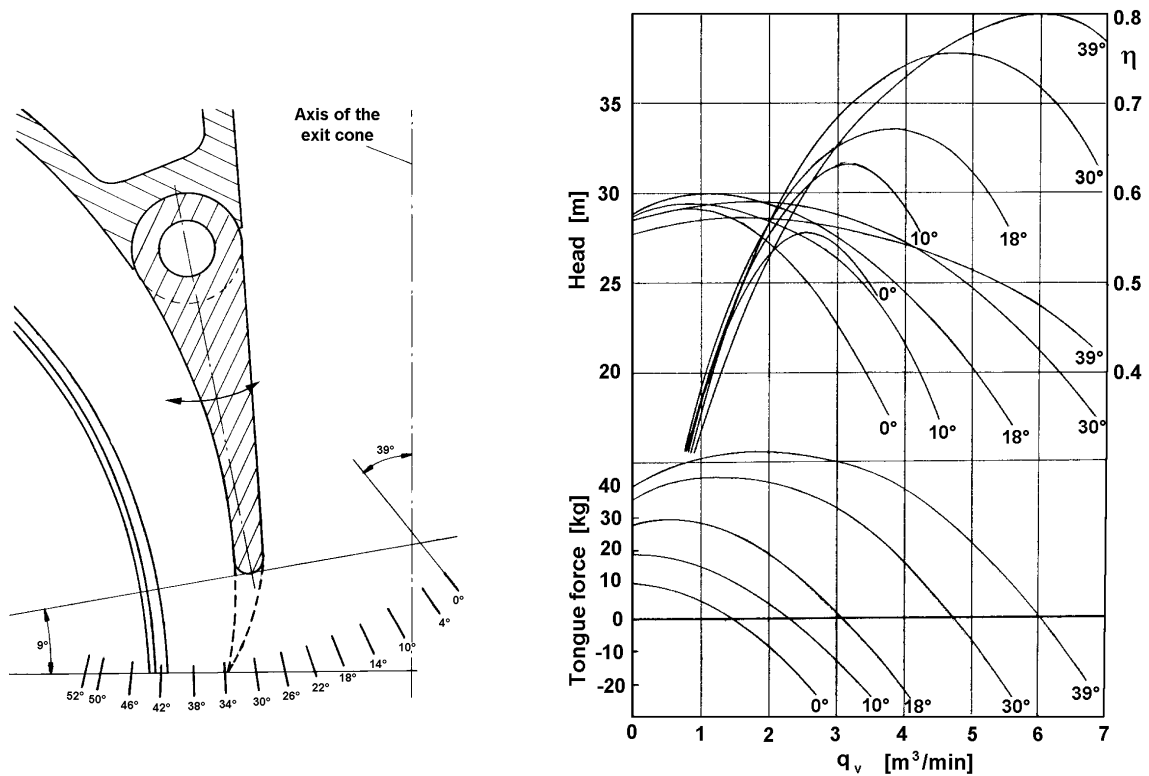


Figure 14. Left: the movable and changeable tongue of the volute of the pump tested by Lipski. Right: the effect of the tongue angle on the pump head, efficiency and force on the tongue. (Lipski 1979)

Lipski proposes that the pump could be controlled by adjusting the tongue angle or tongue length. Lipski also recommends the following possibilities for the improvement of efficiency in pumps:

- The tongue location and angle should also be changed to the optimum if the operating characteristics of the pump are adjusted by turning the impeller in a lathe.

- The tongue should be shortened if efficient operation in off-design conditions is desired. The improvement in efficiency is gained especially at high flow. In Lipski's experiments the efficiency at the design point was also increased slightly by shortening of the tongue, which indicates that the volute or the tongue were slightly mismatched with the impeller.
- The angle of the tongue could automatically be adjusted as the operation point changes.

Dong et al. (1997) have experimentally investigated the effect of the tongue shape on the performance, pressure fluctuations and noise in a centrifugal pump. The five different tongue geometries studied are shown in figure 15 on the left and their effect on the overall characteristics of the pump on the right. It is seen how the head of the pump can be increased both at low and high flows by retracting and rounding the tongue. Only the very much shortened tongue number 5 with a 27% gap between the impeller and tongue decreases the performance at high flow. Dong et al. (1997) also report a reduction in noise when the tongue was moved away from the impeller. The attenuation was notable when the tongue gap was increased from 7% to 11% or 18%, but insignificant when the gap was further increased.

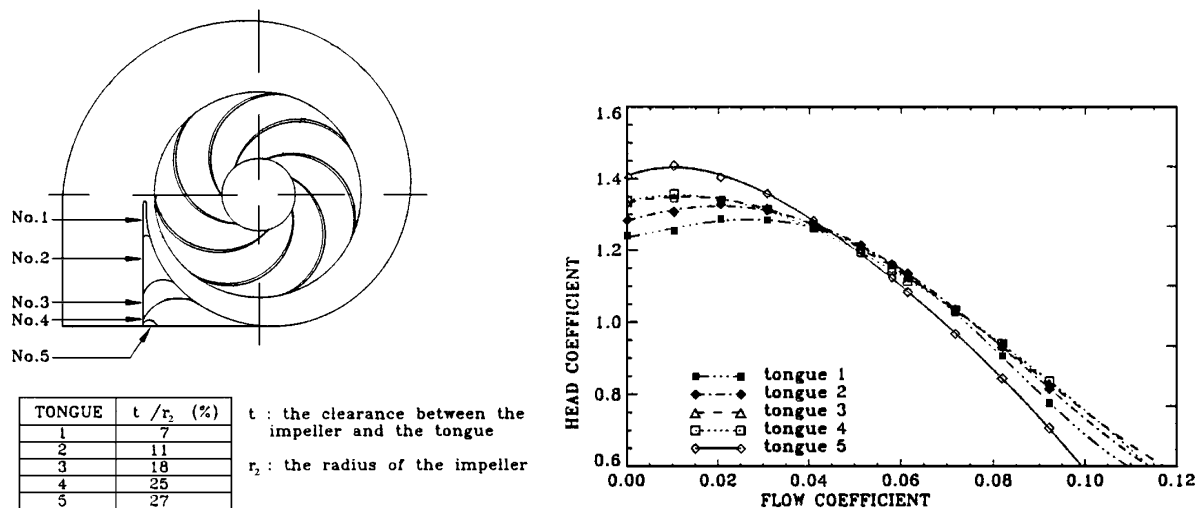


Figure 15. Different tongue shapes (left) and their effect on the overall performance of the pump (right). (Dong et al. 1997)

Ayder (1993) has carried out flow visualisations in the tongue region of a centrifugal pump volute. The visualisations show the well-known behaviour of the tongue flow at different mass flows sketched into figure 16. At the design flow the incidence angle at the tongue is approximately zero, at low mass flow the flow recirculates from the exit cone and end of the volute back to the beginning of the volute, and at high mass flow the flow from the beginning

of the volute tries to escape to the exit cone resulting in a high incidence angle at the tongue and flow separation in the exit cone.

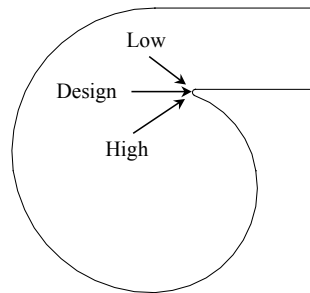


Figure 16. Typical flow direction in the tongue region of a centrifugal machine at low, medium and high flows.

Lee and Bein (1997) have investigated the flow in the volute of a radial compressor of an air conditioning system. In the numerical study Navier-Stokes equations were solved for the volute using the $k-\varepsilon$ turbulence model. For the verification of the simulation 40 static pressure taps, 5 total pressure probes and 3 dynamic pressure transducers were installed to the diffuser and volute of the compressor. The measurements and calculations were carried out at the design flow for two different tongue geometries:

1. Closed tongue, which does not allow recirculation.
2. Open tongue, which allows recirculation.

The measured compressor isentropic efficiency is reported to be 0.5 percentage points higher with the open tongue volute. Lee and Bein (1997) have found that a low-pressure zone near the tongue is present both with closed and open tongue volutes. Further they state that the largest total pressure loss occurs in the beginning of the volute downstream of the tongue. A comment can be made concerning the analysis of Lee and Bein (1997). They state that the investigation was done at the design point, but the measured and calculated static pressure distribution shows some increase along the circumference. Thus the flow seems to be smaller than the design flow of the volute.

Hosangadi et al. (2000) report a study in which the volute of Lee and Bein (1997) was further examined using a hybrid unstructured CFD-code. Flow losses are reported to be generated in the tongue region, where a strong local flow acceleration and a low-pressure region was observed. Also the transition from the diffuser to the volute is reported to generate strong vorticity and probable loss.

Dilin et al. (1998) have examined a centrifugal fan with two different rectangular volutes, one with a closed tongue and another with a cut back tongue that allows some recirculation of the flow. The volute with the closed tongue is reported to give higher pressure rise at low flow, whereas the volute with the cut back tongue performs better at high flow. A similar trend has been observed by Lipski (1979) and Copley et al. (1962) in pump volutes. At high volume flow a separated flow in the exit cone behind the tongue is reported by Dilin et al. (1998). The shortening of the tongue is shown to reduce this separated area.

Yadav and Yahya (1980) report a survey carried out in a two-dimensional volute, for which the inlet flow was produced through a swirl generating device instead of an impeller. Particular interest was paid to the tongue length and position. A long tongue located at 10° circumferential position gave the best static pressure recovery, when the flow at the volute inlet was quite tangential, representing a situation at low flow. The more radial the flow at the volute inlet turned, the shorter the optimal tongue length became. At an inlet flow angle corresponding to high flow, a tongue at 30° location was found to give the highest static pressure recovery. At high volume flow a separated flow was observed behind the tongue at the inlet of the exit cone. A shortening and rounding of the tongue reduced this separated area.

The cross-sections of the small volute channel and the exit cone intersect in the tongue area, if the volute cross-section is located at a smaller radius than the diffuser outlet. Stiefel (1972) reports that this deformation in the tongue area leads to a decrease of compressor efficiency, see figure 17.

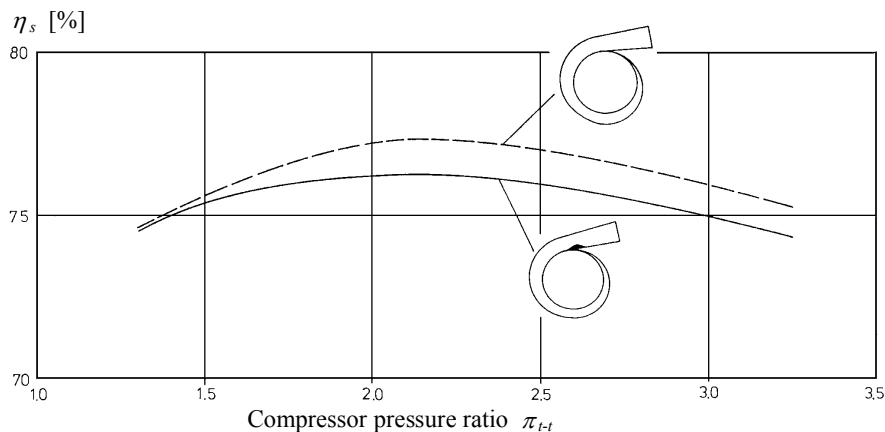


Figure 17. Decrease of the compressor efficiency due to poor tongue as a result of the intersection of the exit cone and small volute channel. (Stiefel 1972)

2.3.2 Theoretical prediction of the overall performance of the volute

Japikse (1982) presents a simple one-dimensional method for the prediction of the volute total pressure loss and static pressure recovery. The method was later complemented by Weber and Koronowski (1986). According to them the volute losses can be divided into the following categories:

1. Meridional velocity dump loss Δp_{mvdI}
2. Skin friction loss Δp_f
3. Tangential velocity dump loss Δp_{tvdI}
4. Exit cone loss Δp_e

The flow is assumed to be incompressible. It is assumed that the kinetic energy related to the radial velocity at the volute inlet is completely lost to the swirling inside the volute. This forms the meridional velocity dump loss Δp_{mvdI}

$$\Delta p_{mvdI} = \frac{1}{2} \rho c_{r3}^2 \quad (11)$$

The skin friction loss Δp_f accounts for the friction losses on the volute inner surface.

$$\Delta p_f = \xi \frac{l}{d_h} \frac{1}{2} \rho c_{u3}^2 \quad (12)$$

where l is the average path length of the fluid particles inside the volute channel and d_h the mean hydraulic diameter of the channel. The friction coefficient ξ can be found for example from Moody's chart. According to Japikse (1982) the friction loss can be neglected, but Weber and Koronowski include it in the model. Only the tangential velocity c_{u3} is used in equation (12), since the kinetic energy associated with radial velocity was already assumed to be lost according to equation (11) (Ayder 1993).

According to Japikse (1982) the tangential velocity dump loss Δp_{tvdI} occurs only when the flow decelerates in the volute. In that case the dump loss is assumed to be equivalent to the total pressure loss in a sudden expansion.

$$\Delta p_{tvdI} = \frac{1}{2} \rho c_3^2 \frac{\left(\lambda - \frac{A_3}{A_4} \right)^2}{1 + \lambda^2} = \frac{1}{2} \rho (c_{u3} - c_4)^2 \quad (13)$$

where A is the area of the flow path and λ the swirl parameter defined with equation (10). Weber and Koronowski (1986) introduce a more complicated method for calculating the tangential velocity dump loss. An intermediate station in the volute channel, denoted with 3.5, is determined at the point where 50% of the mass flow is collected by the volute. First the real through flow velocities in stations 3.5 and 4 are calculated

$$\begin{aligned} c_{3.5} &= \frac{q_{v4}}{2 A_{3.5}} \\ c_4 &= \frac{q_{v4}}{A_4} \end{aligned} \quad (14)$$

Then two fictive tangential velocities at the diffuser exits $c_{u\ 3\leftarrow 3.5}$ and $c_{u\ 3\leftarrow 4}$ are calculated using the conservation of the angular momentum and the real velocities $c_{3.5}$ and c_4 .

$$\begin{aligned} c_{u\ 3\leftarrow 3.5} &= c_{3.5} \frac{r_{3.5}}{r_3} \\ c_{u\ 3\leftarrow 4} &= c_4 \frac{r_4}{r_3} \end{aligned} \quad (15)$$

where r_3 is the radius of the diffuser outlet and $r_{3.5}$ and r_4 are the radii of the centre of the volute channel measured from the impeller shaft. The tangential velocity dump loss is then calculated in two parts.

$$\begin{cases} \Delta p_{\text{tvd}l\ 3.5} = K_T \frac{1}{4} \rho (c_{u3}^2 - c_{u3\leftarrow 3.5}^2) & , \text{ if } c_{u3} \geq c_{u3\leftarrow 3.5} \\ \Delta p_{\text{tvd}l\ 3.5} = \frac{1}{4} \rho (c_{u3} - c_{u3\leftarrow 3.5})^2 & , \text{ if } c_{u3} < c_{u3\leftarrow 3.5} \end{cases} \quad (16)$$

and

$$\begin{cases} \Delta p_{\text{tvd}l\ 4} = K_T \frac{1}{4} \rho (c_{u3}^2 - c_{u4}^2) & , \text{ if } c_{u3} \geq c_{u3\leftarrow 4} \\ \Delta p_{\text{tvd}l\ 4} = \frac{1}{4} \rho (c_{u3} - c_{u4})^2 & , \text{ if } c_{u3} < c_{u3\leftarrow 4} \end{cases} \quad (17)$$

where the coefficient $K_T = 0.5$ for volutes and $K_T = 1.0$ for plenums. Finally the tangential velocity dump loss is obtained by adding the two components.

$$\Delta p_{\text{tvd}l} = \Delta p_{\text{tvd}l\ 3.5} + \Delta p_{\text{tvd}l\ 4} \quad (18)$$

The exit cone loss Δp_e could be calculated according to any appropriate diffuser performance prediction method presented for example by Japikse (1984). Weber and Koronowski (1986) propose a standard gradual expansion model

$$\Delta p_e = K_E \frac{1}{2} \rho (c_4 - c_5)^2 \quad (19)$$

in which the exit cone loss coefficient K_E ranges from 0.15 for exit cones with an opening angle of about 10° up to 1.1 for exit cones with an opening angle of 60° . In a well-designed exit cone the opening angle should not exceed 10° , so a constant value of 0.15 is proposed by Weber and Koronowski (1986).

Finally the overall total pressure loss of the volute and exit cone is obtained by adding the different components together.

$$\Delta p_{3 \rightarrow 5} = \Delta p_{mvd} + \Delta p_f + \Delta p_{tvd} + \Delta p_e \quad (20)$$

Van den Braembussche et al. (1999) have developed a more sophisticated model for the analysis of the performance of volutes. It predicts the non-uniformity of the flow variables around the circumference and takes into account the vortical structure of the flow inside the volute channel. The model includes the following components:

- **Rotor response calculation** to predict the circumferential velocity distribution at the impeller outlet (c_{r2} and c_{u2}) as a result of the non-uniform static pressure distribution.
- **Diffuser flow calculation** to predict the circumferential distribution of the flow variables at the diffuser outlet.
- **Volute flow calculation** to approximately calculate the three-dimensional flow inside the volute. It predicts the volute losses, static pressure rise and the static pressure distribution along the circumference.
- **Impeller outlet pressure calculation** to predict the circumferential total pressure distribution at the impeller outlet.
- **Exit cone flow calculation** to predict the performance of the exit cone. The model takes into account the swirling, non-uniform flow at the exit cone inlet.

The calculation is done at several positions around the circumference (typically 36). In addition, each cross-section of the volute channel is divided into several co-centric ellipses, which are further divided into four quadrants, see figure 18. Mass and momentum balances are constructed for each control volume obtained using the above-mentioned discretisation. The different parts of the model are iterated until a convergence is reached. Only the exit cone

flow calculation is performed once, after the volute calculation is finished. The model has been tested with several different volutes, both internal and external, and is reported to predict the overall performance of the volute well. (Van den Braembussche et al. 1999)

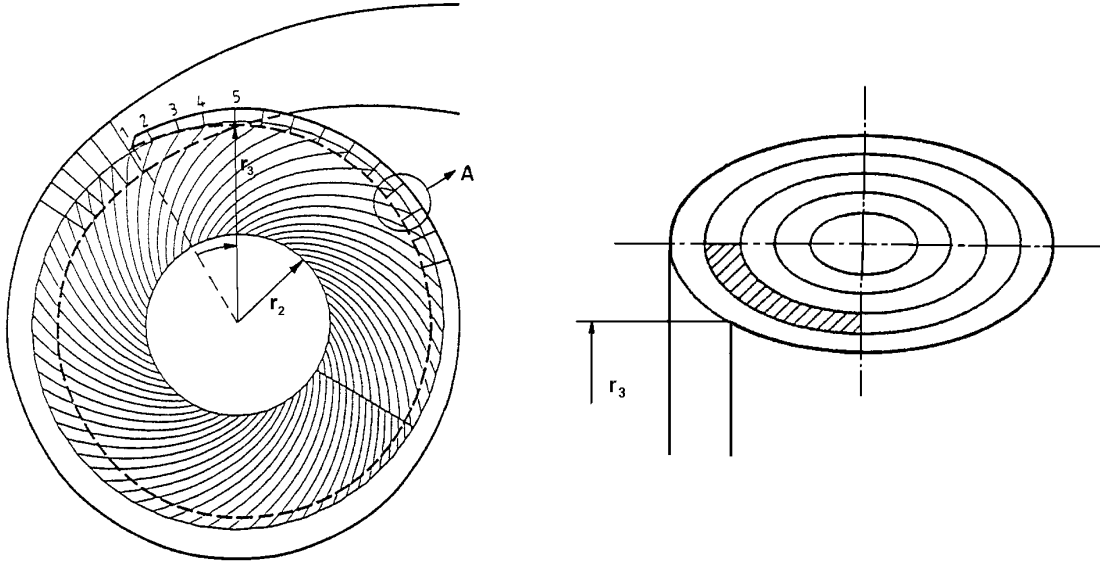


Figure 18. The discretisation of the diffuser and volute in the volute flow model of Van den Braembussche et al. (1999).

2.3.3 The mechanical effects of the volute on the compressor

The non-uniformity of the flow caused by the volute has mechanical effects on the compressor, such as radial force and vibrations. According to Stepanoff (1957) the radial force F_r of a centrifugal pump can be calculated from

$$F_r = K_r p_{t\ out} d_2 b_2 \quad (21)$$

where $p_{t\ out}$ is the total pressure at the pump outlet, d_2 the diameter of the impeller and b_2 the height of the impeller. The non-dimensional coefficient K_r varies from pump to pump and can be determined experimentally. For a pump with a volute Stepanoff suggests

$$K_r = 0.36 \left(1 - \left(\frac{q_v}{q_{v\ des}} \right)^2 \right) \quad (22)$$

and for a pump with a constant area casing (collector) he proposes

$$K_r = 0.36 \left(\frac{q_v}{q_{v\ des}} \right) \quad (23)$$

where q_v is the volume flow in the operating point in question and $q_{v, des}$ the volume flow at the design point. Equations (21) and (22) yield to a zero force at the design flow and maximum positive force at zero flow, whereas equations (21) and (23) result in a null force at shut off and maximum force at high flow. Other researchers (Agostinelli et al. 1960, Moore and Flathers 1998) have shown that K_r cannot be expressed in such a simple manner only as a function of the volume flow as Stepanoff proposes. Thus the above mentioned equations for the coefficient K_r are not suitable for a compressor analysis without modifications. However, equation (21) describes the main parameters influencing the radial force quite well.

Moore and Flathers (1998) present an experimental technique to quantify the radial force in turbomachinery operating on fluid film bearings. They have used this method to measure the radial loads of a centrifugal pipeline boost compressor equipped with oil lubricated titling pad bearings both in a laboratory and on the field. The radial force is found to be the highest at low flow close to the surge. As the flow rate is increased, the force is reduced until a minimum force is reached somewhat above the design flow. The force rises again towards the choke line, but stays well below that of the surge line at all conditions.

Flathers and Bache (1996) present a numerical study of the centrifugal pipeline boost compressor that was measured by Moore and Flathers (1998). The shrouded impeller, the vaneless diffuser and the volute was modelled with a commercially available CFD-code, TASCflow. The solution was obtained by time averaged, fully 3-dimensional, viscous calculation utilising the standard $k-\varepsilon$ turbulence model. The aerodynamic performance of the compressor (pressure ratio and efficiency) was predicted well. The results of the force calculation were of correct order of magnitude, but showed moderate difference between the measured and calculated values. The authors conclude that the radial force was difficult to predict correctly and explain it partially by the fact that the inlet volute was not included in the model.

Strain gage and mechanical vibration measurements were made in a six-stage centrifugal compressor by Sorokes et al. (1998). The strain gages on the impeller showed a peak response at 1.0 times the compressor running speed. The blades were excited by the pressure non-uniformity caused by the volute, which was found to be the strongest at high mass flow. This was suspected to be one possible cause for impeller failures detected in the investigated type of compressors.

Hagelstein et al. (1997) have also shown how a change in the circumferential pressure distribution influences the impeller blade vibrations. Asymmetrically adjusted diffuser vanes have been shown to have a favourable effect on the pressure field and blade vibrations.

Fatsis et al. (1997) present a time-accurate computational method for analysing the flow and forces in radial impellers under non-uniform outlet conditions produced for example by the volute. The impeller force was calculated in two different ways: by integrating the pressure forces over the impeller surface and by applying the pressure and momentum balance over a control volume, which contained the space between the impeller inlet and outlet. The first method allowed the calculation of the oscillating force in single blades, whereas the latter method allowed the division of the net force into components caused by the non-uniformity of the static pressure, radial momentum and tangential momentum. Fatsis et al. (1997) have calculated two different centrifugal compressor impellers at high mass flow, one with radial ending blades and the other with 40° backward lean angle. They found that the integration of the static pressure distribution at the impeller outlet gave a good approximation of the net radial force for the impeller with backward leaned blades. However, for the impeller with radial ending blades, the force of the radial momentum compensated the pressure force to a great extent. Thus the pressure measurement alone is not suitable for determining the radial force of impellers with radial ending blades.

Antila et al. (1996) describe the design of a single-stage centrifugal compressor equipped with active magnetic bearings. The properties of the bearings and impeller force measurements using magnetic bearings are reported. Axial force is found to vary almost linearly with the pressure ratio, which is typical for a centrifugal compressor. The measured radial force is found to be a function of the mass flow, but independent of the rotational speed. The radial force is the highest at choke and decreases toward small flow, reaching the minimum somewhat below the design flow. Close to the stall limit the radial force increases slightly again. A comment is due here: the reported radial force certainly is independent of the rotational speed, when the flow is considered as a relative flow rate between the choke and stall limits. Naturally the absolute mass flow varies with the speed, so in that sense the radial force cannot be held totally independent of the speed.

Baun and Flack (1999) report the design and test run of a plexiglass research pump equipped with magnetic bearings for hydraulic force measurement. The axial and radial magnetic bearings, their control system and the data acquisition system were designed especially for static and dynamic force measurements. The axial force was found to be the highest at shut off. From there it decreased steadily towards higher flow (smaller head) with the exception of two local maxima located at 0.75 and 1.0 times the design flow coefficient. The radial force was also found to be the highest at shut off and to decrease steadily until the minimum was reached at the design flow. At flow rates higher than the design flow, the net radial force increased again.

2.3.4 Detailed flow investigations in the volute

The flow structure in the volute is strongly affected by the vortex flow that forms into the volute channel as a consequence of the radial velocity at the volute inlet. Different vortex patterns are observed in the volute depending on the shape and operating point of the volute. In vortex flows two basic vortex structures can be distinguished:

- Solid body vortex i.e. forced vortex, left side of figure 19.
- Free vortex flow, right side of figure 19.

Often in a real flow a combination of the above mentioned vortex structures is present.

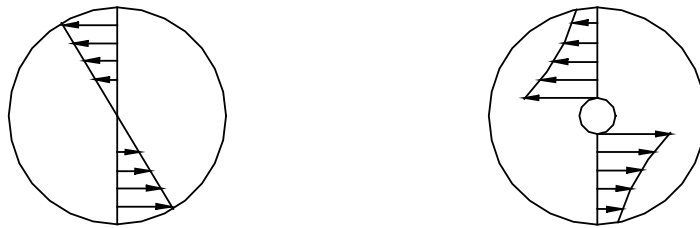


Figure 19. The two basic vortex structures: forced vortex i.e. solid body vortex on the left and free vortex flow on the right.

Van den Braembussche and Hande (1990) report a study, where static pressure measurements and three-hole probe traverses were made in a straight conical pipe representing a volute channel. Also an analytical model for the flow in a straight volute is presented. The authors found that the fluid entering the volute close to the tongue at a small radius filled the centre of the volute. New fluid entering the volute further downstream at a larger radius wrapped around the upstream fluid. Thus the swirl velocity was approximately constant in the outer part of the cone, and no free vortex type of flow was observed. In the centre of the cone a

forced vortex flow was seen. The through flow velocity showed a large crosswise variation, having a maximum at high flow and minimum at low flow in the volute centre. The strongly increased through flow velocity in the volute centre is reported to explain the odd-sounding observation of Stiefel (1972) that the volute should be designed with a negative blockage, i.e. that the area of the cross-section should be 10 - 15% smaller than the frictionless computed one.

Ayder (1993) has thoroughly investigated the flow inside three different volutes: a rectangular external volute of a pump, a rectangular internal volute of a compressor and an elliptic volute of a compressor. The results of measurements made in a rectangular compressor volute are also reported in Ayder and Van den Braembussche (1991) and measurements carried out in an elliptic compressor volute in Ayder et al. (1993). A numerical survey of the elliptic compressor volute is presented also in Ayder and Van den Braembussche (1994). According to all these studies a forced vortex flow is present in the volute channel. In the beginning of the volute (at a small circumferential angle) a forced vortex forms due to shear stresses in the middle of the channel, which results in high losses in that position. At the bigger circumferential angles two separate mechanisms are reported to be responsible for the forced vortex flow. At high volume flow the forced vortex further in the volute is a result of the increasing radial velocity along the circumference and the way the volute is filled with the fluid. As the new fluid with a higher radial velocity wraps around the fluid already in the volute, the forced vortex forms automatically. Thus it is not caused by energy dissipation due to the shear stresses in the middle of the channel. This results in smaller losses in the middle of the volute channel than one could assume at a first glance. At low flow, however, a different mechanism is present. Because the radial velocity stays practically constant along the circumference, the shear stresses in the middle of the volute channel must mainly be responsible for the forced vortex flow. This causes high total pressure loss in the volute channel. (Ayder et al. 1993)

The static pressure distribution in the volute is affected mainly by the centrifugal forces due to swirl velocity and those due to through flow velocity (Ayder 1993). At high flow the strong swirl velocity is dominant, and causes a low static pressure into the middle of the volute cross-section. At low flow the swirl velocity and centrifugal forces caused by it are weak. Thus the through flow velocity together with the circumferential curvature of the volute channel result in a low static pressure close to the inner wall of the volute. The maximum through flow

velocity was observed close to the volute centre or inner wall depending on the operating point. This corresponds to the low static pressure zones observed in the volute. (Ayder et al. 1993)

Secondary vortices in rectangular volutes have been reported by Ayder (1993). In the external pump volute a counter-rotating vortex formed next to the lower outer corner, left side of figure 20. In the internal compressor volute a secondary vortex was observed close to the inner wall above the diffuser, right side of figure 20. Both vortices are explained to be caused by the radial pressure gradient, which is the result of the centrifugal force caused by the circumferential curvature of the volute channel and through flow velocity. When the low energy fluid in the boundary layer is subjected to the radial pressure gradient, it can no longer follow the main swirl direction, but turns back towards the lower pressure. (Ayder 1993)

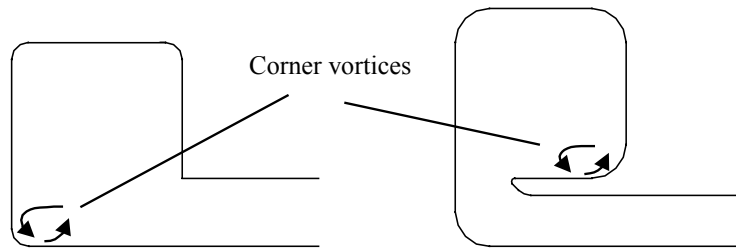


Figure 20. The corner vortices observed in the rectangular volutes by Ayder (1993). External pump volute on the left and internal compressor volute on the right.

Ayder (1993) discusses also the leakage flow through the tongue gap. The axial height of the volute channel was constant in both of the rectangular volutes examined by Ayder, because the variation in the cross-sectional area was obtained merely by increasing the radial width of the channel along the circumference. This leads to a high tongue gap, through which a substantial leakage flow is able to pass. At low flow the low energy fluid that is accumulated close to the inner wall of the volute flows through the tongue gap and fills up to 50% of the beginning of the volute. This shifts the centre of the typical forced vortex in the small circumferential angles especially with the internal volute. (Ayder 1993)

In the numerical work of Ayder and Van den Braembussche (1994), fully three-dimensional flow in the elliptic compressor volute was simulated using a modified Euler solver. To estimate some of the friction effects, wall shear stress forces and second-order dissipation were added to the Euler solver, but otherwise the flow was treated as frictionless. The numerical results confirmed the filling mechanism of the volute presented in Van den

Braembussche and Hande (1990). Also the main flow structure observed in the experiments was captured by the model. Only the high losses in the vortex core in the beginning of the volute channel were not reproduced.

Hagelstein et al. (2000) report an experimental and numerical investigation of a rectangular external compressor volute. Five-hole probe measurements were made in the volute channel to obtain the main flow structure, which was found not to be very much different from the one reported by Ayder (1993). The static pressure and through flow velocity distributions were seen to have the same basic structure as the ones observed by Ayder. The local total pressure loss coefficient is reported to be high particularly in the centre of the volute cross-section, due to accumulation of the low energy fluid into the vortex core as a result of the static pressure gradient. The swirl velocity distribution, however, showed some difference to Ayder (1993). Instead of linear increase of the swirl velocity, as in the plain forced vortex flow, a strong increase in the vortex core, but only a mild increase in the outer part of the cross-section was seen. Thus the swirl distribution approached the one reported by Van den Braembussche and Hande (1990). The corner vortices apparently present in the rectangular volute are given as reasons for the observed swirl pattern by Hagelstein et al. (2000).

The numerical study presented by Hagelstein et al. (2000) was made with the same modified Euler solver as the work of Ayder and Van den Braembussche (1994). The calculation domain included the vaneless diffuser, volute and exit cone. The simulation slightly over-predicted the static pressure non-uniformity caused by the volute. The flow structure inside the volute is reported to be quite close to the measured one apart from the loss in the vortex core in the volute centre, which was not fully captured. The numerical simulation showed also distinct flow separation in the end of the volute and in the exit cone. (Hagelstein et al. 2000)

Hubl (1975) reports a thorough analytical and experimental investigation of different compressor volutes. Two circular external volutes were measured, one with a tangential inlet and another with a symmetric inlet. The flow at the vaneless diffuser outlet was measured in 15 circumferential locations, and the three-dimensional flow in the volute was measured with a four-hole probe in seven circumferential locations at four different mass flows.

Hubl (1975) observed the following flow pattern in the circular volute with the tangential inlet, see the left side of figure 21. A forced vortex type of swirl was present at low flow apart

from the small area in the beginning of the volute. At a slightly higher mass flow rate the flow pattern resembled the one reported by Hagelstein et al. (2000) i.e. a sharp increase of the swirl velocity in the middle and a mild increase in the outer part of the volute channel. At high mass flow the swirl pattern was close to the one observed by Van den Braembussche and Hände (1990), in which the swirl velocity increases very sharply in the middle of the channel and stays constant in the outer part of the channel. The through flow velocity profile had a maximum between the inner wall and the middle of the volute channel. At low flow the profile was relatively flat, whereas at high flow a strong acceleration in the middle was observed. The total pressure distribution showed a minimum in the middle of the channel at all flows. The static pressure distribution showed as well a minimum in the middle. The more the mass flow increased, the more sharply the static pressure decreased towards the middle. Hübl (1975) draws attention to the high velocity gradient at the volute inlet, where new fluid with high radial velocity enters the volute and mixes with the more slowly swirling flow already in the volute. This is assumed to cause considerable loss by Hübl.

In the circular volute with the symmetric inlet, see the right side of figure 21, quite a different flow structure has been reported by Hübl (1975). The swirl pattern consisted of two counter-rotating forced vortices with each of them having a linear swirl velocity profile, see figure 21. The static pressure distribution was almost constant across the volute cross-section. Also the total pressure showed quite a constant distribution with a small local increase in the middle and two weak minima at both sides of the peak close to the vortex cores. The through flow velocity profile was constant at low flow. At high flow two distinct peaks were observed in the through flow velocity in the same locations where the vortex cores were, and a local minimum was seen in the middle.

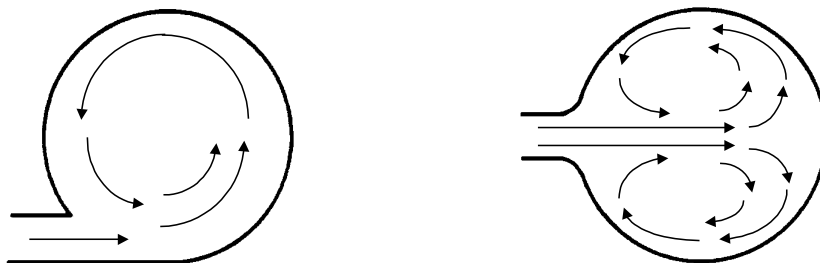


Figure 21. The vortex structures in the volutes measured by Hübl (1975). The single vortex in the volute with a tangential inlet on the left and the double vortex in the volute with a symmetric inlet on the right.

Fahua et al. (2000) have used a commercial CFD-code to study the flow in a vaneless diffuser and volute of a pipeline compressor. The investigated volute had almost circular cross-section and a tangential inlet. The flow was calculated as viscous and three-dimensional, and the standard $k-\varepsilon$ turbulence model with a wall function was used. Only one blade passage of the impeller was modelled and the flow quantities at the impeller exit were averaged in the circumferential direction. This prevents detailed examination of the phenomena caused by the circumferential non-uniformity of the volute, but offers a relatively simple and quick analysis of the complete compressor. Special attention was paid to the flow structure in the volute and to the axial distortion of the flow quantities in the diffuser. At low and design mass flows a forced vortex was observed in the volute channel. At the design flow a narrow zone of free vortex flow was also seen on the wall in few circumferential locations. At high mass flow quite a different double vortex flow pattern is reported in the beginning of the volute up to the 180° circumferential position. Although the volute had a tangential inlet, the flow in this region resembled quite much the one measured by Hübl in a symmetric volute. The static pressure recovery and total pressure loss of the diffuser are reported to have an axial i.e. spanwise variation. Both the static pressure recovery and total pressure loss are stronger on the shroud side and weaker on the hub side of the diffuser. This is reported to be an indication of the upstream effect of the volute. (Fahua et al. 2000)

Dilin et al. (1998) report an investigation of two rectangular fan volutes with symmetric inlets, one with a closed tongue and another with a cut back tongue that allows recirculation. In fans the diffuser is often omitted, as in pumps. In this case, however, a short vaneless diffuser with a radius ratio of 1.37 was used. In the numerical part a commercial CFD code was used to analyse the viscous incompressible flow. The $k-\varepsilon$ model with a wall function was used to model the turbulence. Circumferentially uniform boundary condition was given at the diffuser inlet. In the experimental part the three-dimensional flow structure in the volute channels was measured with a five-hole probe in numerous circumferential positions. Also flow visualisations in the tongue region were performed. According to Dilin et al. (1998) the flow structure in the volute channel depends on the flow rate and tongue configuration. In the volute with the closed tongue, two counter-rotating vortices were seen like in the experiments of Hübl (1975), see the right side of figure 21. In the volute with the cut back tongue, a similar twin vortex pattern was present at high and medium flows. At low flow, however, a single vortex just as in the volutes with tangential inlet, left side of figure 21, was seen. This is likely to be caused by the recirculation of the flow. At low mass flow the pressure gradient pushes

fluid from the end of the volute and from the exit cone back into the beginning of the volute. This recirculating fluid fills the beginning of the volute and affects strongly the development of the vortex structure.

3 EXPERIMENTAL FACILITIES

3.1 Test compressor

The test compressor was a single-stage radial compressor originally designed for producing vacuum for paper and pulp mills, see figure 22. In its design point the compressor produces 50 kPa vacuum at the inlet and exhausts into ambient air pressure.

The compressor is driven directly by a 175 kW high speed electric motor that is supplied with variable frequency AC-current by a 200 kW inverter. No gearbox is needed in this single shaft construction and the use of an inverter allows variable speed control from zero rpm to full speed. The compressor is totally oil free as active magnetic bearings are used. The compressor shaft lies vertical in order to minimise radial bearing loads.

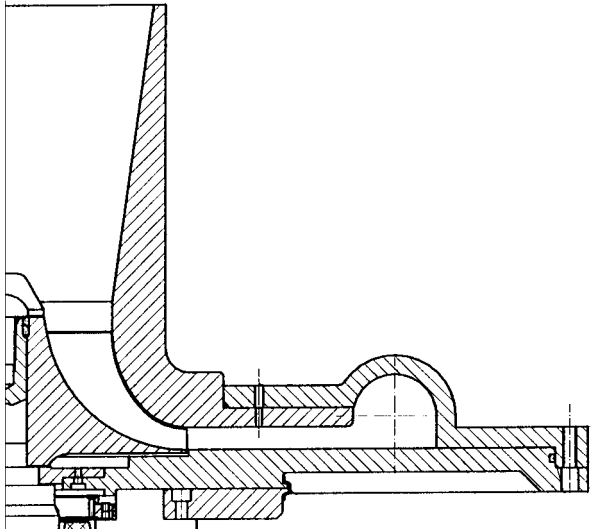


Figure 22. Test compressor. Photo: Petri Sallinen / LUT

The specific speed of the compressor, defined according to equation (24), is $N_s = 0.90$.

$$N_s = \frac{\Omega \sqrt{q_{v1}}}{\Delta h_s^{0.75}} \quad (24)$$

where Ω is the angular velocity, q_{v1} the inlet volume flow and Δh_s the isentropic enthalpy rise. The unshrouded impeller has got seven full blades and seven splitter blades with 30 degrees backsweep at the trailing edge measured from the radial direction. The diameter of the impeller is $d_2 = 309$ mm. An unpinched vaneless diffuser with a diameter ratio of $d_3/d_2 = 1.90$ and constant height $b = 20.4$ mm is used to connect the impeller to the volute.

3.2 Volutes

3.2.1 Original volute

The original volute was designed for easy and cost effective industrial assembly. The shape of its cross-section was rectangular in the bottom and semi-circular in the top. The area distribution of the cross-section was designed for a constant static pressure at the design point assuming frictionless flow. Figure 23 shows a photo of the original volute taken from the exit cone and the shape of the cross-section at the 96° and 180° circumferential locations. The tongue, which was located at $\theta = 33^\circ$, is seen in the lower left corner of the photo. The tongue shape is simple, since the intersection of the small and big volute channel is simply a vertical line. The volute was made of stainless steel by casting and the inner surface was left unpolished. The surface roughness was measured to be approximately $R_a = 6 - 9 \mu\text{m}$.

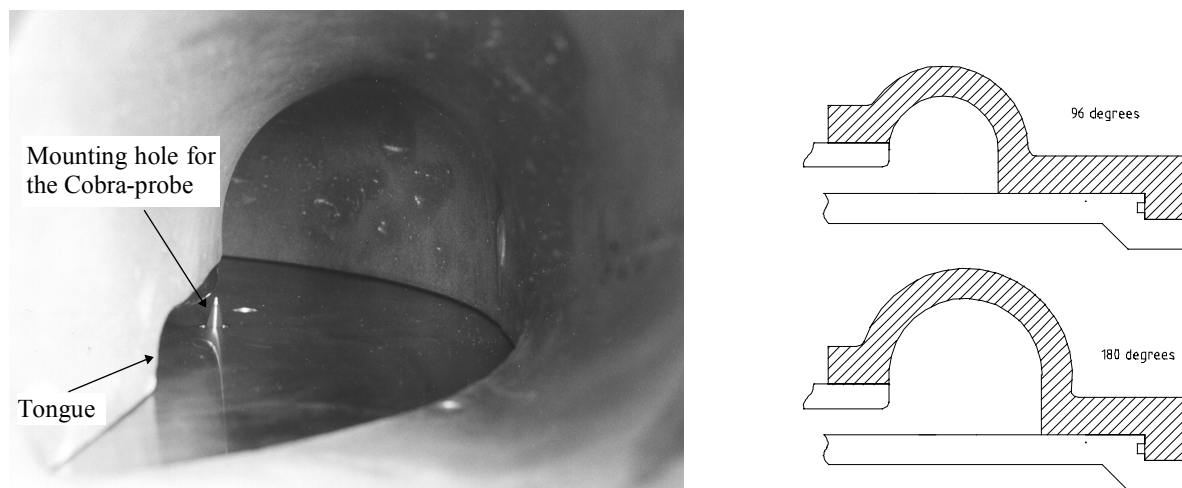


Figure 23. Original volute and its cross-sections at different circumferential locations. Photo: Petri Sallinen / LUT

3.2.2 Circular volute

The circular volute was designed in order to find out the influence of the square edged bottom to the volute flow. The shape of the cross-section was chosen to be as close to a circle as possible and can be seen in figure 24. Because the new volute had to be fitted to the original compressor, the diameter ratio of the vaneless diffuser had to be increased by 6.8% to $d_3/d_2 = 2.03$. The circular volute had the same variation in the cross-sectional area as the original one.

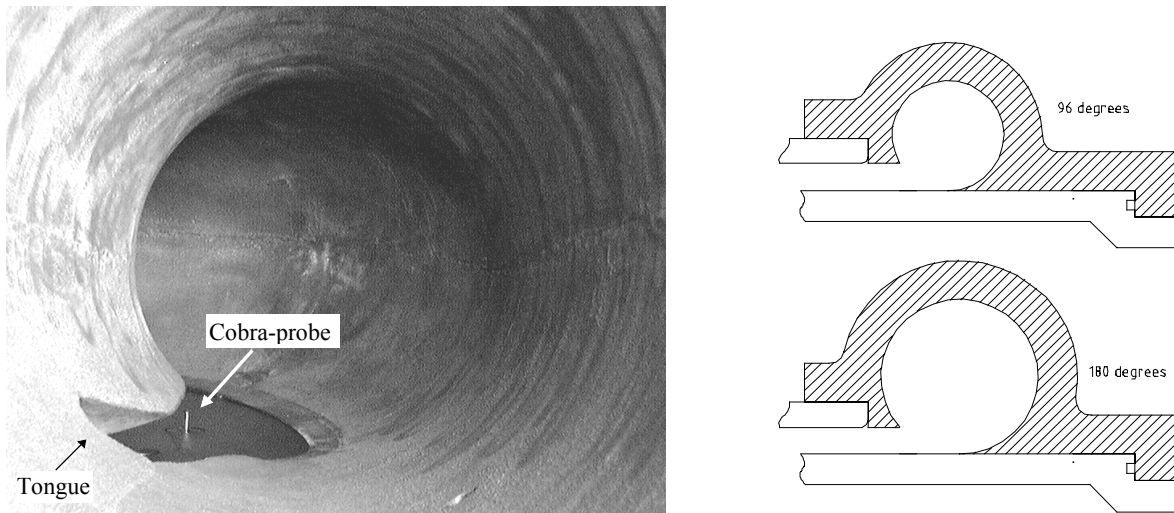


Figure 24. Circular volute and its cross-sections at different circumferential locations. Photo: Timo Mikkola / LUT

The shape of the tongue of the circular volute was let to have the form which is created when a small and a big circular volute channel intersect. Thus the tongue became semi-elliptic and sharp-edged and was located at $\theta = 30^\circ$, see figure 25. It was anticipated that the small "hump" at the lower part of the tongue and the sharp edge would not be the optimal shape, especially at off design conditions. However, the tongue was left as it was, because no exact information about the optimum shape was available at that time and it is always easier to remove material than to add it afterwards. The circular volute was cast from aluminium, since it was to be used only in the test compressor operated with clean air. The surface was left unpolished, but due to the difference in material and casting method, the surface was somewhat rougher than in the original volute. The average measured surface roughness in the volute was $R_a = 16 - 19 \mu\text{m}$ and in the exit cone $R_a = 13 \mu\text{m}$.

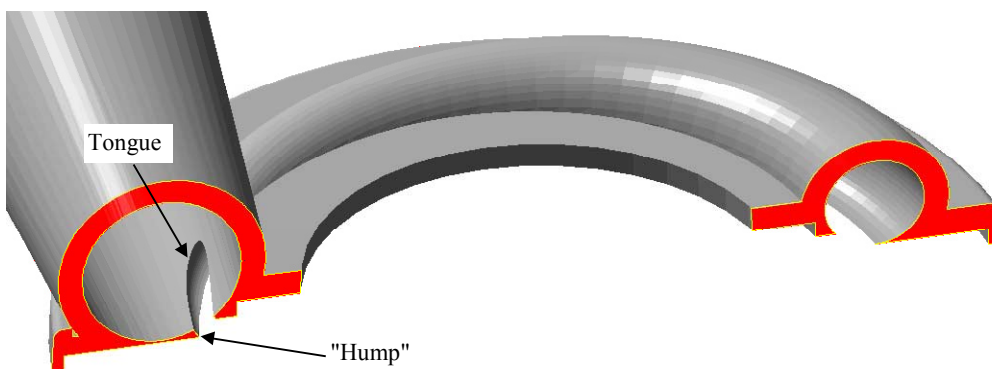


Figure 25. Semi-elliptic and sharp-edged tongue of the circular volute.

3.2.3 Modified circular volute

The circular volute was later modified in order to investigate the effect of the shape of the volute tongue on the performance of the volute. The sharp and semi-elliptic tongue was rounded and the "hump" from the lower part of the tongue was removed. The modified tongue of the circular volute is shown in figure 26. The shape of the tongue is almost linear and the thickness is considerably increased especially at the lower and upper parts of the tongue. Only in the middle of the tongue a relatively sharp edge still exists. In the modification the tongue was moved slightly further into the 32.5° circumferential position, being now at about the same location as the tongue of the original volute. The slightly shortened and rounded tongue was assumed to tolerate larger incidence angles resulting in increased performance at off design conditions. In addition, the circular volute was smoothed in order to allow fair comparison of the original and circular volutes. The average surface roughness was $R_a = 5 - 8 \mu\text{m}$ after the smoothing.

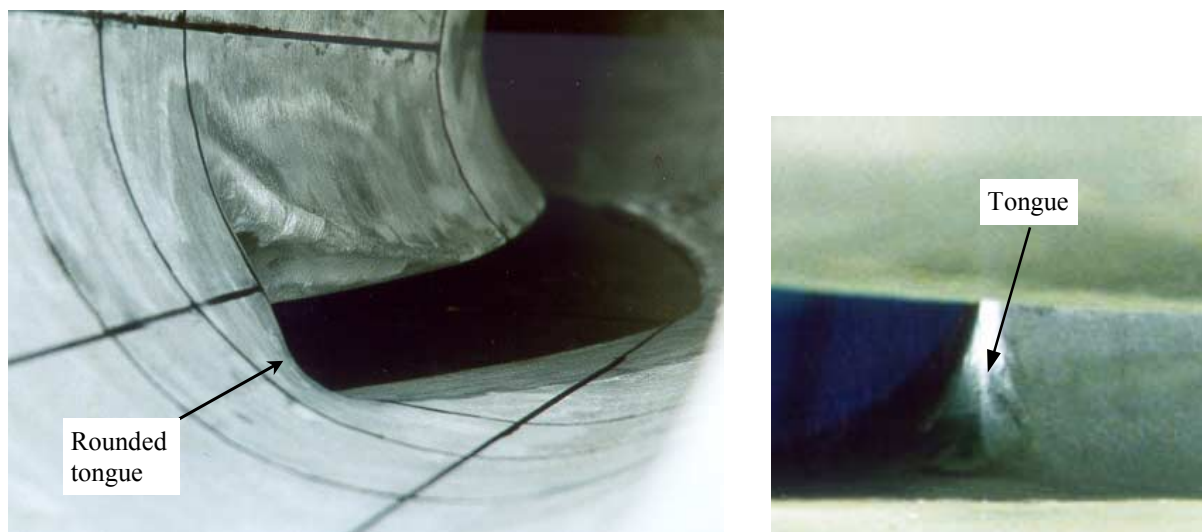


Figure 26. The tongue region of the modified circular volute (left) and a view from the vaneless diffuser towards the tongue (right). Photo: Petri Sallinen / LUT

3.3 Measuring equipment and data acquisition

3.3.1 Compressor test stand

The experiments were carried out in the Laboratory of Fluid Dynamics at Lappeenranta University of Technology. The lay-out of the test facility can be seen in figure 27. The open loop test stand has two throttling valves, valve A upstream and valve B downstream of the

compressor, in order to allow measurements of both vacuum and overpressure compressors. In this study the measurements were done in the vacuum mode i.e. valve B was fully open and the compressor was throttled using valve A. The outlet pipe of the test stand was insulated to ensure correct temperature measurement.

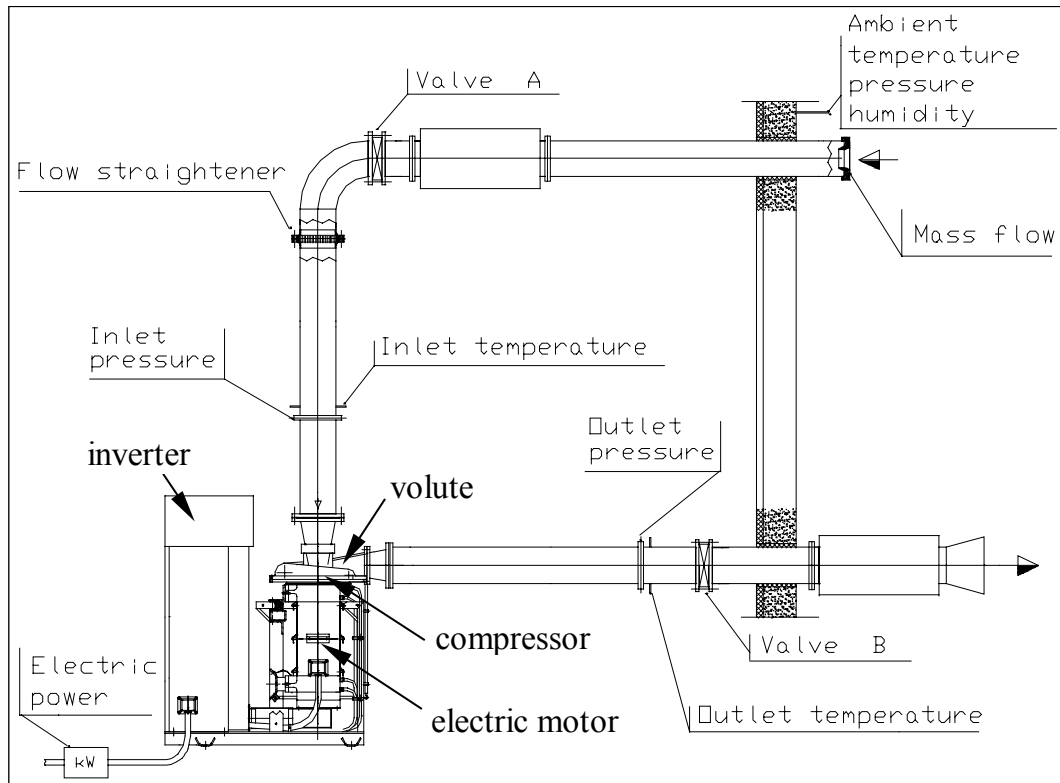


Figure 27. Compressor test facility.

The overall performance of the compressor was measured using the instrumentation of the test stand, which allows the measurement of ambient temperature, pressure and humidity, mass flow, inlet total temperature and total pressure, outlet total temperature and total pressure, rotational speed and input power, see figure 27. The mass flow was measured at the beginning of the inflow pipe according to VDI 2041 with an ISA 1932 nozzle made according to DIN 1952. The analogue signals of the thermoelements, pressure transducers, humidity meter, tachometer and power analyser were collected into a Fluke Hydra data logger, which was connected to a PC via an RS-232 serial cable. With an in-house developed data acquisition program the compressor can be monitored on-line and the necessary data can be saved. The instrumentation of the test stand and the performance calculations were made according to the following standards: ISO 5389, ASME PTC 10 and VDI 2045 Part 1 and 2.

3.3.2 Pneumatic probe and static pressure taps

The flow inside the compressor was measured using a miniature three-hole Cobra-probe manufactured by Concepts ETI. The probe head, the left side of figure 28, was about 2 mm wide and less than 1 mm high, so it barely disturbed the flow. The Cobra-probe allows the measurement of static pressure, total pressure and flow direction on a plane. During the measurement the probe was first nulled i.e. turned directly towards the flow, after which the pressures in each hole were recorded. The probe was calibrated by the manufacturer and the calibration sheet is attached in appendix A.

A manual traversing gear was used to position the probe in the desired location, the right side of figure 28. It allowed the probe to be moved axially and rotated about its axis. The axial position could be read from the instrument with an accuracy of 0.05 mm and angular position with an accuracy of 0.2° . The Cobra-probe was traversed at the diffuser exit in three different circumferential positions: 90° , 180° and 360° for the original volute and 78° , 168° and 348° for the circular and modified circular volutes. The reason for the different traversing positions for the different volutes is that the traversing gear needs a certain room for its attachment. The difference in the radius of the diffuser was not enough, so the mounting holes had to be separated also circumferentially. The circumferential location of $270^\circ/258^\circ$ was left out because it was impossible to fit the traversing gear there because of the compressor mountings.

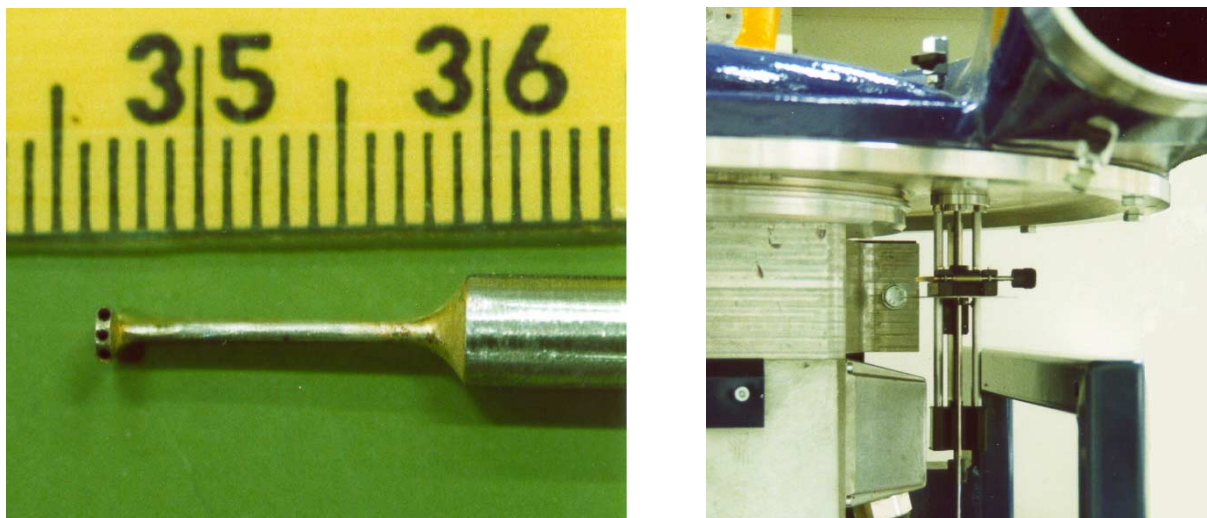


Figure 28. The head of the Cobra-probe (left) and the traversing gear installed onto the diffuser hub wall (right). Photo: Petri Sallinen / LUT

The static pressure distribution on the volute and exit cone surface was measured using seven static pressure taps positioned at the volute top. The static pressure distribution at the impeller exit / diffuser inlet was measured using eight static pressure taps located on the shroud surface of the vaneless diffuser at diameter ratio $d/d_2 = 1.014$. The static pressure tap and Cobra-probe traversing positions can be seen in figure 29.

3.3.3 Flow visualisation

The flow in the beginning of the exit cone was visualised using tufts. Pliant, fluorescent orange tufts were taped with heatproof aluminium tape on the exit cone surface in three rows denoted with letters A, B and C. The tuft rows were located 200, 250 and 300 mm away from the $0^\circ/360^\circ$ line, see figure 29. The first row A was at the level of the tongue in the original and modified circular volutes and about 20 mm downstream from the tongue in the circular volute. The tuft positioning and numbering in the different volutes is shown in figure 30. In the original volute an additional tuft was positioned next to row 3 due to the longer periphery of the square edged inner lower corner. In addition, an internal flow visualisation was made. To enable this one tuft was attached to a thin-tipped stick and was traversed across the exit cone from bottom to top starting from the position of the surface tuft B5.

Two holes were made on the exit cone wall in order to allow the observation of the tufts. One hole was used to insert an borescope into the exit cone while the other one was housing a small halogen light bulb to provide necessary illumination. The movement of the tufts was recorded with a digital video camera through the borescope. Only one tuft could be seen at a time due to the limited viewing angle of the borescope.

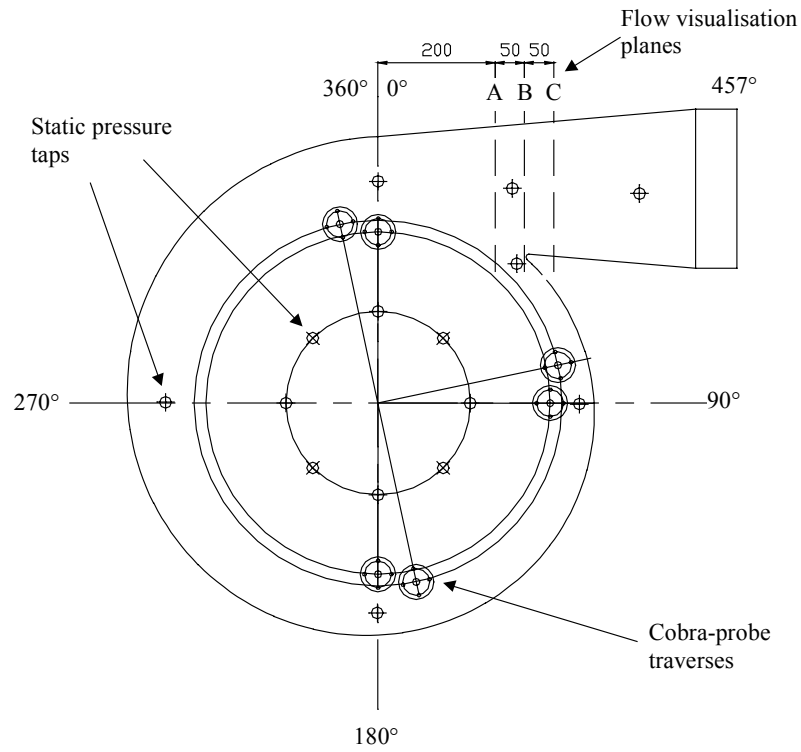


Figure 29. Location of the static pressure taps, Cobra-probe traverses and flow visualisation tufts.

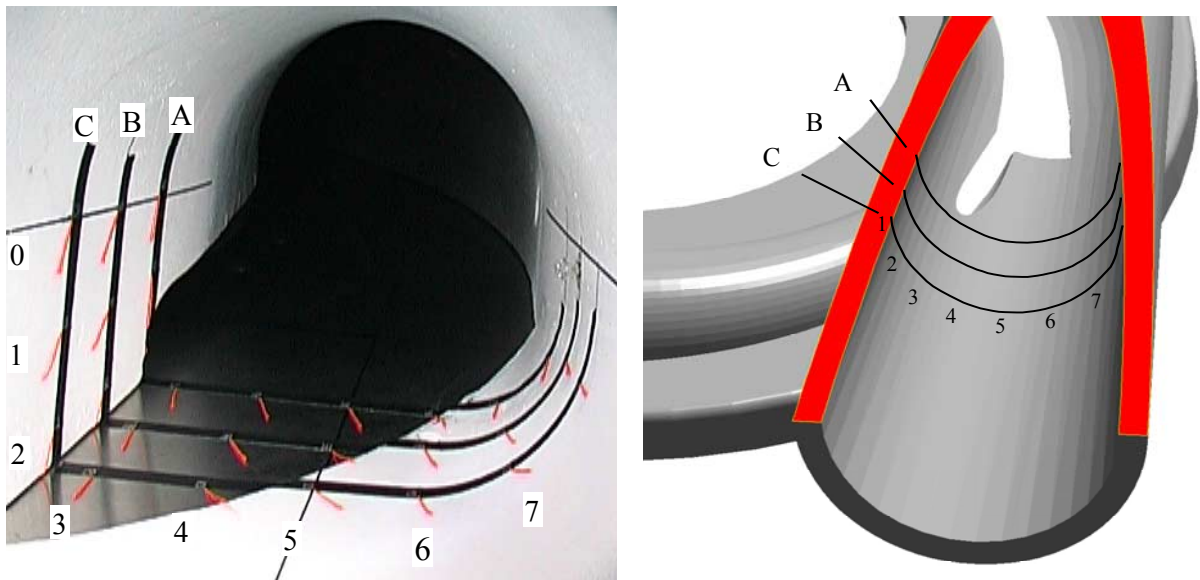


Figure 30. Location of the flow visualisation tufts in the original volute (left) and in the circular and modified circular volutes (right). Photo: Juha Haikola / LUT

4 EXPERIMENTAL RESULTS

4.1 Performance map of the compressor

The performance map of the compressor was measured with all the three different volutes. The volute and the exit cone were insulated with mineral wool in order to rule out the effect of different heat transfer properties of the stainless steel and aluminium volutes. The measurement was carried out at six different speeds: 0.68, 0.80, 0.90, 1.00, 1.08 and 1.13 times the design speed. The compressor was first allowed to warm up at the lowest speed near the choke line. The measurement was then begun at the highest flow at the lowest speed. The operation point was adjusted and the temperature was allowed to stabilise before the measurement was made. Then the compressor was throttled from the inlet and the next point at the same speed was measured. The whole constant speed curve was measured in this manner until the stall line was reached. Then the speed was increased and the next constant speed curve was measured starting again from the highest flow. In this manner the pressure ratio and the temperature were constantly increasing during the measurement. Although the temperature was allowed to stabilise at each point for a reasonably long time, a slight transient condition may still have existed during the measurement resulting in an overestimate of the measured isentropic efficiency by approximately 0.3 - 0.5 percentage points. As all the performance map measurements were carried out in the similar way, they are fully comparable.

The determination of the stall limit is not straightforward in a vacuum compressor, since stalling begins fairly smoothly especially at a low pressure ratio. As the flow is throttled, the pressure ratio increases until a maximum is reached. When the flow is further throttled, the pressure ratio begins to fall, but the operation of the compressor is still stable. After still further throttling small fluctuations in the pressure ratio and slight vibrations in the compressor are observed. The stall limit shown in the performance maps is located at this point. If the flow was further throttled, the compressor would enter into full surge. The determination of the right side of the performance map was more ambiguous. In general, the measurement of each constant speed curve was begun around the point where the compressor isentropic efficiency was 50%, since it makes little sense to operate the compressor at a higher flow. However, at higher speeds the maximum flow was limited by the power limitation of the

electric motor, so the 50% efficiency could not be reached. For these reasons clear aerodynamic choking (vertical operation curve) cannot be observed in the performance maps.

During the measurement the speed and mass flows of each point were scaled to the chosen reference conditions according to equations (5) and (6). When a vacuum compressor is being measured, the outlet pressure stays constant while the inlet pressure varies according to the pressure ratio. For this reason the reference temperature and humidity were given at the inlet, but the reference pressure $p_{15\ ref}$ at the outlet. The inlet pressure needed for equation (6) was calculated from the measured pressure ratio

$$p_{11\ ref} = p_{15\ ref} \frac{p_{11}}{p_{12}} \quad (25)$$

In all performance maps the mass flow and the rotational speed have been made non-dimensional by dividing them by the mass flow and the speed at the design point of the original configuration. Figure 31 shows the non-dimensional performance map of the original compressor using a mass flow -based x-axis. The shape of the map looks odd at first but is typical for a vacuum compressor. As the pressure ratio increases, the inlet pressure decreases, because the outlet pressure is kept constant in the vacuum application. This results in decrease of the density which shifts the points at the upper part of the map towards lower mass flow.

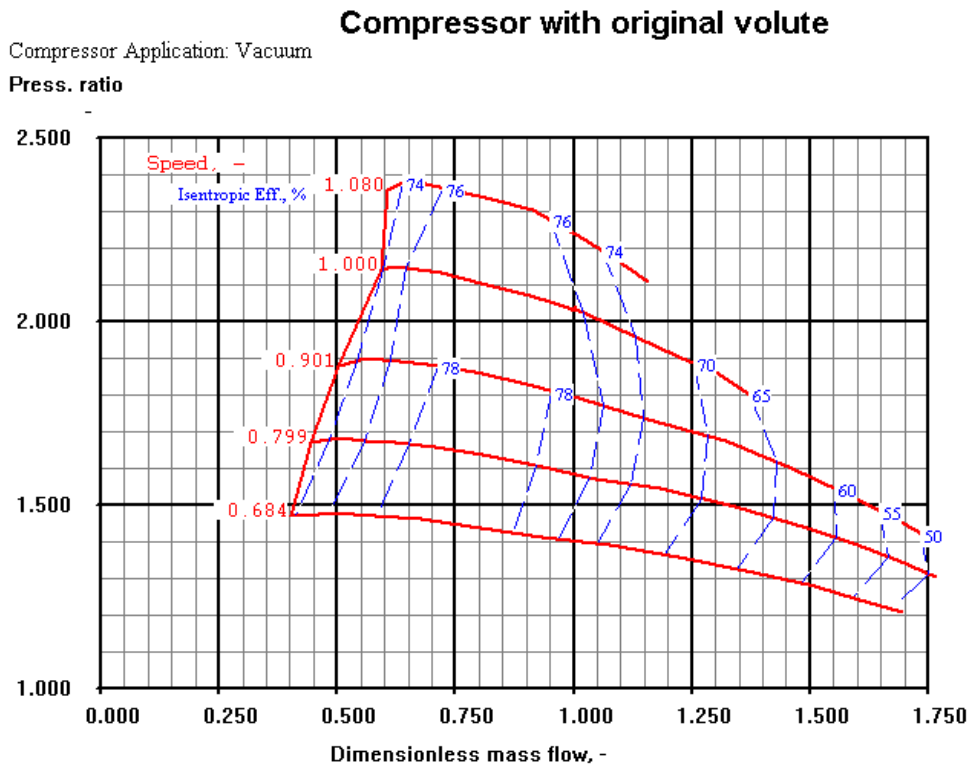


Figure 31. Performance map of the compressor with the original volute. Non-dimensional mass flow on the horizontal axis.

Figure 32 shows the same performance map as figure 31, but with a volume flow -based x-axis. The volume flow at the reference conditions is calculated using equation (7), so only the inlet temperature and gas composition are needed. The volume flow has been non-dimensionalized by dividing it by the volume flow at the design point. The map in figure 32 looks like a conventional compressor map, because the varying inlet pressure does not affect the scaling.

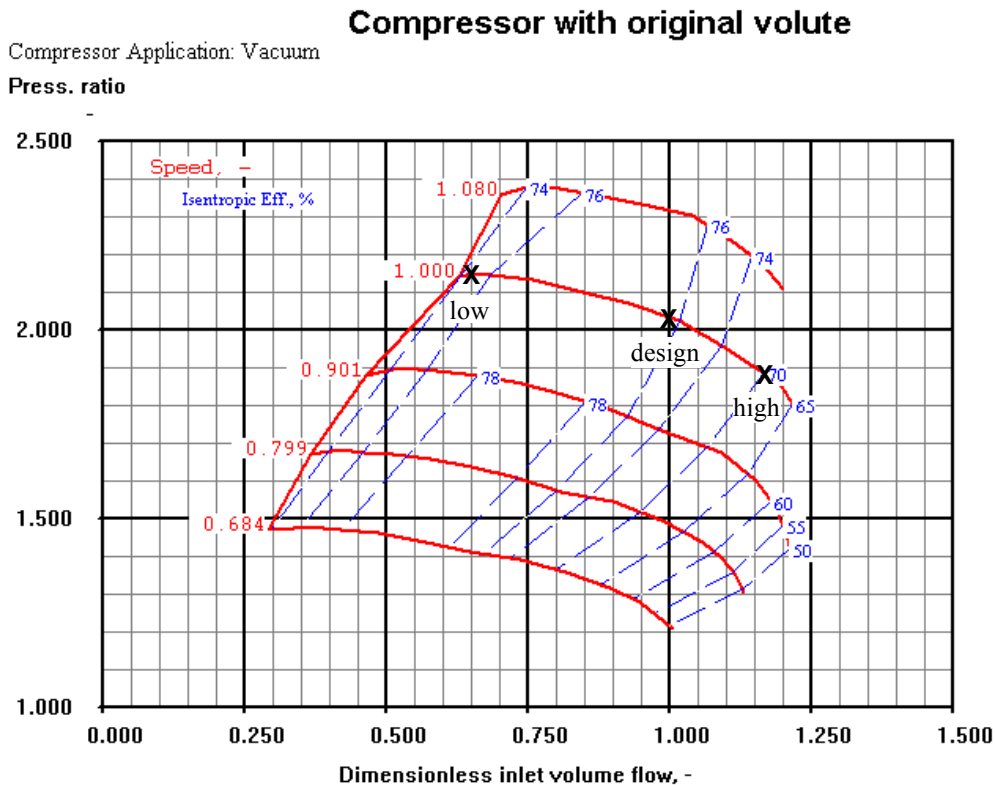


Figure 32. Performance map of the compressor with the original volute. Non-dimensional volume flow on the horizontal axis.

During the measurements the operating point of the compressor was always set using the reference speed, equation (6), and reference volume flow, equation (7). The compressor produces slightly different pressure ratio with the different volutes, so the mass flow -based scaling would lead to erroneous reference mass flow, when the reference pressure is given at the outlet. For this reason all of the results in this work are presented using the reference volume flow.

Three operating points at the design speed were selected for detailed analysis. The points at 0.65, 1.00 and 1.17 times the design flow, denoted with low, design, and high are also indicated in figure 32. The volume flow -based non-dimensional performance map of the

compressor with the circular volute is shown in figure 33 and that with the modified circular volute in figure 34.

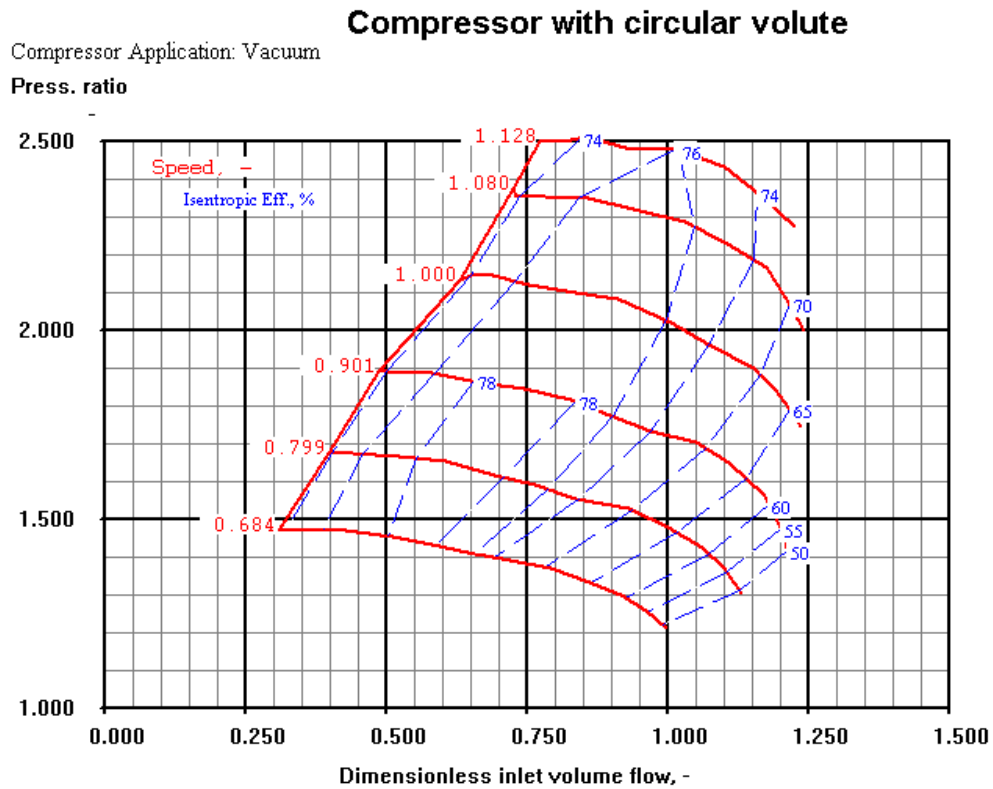


Figure 33. Performance map of the compressor with the circular volute.

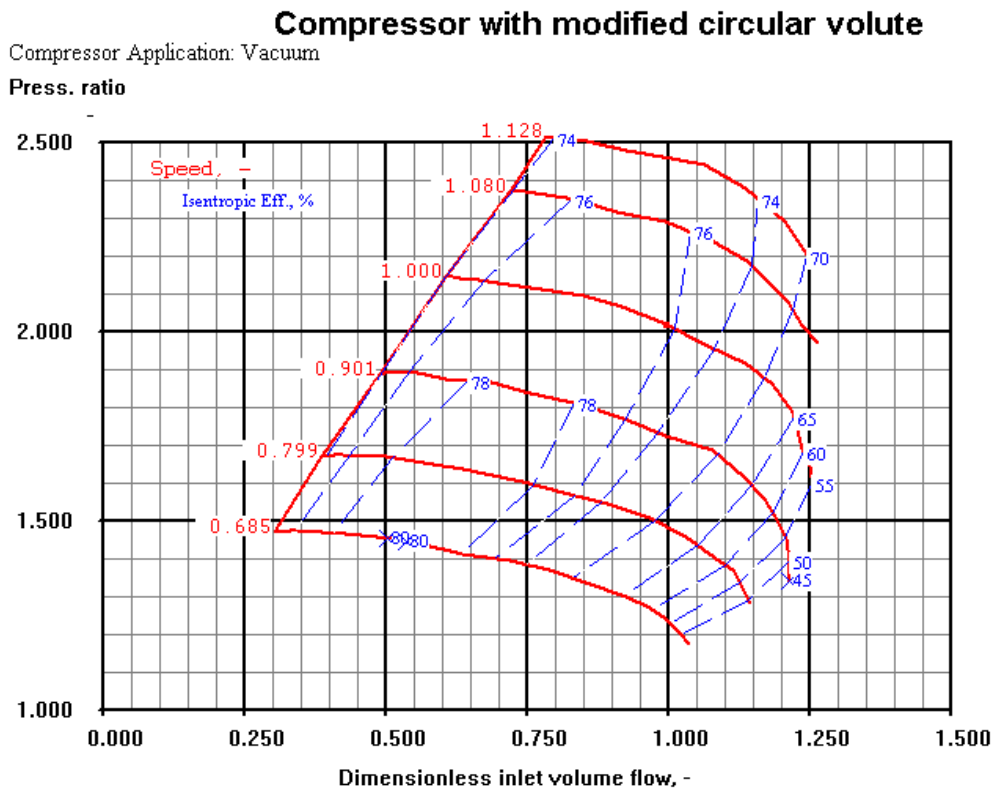


Figure 34. Performance map of the compressor with the modified circular volute.

Fairly small differences are seen when the performance maps measured with the different volutes are compared. Only minor changes in the stall limit are observed, but taking into account the uncertainty in the determination of the stall limit, no differences between the volutes can be determined. The choke limit remains unchanged as much as from the end of the 0.9 speed curve can be seen. Also the pressure ratio as a function of the rotational speed is practically the same. The reason for the small differences is clear. The area of the cross-section of the different volutes was the same, so the stall and choke lines as well as the shape of the constant speed curves should be the same.

In the efficiency curves, however, some differences can be found. The modified circular volute seems to have higher efficiency especially at the low speeds and high flows. For example at the operating point $q_v/q_{v, des} = 1.00$ and $\pi = 1.50$ the isentropic efficiency of the compressor is two percentage points higher with the modified circular volute than with the other volutes. The reasons for this are discussed in the following chapter.

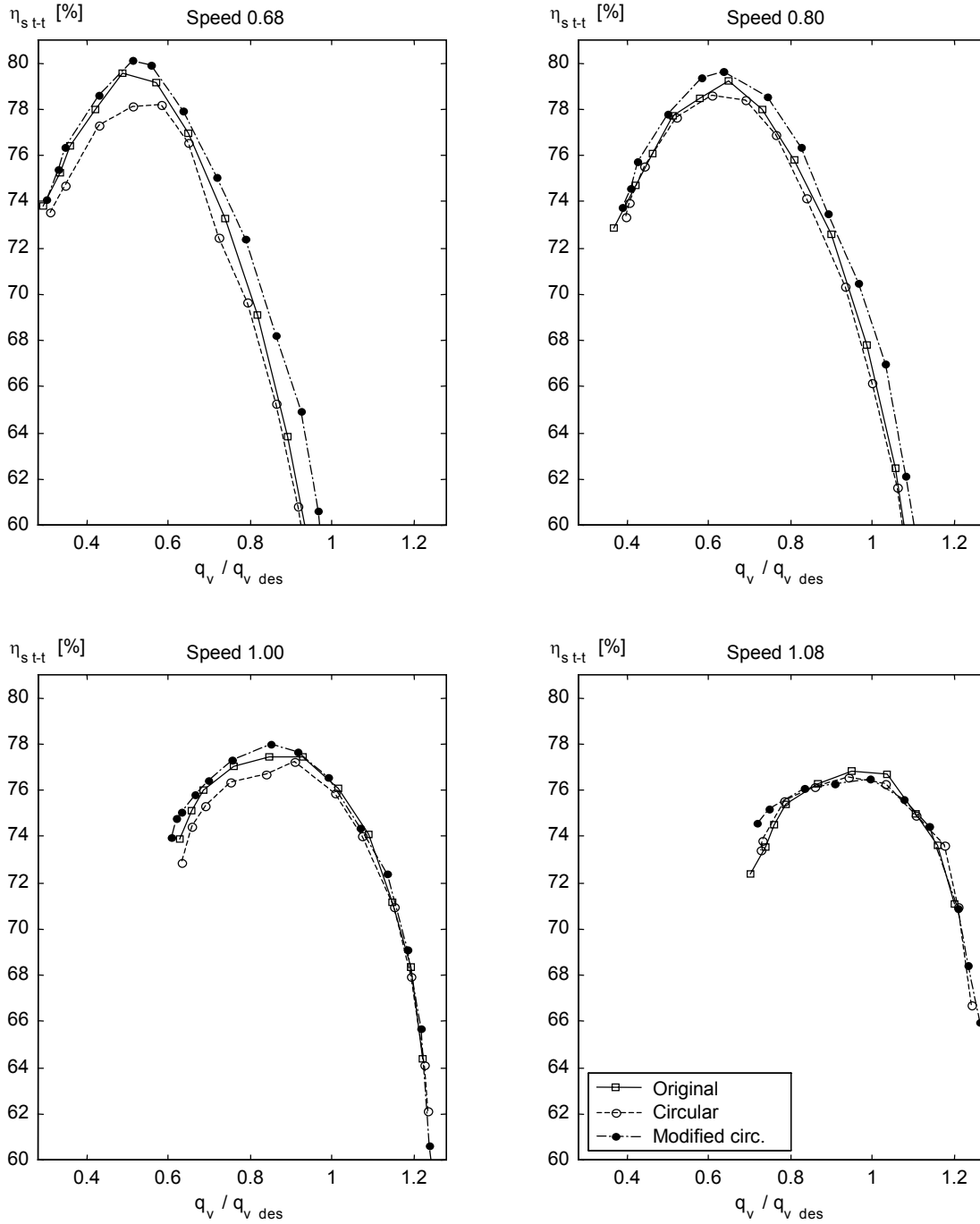
4.2 Efficiency of the compressor

The total-to-total isentropic efficiency of the compressor was measured in the whole operating regime during the performance map measurement as described above. Figure 35 shows the total-to-total isentropic efficiencies obtained during the performance map measurement with different volutes.

The efficiency was also measured in the three selected operating points at the design speed by letting the compressor to run for 1 - 1½ hours at each point. This ensured that the steady state conditions were achieved and allowed numerous measurements at each point to be made. The efficiencies shown in table 1 are the mean values of those measurements.

Table 1. Isentropic total-to-total efficiency of the compressor with the different volutes at the design speed.

	Low flow	Design flow	High flow
Volute	$\eta_{s\ t-t}$ [%]	$\eta_{s\ t-t}$ [%]	$\eta_{s\ t-t}$ [%]
Original	73.9	76.0	69.1
Circular	74.2	76.0	68.8
Modified circular	75.1	75.9	69.6

**Figure 35.** Isentropic total-to-total efficiency of the compressor with the different volutes at different speeds.

The uncertainty of the efficiency measurement is about ± 1.2 percentage points in a single measurement (Sallinen 1999). The differences in the measured efficiency with the different volutes are bigger than the uncertainty only in the lower right quadrant of the performance map. Thus the performance comparison has to be treated with some caution. However, in the detailed efficiency measurements 50 - 100 single measurements were made at each point and the average value was calculated. Also the repeatability of a measurement is better than its absolute accuracy, and in this case all of the measurements were made on the same test stand using the same instrumentation. Thus at least some kind of comparison between the measurements is justified even if the differences are below the absolute uncertainty.

According to table 1 practically no differences between the volutes exist in the design point. This is also seen in figure 35. It is apparent that at the design point the incidence angle of the flow to the tongue of the volute is approximately zero. Thus the tongue does not disturb the flow very much regardless of its shape.

At high flow the modified circular volute performs best and the circular worst, see table 1. The same tendency is observed in figure 35 and is the strongest at 0.68 and 0.80 speeds. In these operating points the flow at the volute inlet is the most radial. Thus the swirling component inside the volute channel is strong in comparison to the through flow velocity, and the incidence angle at the tongue of the volute has a large positive value. The good performance of the modified circular volute is explained by the circular shape, which is the most optimal for the swirling flow, and the rounded and slightly shortened tongue, which tolerates large incidence variations with small losses. The performance of the original volute suffers from the rectangular corner, which causes an additional corner vortex (Reunanen et al. 2000), and also from the possible flow separation in the exit cone (see chapters 4.3 and 4.4). The poor performance of the circular volute at high flow results from the sharp-edged tongue and rough surface, which produce more loss than the circular shape of the cross-section is able to reduce in comparison to the original volute.

At low flow the modified circular volute performs best and the original worst according to table 1. According to figure 35 the modified circular volute is again the best, but the circular volute seems to be the worst at most speeds. The discrepancy is explained by the measurement accuracy, since the 0.3-percentage-point-difference between the original and circular volutes (table 1) is within the measurement uncertainty. The good performance of the modified

circular volute at low flow is most likely due to the rounded tongue, which tolerates large incidence variations. The exit cones of the circular and modified circular volute seem to have a tendency to flow separation at low flows (see chapters 4.3 and 4.4), which together with the sharp tongue is the most likely cause for the somewhat lower performance of the circular volute.

4.3 Static pressure distribution in the diffuser, volute and exit cone

The static pressure distribution at the impeller exit i.e. diffuser inlet was measured using eight static pressure taps mounted on the diffuser shroud wall. The measured pressures have been made non-dimensional by dividing them by the total pressure at the compressor inlet. Figure 36 shows the pressure distribution at various volume flows at the design speed and figure 37 at the 0.8 speed. Only the pressures measured using the original volute are shown, since the differences in the pressure distribution with the different volutes are small and could hardly be visible with the current scaling of the axes.

The pressure non-uniformity caused by the volute is clearly visible at the diffuser inlet. At high flow the static pressure drops along the circumference. The pressure is almost constant at the design flow at the design speed. However, a small decrease is observed indicating that the design flow of the volute is slightly lower than the design flow of the impeller. At 0.8 speed the pressure distribution is naturally constant at the lower flow of about 0.65. At low flow the static pressure rises along the circumference on the average, but the rise is characterised by two distinct waves. The waves are strong at the design speed and become weaker at 0.8 speed, yet being still clearly visible. The most likely reason for this two-wave pattern is the impeller response to the non-uniform static pressure distribution caused by the volute. This kind of behaviour has also been reported by Young (1992) and Hagelstein et al. (1997), but has not been observed by some other researchers such as Ayder (1993). Also Fatsis et al. (1997) have calculated a bimodal behaviour of the main flow variables at the impeller outlet. They explain this to be a result of a static pressure wave travelling back and forth in the impeller blade passage. According to Young (1992) and the present measurements the waves become weaker as the speed and pressure ratio gets smaller. The experiments by Ayder (1993) were carried out at the pressure ratio 1.1 - 1.3, which could explain the two-wave pattern not being present in those experiments.

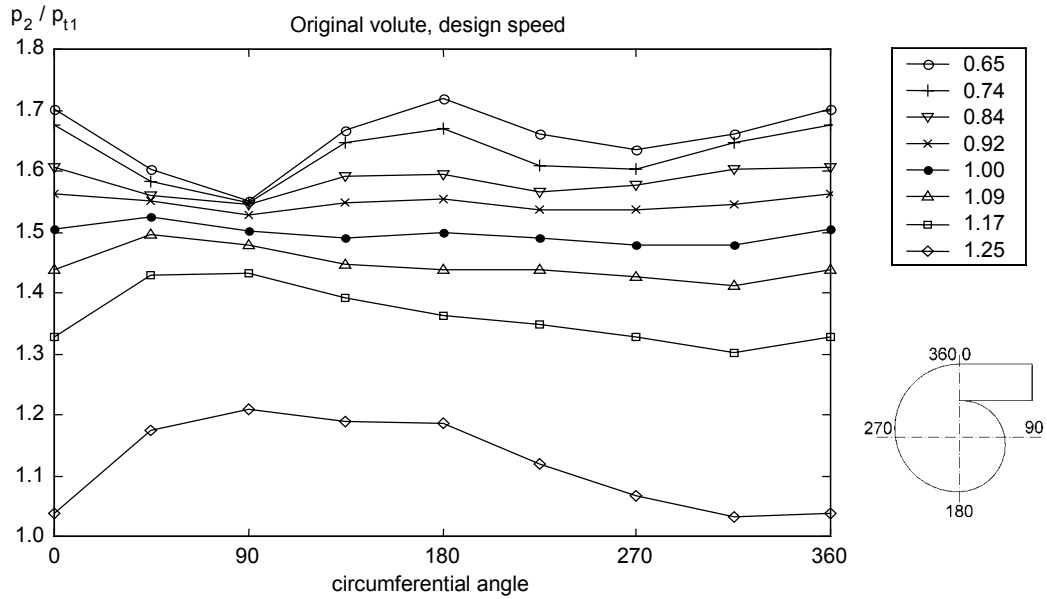


Figure 36. Static pressure distribution at the diffuser inlet at radius ratio $r/r_2 = 1.01$ at the design speed with the original volute.

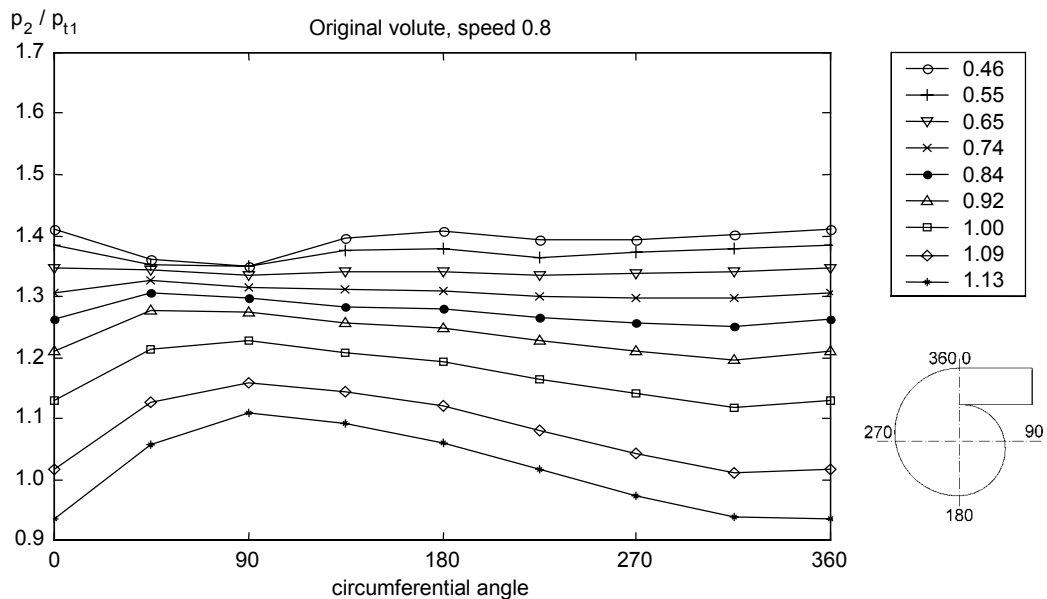


Figure 37. Static pressure distribution at the diffuser inlet at radius ratio $r/r_2 = 1.01$ at 0.8 speed with the original volute.

In an earlier time-accurate simulation of the compressor at the design flow (Pitkänen et al. 1999) a two-wave pattern was observed in the mass flow of a single blade passage as it rotated one revolution. The reason for this two wave-pattern could not then be explained and it was thought to be erroneous. For example some kind of resonance due to a relatively small calculation domain was suspected to be one possible cause. The present measurements prove that there exists a two-wave pattern in the pressure distribution at low flow. There is good

reason to believe that this pressure distribution would cause the mass flow to oscillate in a similar manner. Thus the reason for the two-wave oscillation in the previous time-accurate calculation could be that the calculation over-predicted the oscillation and it was present already at the design flow.

Figure 38 shows the differences in the static pressure distributions at the diffuser inlet with the different volutes. The results are shown at low, design and high flow for the design speed and at 0.46, 0.74 and 1.09 times the design flow for the 0.8 speed. The measured static pressures are again divided by the total pressure at the compressor inlet and the scaling of the axes is chosen so that the differences are seen. Although the offset of the pressure is different, the range of the y -axis in the different figures is the same to enable easy comparison.

The first conclusion from figure 38 is that the differences between the volutes are small. This is natural, since the circumferential distribution of the area of the cross-section was designed to be the same with the different volutes. It is seen in figure 38 that the static pressure at the impeller exit is the highest with the original and the lowest with the modified circular volute. Also the two-wave pattern at low flow seems to be slightly stronger with the original volute than with the circular volutes. The exact reason for the differences is uncertain, but the small difference in the radius ratio of the vaneless diffuser (1.90 for the original and 2.03 for the both circular volutes) could be one explaining factor.

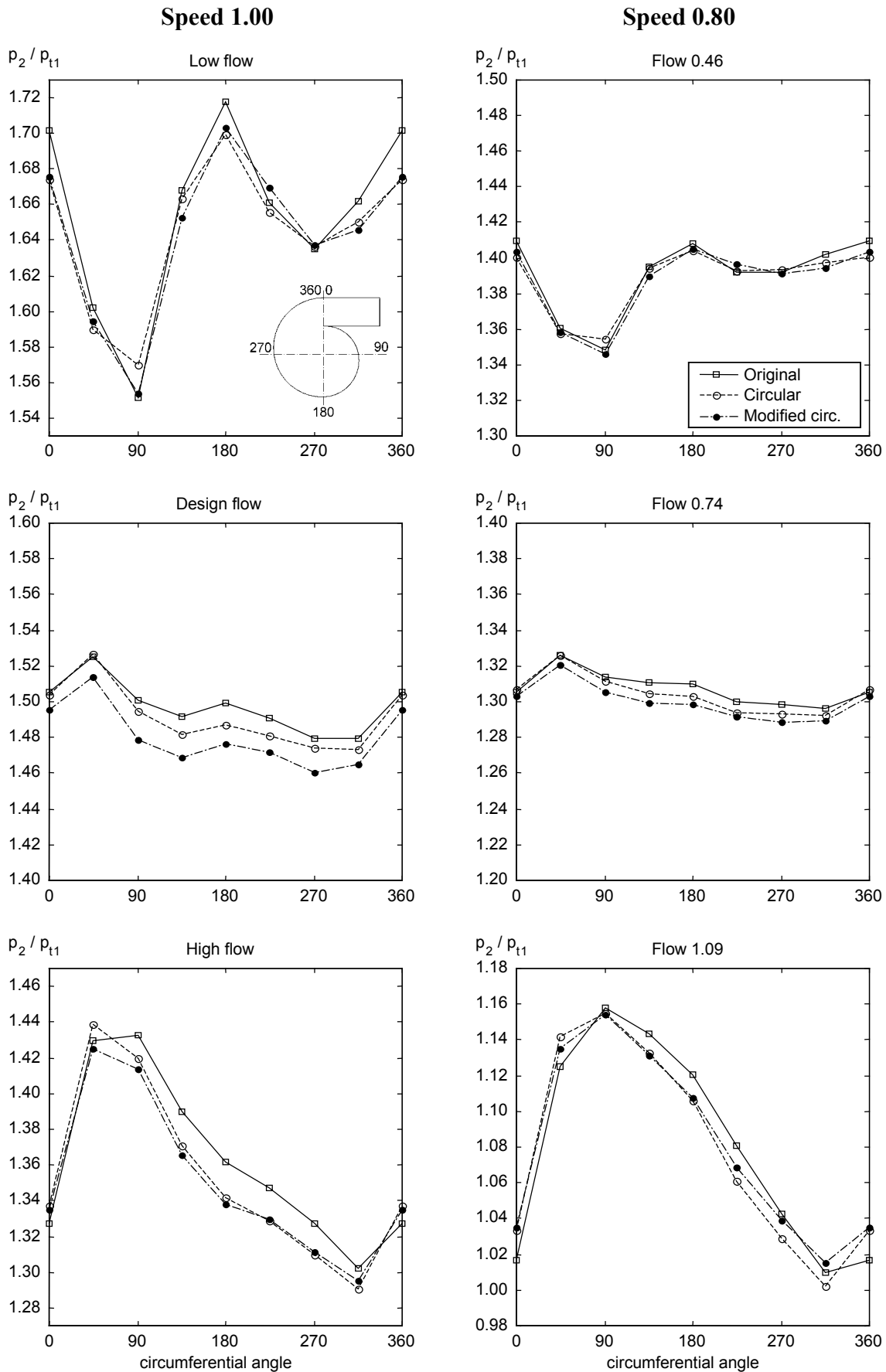


Figure 38. Static pressure distribution at the diffuser inlet at radius ratio $r/r_2 = 1.01$ at low, design and high flow at speed 1.00 (left) and at 0.46, 0.74 and 1.09 flow at speed 0.8 (right) with the different volutes.

The static pressure distribution on the volute and exit cone surfaces was measured using seven static pressure taps positioned on the volute and exit cone top walls. The pressure distribution in the original volute at various volume flows at the design speed is seen in figure 39. The corresponding distribution at 0.8 speed is shown in figure 40. The measured pressures are again non-dimensionalized by the total pressure at the compressor inlet. Here the length of the exit cone is transformed to angles in order to allow the data of the volute and exit cone to be drawn in the same figure. The length of the exit cone in angles is the angle of an arc, whose length at the radius of the volute centre at $\theta = 360^\circ$ is equal to the length of the exit cone.

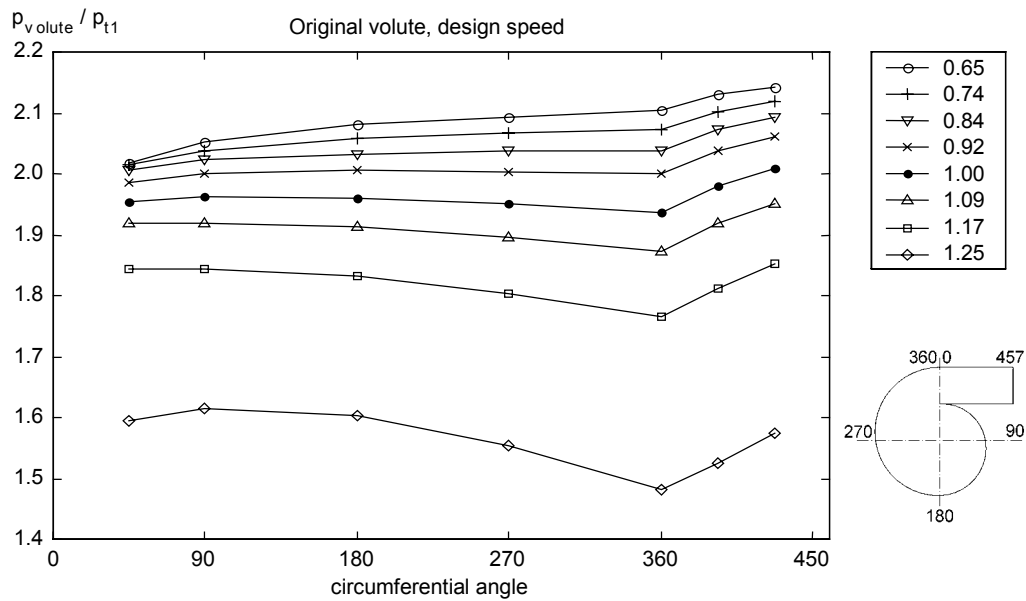


Figure 39. Static pressure distribution in the original volute and the exit cone at the design speed.

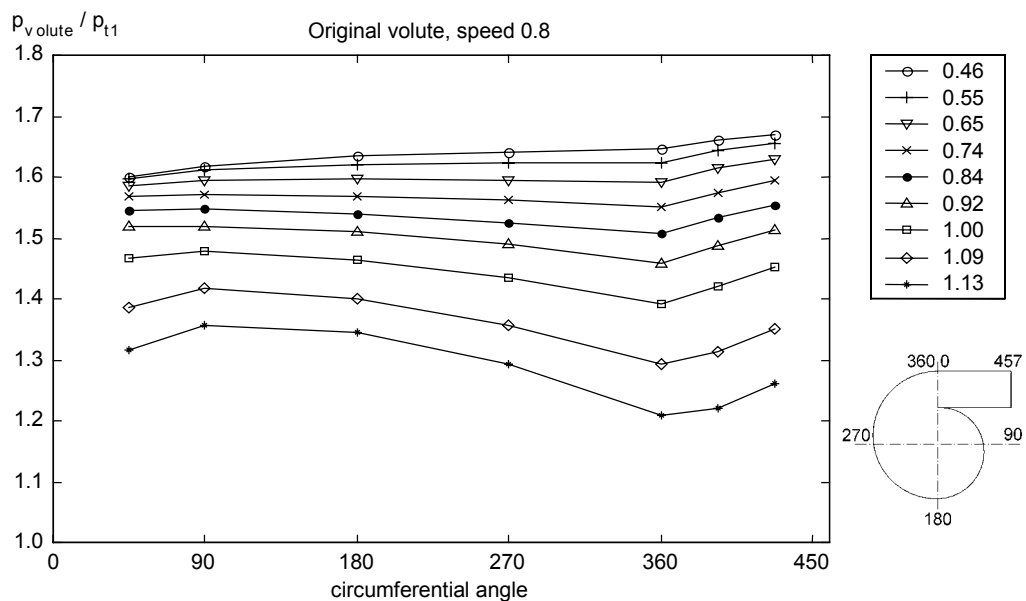


Figure 40. Static pressure distribution in the original volute and the exit cone at 0.8 speed.

A typical pressure distribution of the volute is observed. At high flow the static pressure drops along the circumference, at the design flow the distribution is fairly constant and at low flow the pressure increases. Only one wave per 360° is present in the volute even at low flow. Thus the two-wave behaviour at the diffuser inlet is not caused by the volute pressure distribution alone, but is a result of the pressure non-uniformity caused by the volute and the impeller response to that.

In the exit cone a desired static pressure rise is observed. At high flow, however, a small fall in the rising trend at 392° position is present, especially at 0.8 speed. This indicates that the exit cone is no longer working as an efficient diffuser.

A detailed view of the pressure distribution in the different volutes is shown in figure 41. The same flows, speeds and axis scaling criteria as in the pressure distribution analysis of the diffuser are used. Again the differences between the volutes are small due to the equal area of the cross-section of the different volutes. At low flow the static pressure rise in the end of the exit cone at 425° drops in the circular and modified circular volutes. This indicates flow separation in that part of the exit cone. At the design flow the pressure in each volute drops slightly in the circumferential direction confirming that the design flow of the volutes is a little too small. At high flow at 0.8 speed the already mentioned drop in the performance of the exit cone of the original volute at 392° is seen. At all flows the pressure in the 360° position drops most in the circular and second most in the modified circular volute.

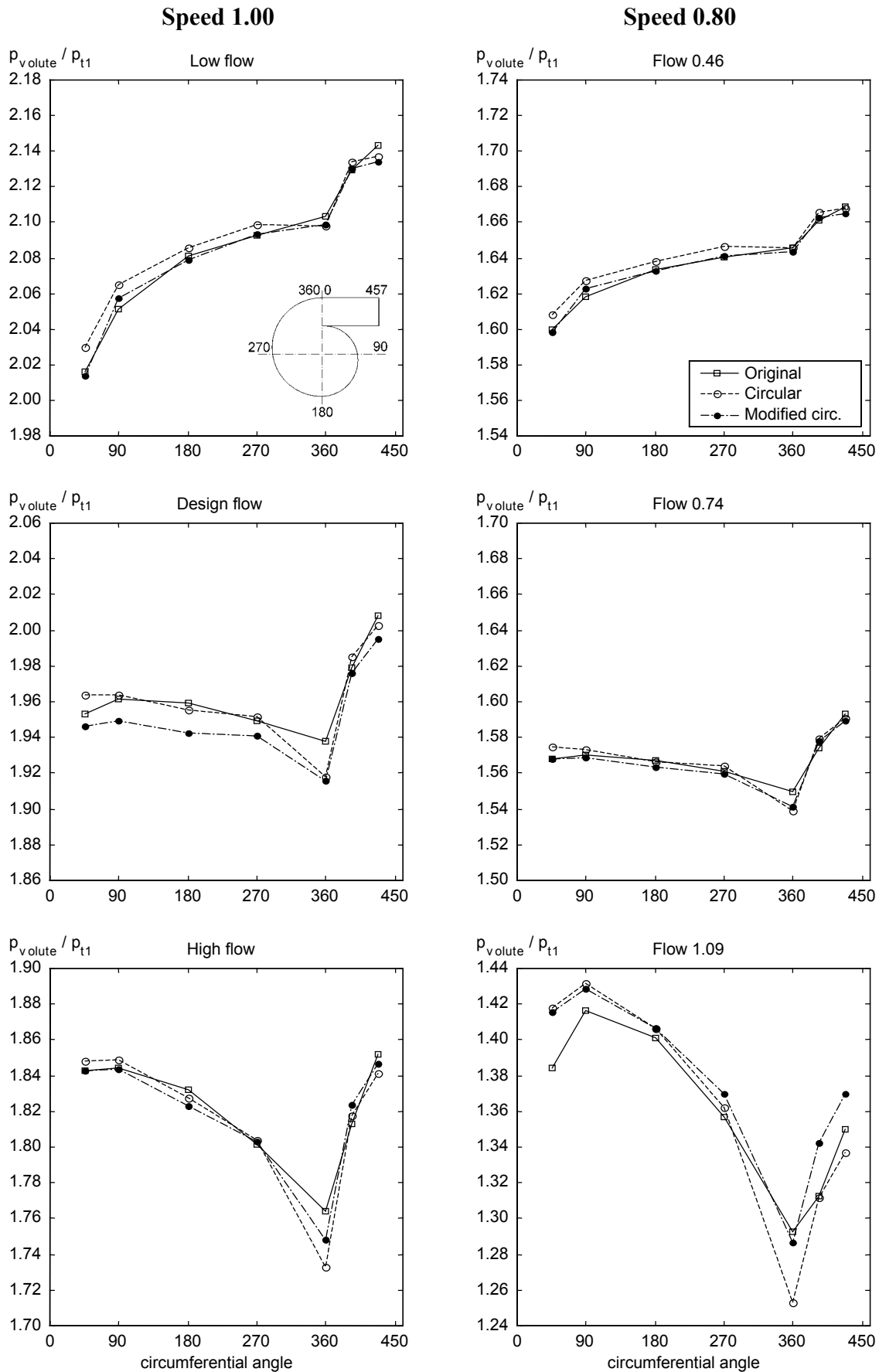


Figure 41. Static pressure distribution in the different volutes and exit cones at low, design and high flow at speed 1.00 (left) and at 0.46, 0.74 and 1.09 flow at speed 0.8 (right).

4.4 Results of the Cobra-probe measurements at the volute inlet

A three-hole Cobra-probe was traversed across the diffuser in three different circumferential locations at the diffuser outlet in order to obtain information of the flow entering the volute. The probe allowed the measurement of the static pressure, total pressure and flow angle. The temperature was not measured, and thus the local flow velocity cannot be calculated accurately. The results of the flow traverses are shown in figures 42, 43 and 44 for the original, circular and modified circular volutes, respectively. All pressures are non-dimensionalized by the total pressure at the compressor inlet and the flow angle is measured from the radial direction.

The static pressure distribution across the diffuser is almost constant with each volute at all positions and flows. Only a very slight decrease close the shroud is observed especially at high flow. The total pressure distribution is typical for the vaneless diffuser. The total pressure is high in the middle and decreases towards the walls due to the boundary layer. Also the flow angle distribution is typical. The flow is more radial in the middle and turns more into the tangential direction near the hub and shroud.

A direct comparison between the volutes is difficult since the traverses were made at slightly different circumferential positions. One point can be made, however. At low flow the total pressure profile at the 180° position with the original volute and at the 168° position with the circular and modified circular volutes is considerable flatter than the corresponding profiles at different locations. Also the level of the total pressure in these measurements is low. This phenomenon is more pronounced with the original volute than with the circular or modified circular volutes.

The pressure and angle distributions in each circumferential location were averaged spanwise across the diffuser using mass flow -based weighting. This enables the circumferential distribution of the quantities to be examined, see figure 45. Of course, an accurate circumferential distribution can not be presented using only three points, but the results have been collected to figure 45 in order to present all the information that is obtainable from the current measurements.

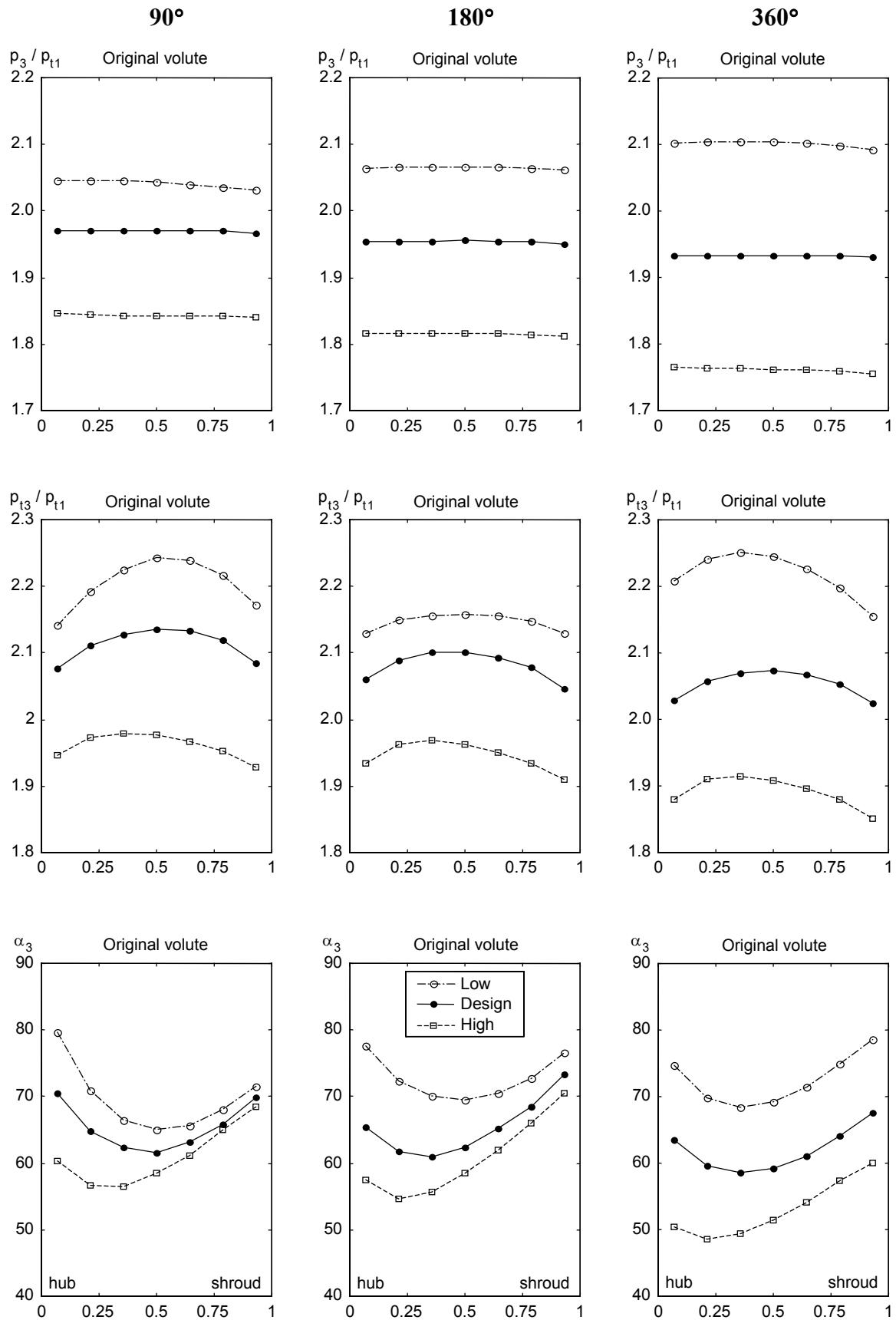


Figure 42. The static pressure, total pressure and flow angle distributions at the volute inlet in three different circumferential positions with the original volute.

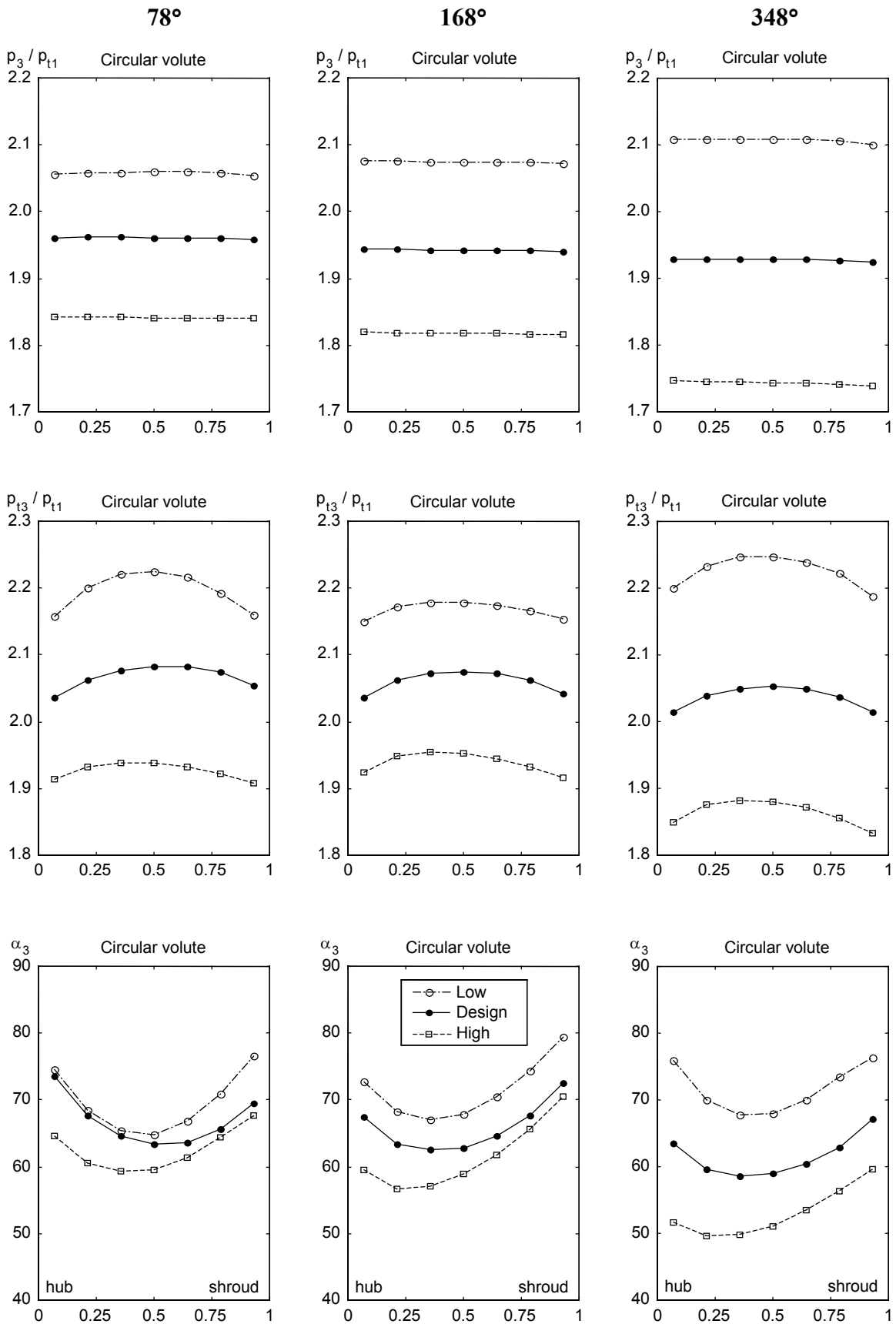


Figure 43. The static pressure, total pressure and flow angle distributions at the volute inlet in three different circumferential positions with the circular volute.

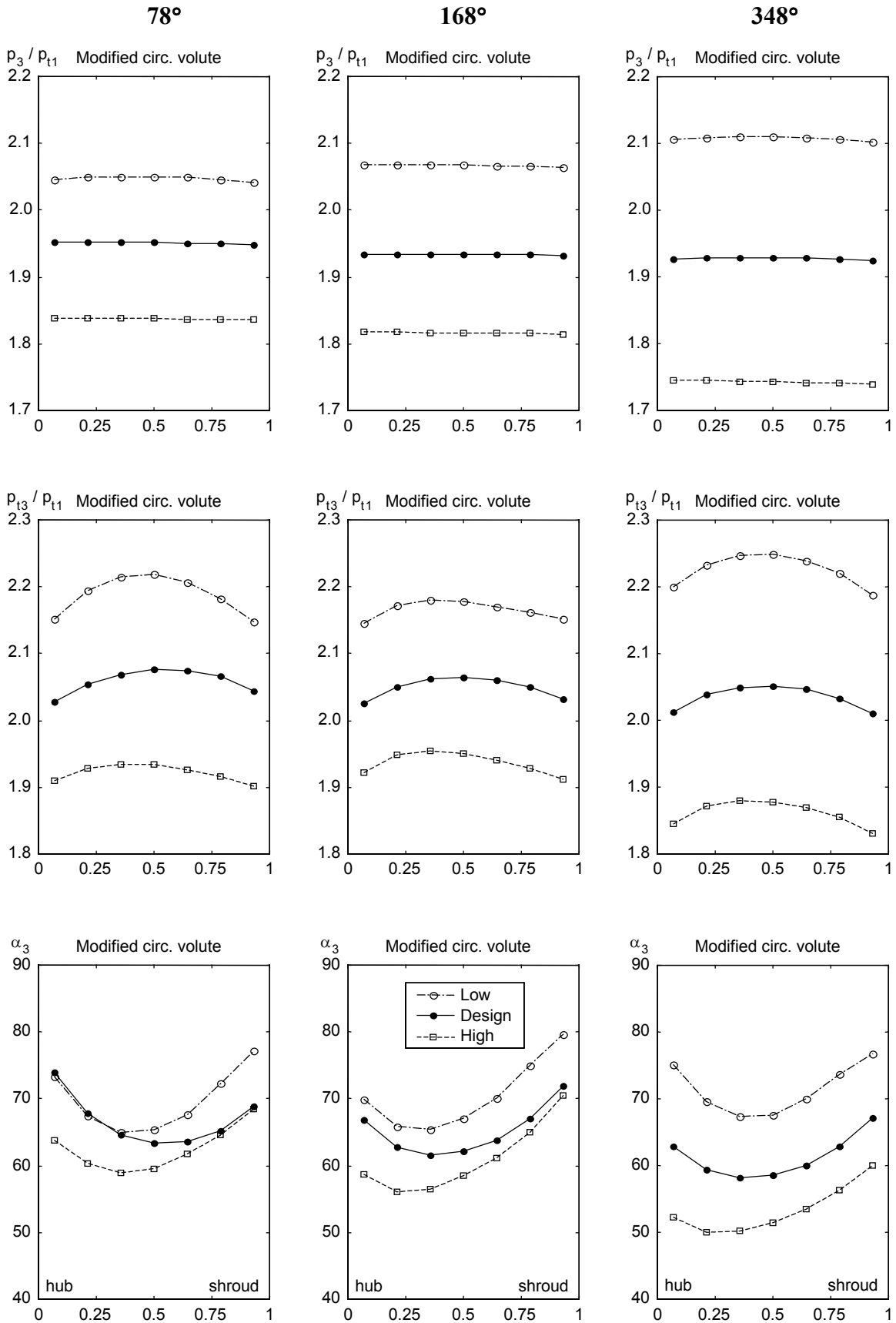


Figure 44. The static pressure, total pressure and flow angle distributions at the volute inlet in three different circumferential positions with the modified circular volute.

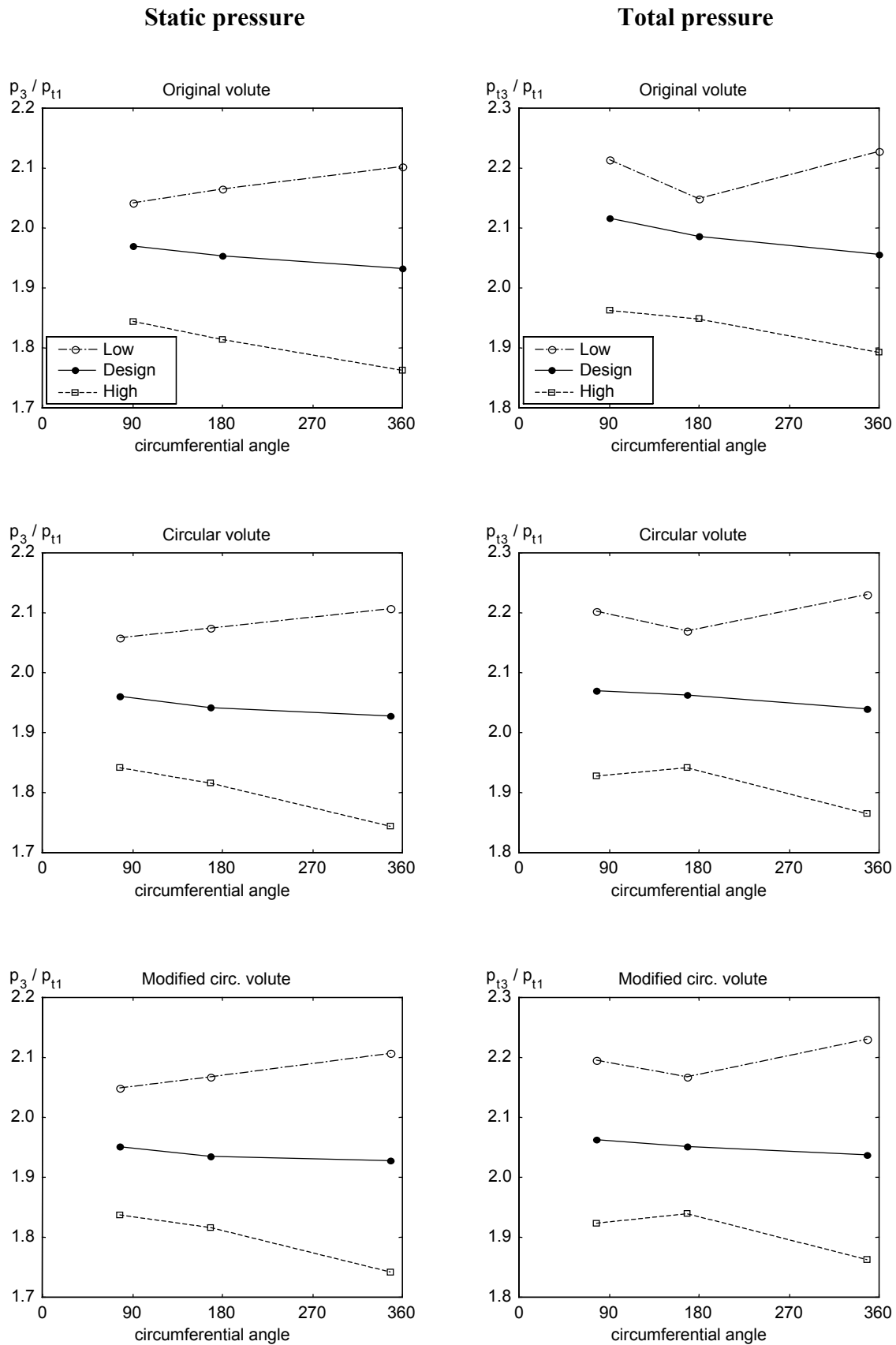


Figure 45. Circumferential distribution of the spanwise averaged static pressure and total pressure at the volute inlet with the different volutes.

Clear and expected trends are seen in the static pressure distribution in circumferential direction in figure 45. At low flow the static pressure increases, at the design flow it decreases slightly and at high flow it decreases more strongly. Thus the static pressure distribution at the volute inlet follows well the static pressure distribution measured from the volute top. When the different volutes are compared, hardly any differences can be seen.

The total pressure distribution, see figure 45, is more complicated. At low flow the total pressure is considerably low around the 180° location. This is a direct result from the relatively flat and low total pressure profile in that measurement point. The notch in the circumferential total pressure distribution is clearly stronger with the original volute than with the circular or modified circular volutes. Since only three measurement points in the circumferential direction were available, the extent of the low total pressure zone cannot be determined. At the design flow a slight and fairly constantly decreasing trend is observed. At high flow a decreasing trend is also seen, but a small bend to the opposite direction from that of low flow is seen.

Hagelstein et al. (2000) have measured the total pressure distribution at the vaneless diffuser outlet in six circumferential locations, see figure 46. They report an exactly similar notch in the total pressure distribution at low flow around the 120° location. Hagelstein et al. explain the notch to be the result of the impeller response to the static pressure perturbation caused by the tongue of the volute. The formation mechanism of the local low pressure is demonstrated in figure 47. The low static pressure in the beginning of the volute (at the 40° - 90° location) is transmitted directly across the diffuser and causes a low static pressure at the impeller exit at the same circumferential position. This is shown also by the present measurements, see figure 36. Due to the low static pressure, the impeller produces a low total pressure in this circumferential location. This low total pressure fluid then flows through the diffuser along the logarithmic streamline and hits the diffuser outlet around the 180° position. In the experiments of Hagelstein et al. the tongue was located at $\theta = 0^\circ$ and the radius ratio of the diffuser was only 1.4, so the low total pressure wake was observed already at $\theta = 120^\circ$.

The phenomenon is weaker with the circular and modified circular volute, because the radius ratio of the diffuser is slightly greater and the traversing point of the Cobra-probe is at a 12° smaller angle with the circular and modified circular volute than with the original volute, see figure 47. Thus the low total pressure zone hits the Cobra-probe directly when the original

volute is used, but partially misses the probe when the circular or modified circular volute is used.

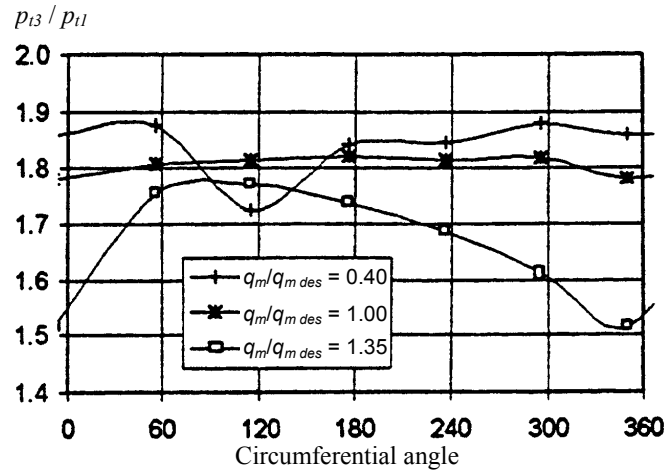


Figure 46. Circumferential distribution of spanwise averaged total pressure at the diffuser outlet measured by Hagelstein et al. (2000)

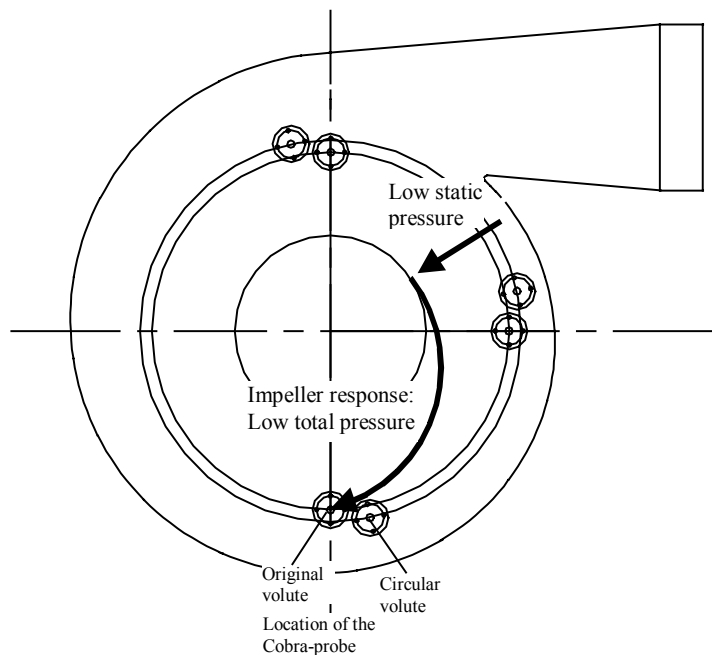


Figure 47. Formation mechanism of the local low total pressure at the diffuser outlet of the test compressor at $\theta = 180^\circ$ at low volume flow.

4.5 Overall performance of the volute and exit cone

The overall performance of the volute and exit cone combination (states 3→5) was analysed using the total pressure loss and static pressure recovery coefficients defined by equations (8)

and (9). The static and total pressures p_5 and p_{t5} after the exit cone were obtained from the compressor test stand instrumentation. There is a 1500 mm long smooth pipe between the exit cone and the pressure measurement position, which provides some room for the highly swirling flow to stabilise before the measurement is made. The pressure loss in this pipe calculated according to the pipe flow pressure loss equation and Moody's chart (Schlichting 1979) is 20 Pa, 50 Pa and 80 Pa for the low, design and high flows respectively, so it can be considered negligible.

The static and total pressures p_3 and p_{t3} at the volute inlet were obtained from the Cobra-probe measurements. The measured pressures were first averaged spanwise in each traversing position using mass flow weighting. The average pressures were then averaged circumferentially using mass flow weighting in order to get only one value for the pressures p_3 and p_{t3} . The validity of the circumferential averaging can be questioned, since the measurements were made only in three different circumferential locations and the measurement at the $168^\circ/180^\circ$ location includes uncertainties discussed above. It is certain that an exact value for the pressures p_3 and p_{t3} cannot be calculated on the basis of the measurements. However, some kind of averaging was unavoidable so that the overall performance of the volutes could be calculated and their performance be compared. Thus two different circumferential averagings were made. In method 1 all three points were included with the point at $90^\circ/78^\circ$ being responsible for 25% of the flow area and the points at $180^\circ/168^\circ$ and $360^\circ/348^\circ$ being responsible for the rest (i.e. 37.5% each). The averaging method 2 was similar apart from the low flow, where the point at $180^\circ/168^\circ$ was left out due to the local notch in the total pressure. In that case the remaining two points were both responsible for 50% of the flow area. Method 2 can be justified on the basis of the measurements by Hagelstein et al. (2000). They report the notch in the total pressure to be rather local and to occur at low flow only. Apart from the notch at the low flow the pressure distributions are reported to be rather linear.

Figure 48 shows the total pressure loss coefficient and figure 49 the static pressure recovery coefficient of the different volutes and exit cones as a function of the volume flow using the averaging method 1 (left) and the averaging method 2 (right). It is seen that the total pressure loss of the volute and exit cone combination is at minimum at the design flow. At high flow rate the flow enters the volute more radially resulting in strong swirl and high losses inside the volute (Ayder 1993). This is observed as increased K_p in figure 48. At low flow rate the flow

enters the volute more tangentially, which, according to Ayder (1993), should result in low losses. However, the K_p in figure 48 increases towards low flow. This can be explained by the increased losses in the exit cone. At low flow the swirl inside the volute is weak, and thus cannot stabilise the diffusion in the exit cone as well as at higher flows. It is also possible that the separation begins already in the volute channel.

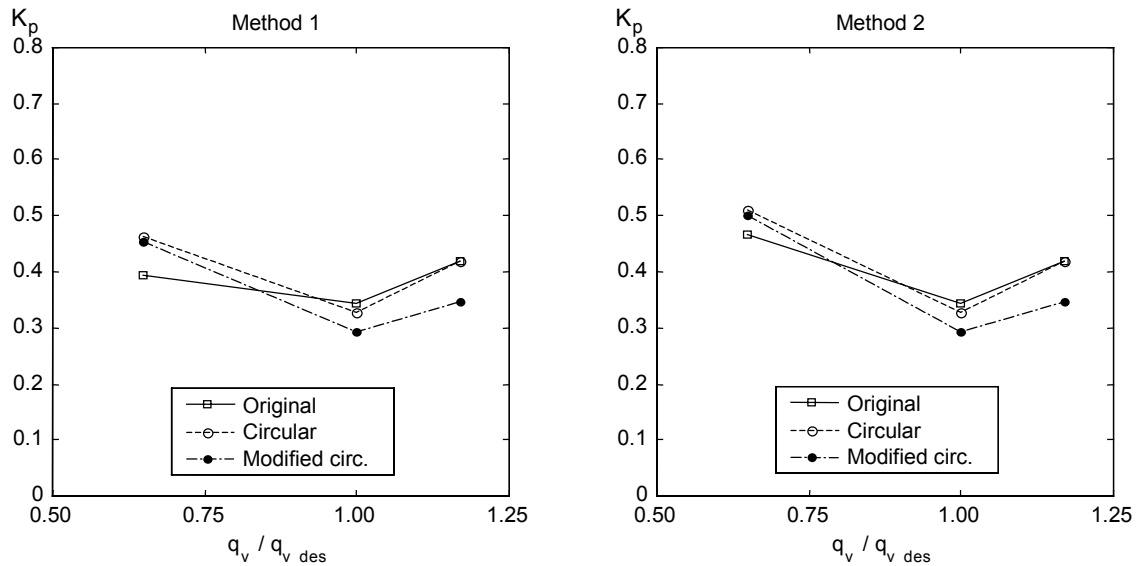


Figure 48. Total pressure loss coefficient of the different volutes and exit cones as a function of volume flow using averaging method 1 (left) and averaging method 2 (right).

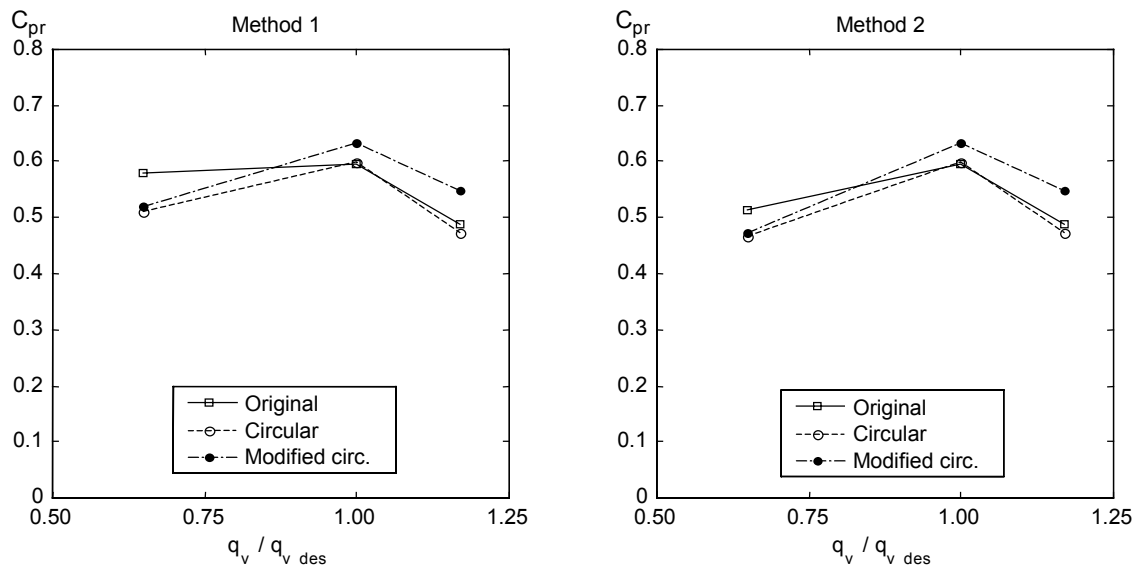


Figure 49. Static pressure recovery coefficient of the different volutes and exit cones as a function of volume flow using averaging method 1 (left) and averaging method 2 (right).

The differences between the volutes are seen in figure 48. At high flow the modified circular volute has lower losses than the other volutes - a trend which was observed also in the efficiency measurements. It is evident that the modified circular volute tolerates the radial flow better than the other volutes due to the circular cross-section and the rounded tongue. At the design flow, too, the modified circular volute has lower total pressure loss than the other volutes according to figure 48. This was not brought out by the efficiency measurements. The reasons for the discrepancy could be inaccuracies in the circumferential averaging, uncertainties in the efficiency measurements and the possibility that the small decrease in the volute loss is compensated for example by a small increase in the diffuser loss. At low flow the differences between the averaging methods 1 and 2 become clear. When the measurement point at 180°/160° is left out, the measured loss at low flow increases. Also the differences between the volutes become smaller. Nevertheless the original volute has the lowest total pressure loss at low flow according to figure 48. This is contradictory to the efficiency measurement, which showed the compressor efficiency to be the highest with the modified circular volute. The reasons for the discrepancy could be the same as at the design flow. Especially the circumferential averaging is the most uncertain at low flow. Also the internal flow visualisation and the static pressure measurements show that the circular and modified circular volutes exhibit some problems in the exit cone at low flow. Perhaps this comes better into view in the Cobra-probe measurements than in the efficiency measurements. The behaviour of the static pressure recovery coefficients is opposite to that of the total pressure loss coefficient and can be explained by the same reasons.

The ratio of the outlet dynamic pressure to the inlet dynamic pressure can be expressed in terms of the K_p and C_{pr} according to equation (26). If this ratio is above the unity, the flow accelerates and if it is below one, the flow decelerates.

$$\frac{P_{t5} - P_5}{P_{t3} - P_3} = 1 - (K_p + C_{pr}) \quad (26)$$

This ratio for the different volutes and exit cones is plotted in figure 50 using the averaging method 1 (left) and the averaging method 2 (right). Practically no differences are seen between the averaging methods. Figure 50 shows significant diffusion at all volume flows. The deceleration takes place mainly in the exit cone, since the volute was designed for a constant through flow velocity at the design flow. This extensive diffusion in the exit cone explains the rather high static pressure recovery coefficients shown in figure 49. The deceleration is greatest at low flow, when it takes place inside the volute as well.

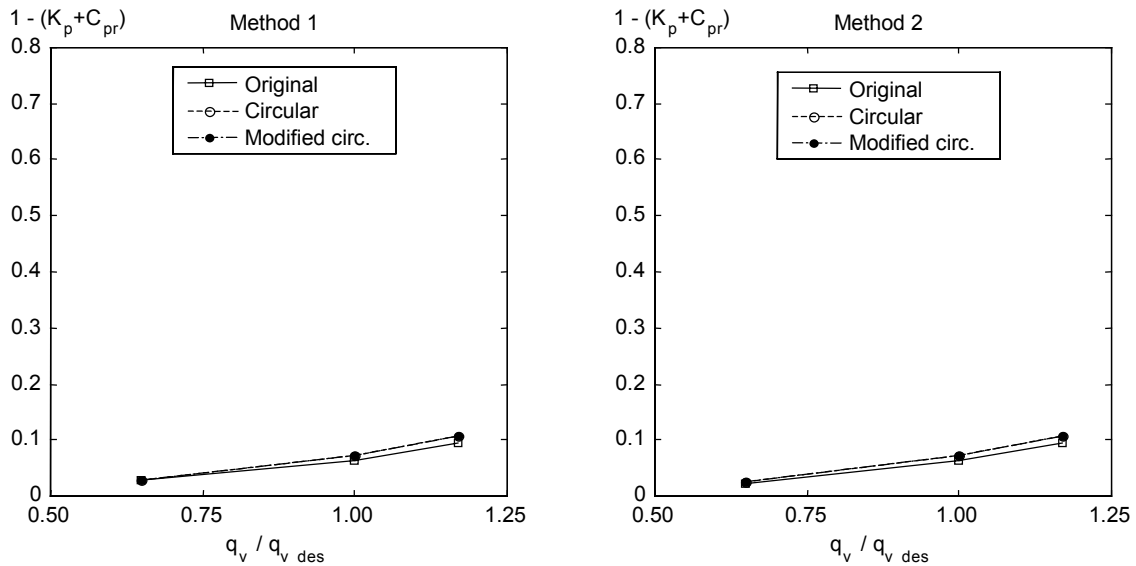


Figure 50. Ratio of the outlet dynamic pressure to the inlet dynamic pressure of the different volutes and exit cones as a function of volume flow using averaging methods 1 (left) and 2 (right).

4.6 Flow visualisation in the exit cone

The flow in the exit cone was visualised using tufts. First the tufts were taped on the exit cone surface and the movement of each tuft was recorded with a video camera one at a time, while the compressor was running at the design speed at different volume flows. Figure 51 shows two typical views observed on the video. On the left the movement of the tuft is fairly small, which is an indication of a steady turbulent flow (Yadav and Yahya 1980). The tuft on the right exhibits a much stronger whipping motion, which implies that some instabilities exist. The angle of the whipping motion was recorded for each tuft as indicated in figure 51. This angle was used to qualify the flow and is presented in figure 52 for each tuft in the different volutes at different flows.

The whipping motion of a tuft can be caused by two distinct reasons. The desired motion is caused by the instability of the flow under investigation, but the tufts have under certain conditions also a tendency to develop undesired, self-excited unstable motion (Crowder 1989). It is important to distinguish between these two types. The tufts used in the present experiments were first tested in a laminar flow wind tunnel, during which self-excited motion was not observed, but this does not guarantee stable tuft operation at all conditions in a turbulent flow. The tuft movement observed in the video in several occasions resembles somewhat the self-excited motion described by Crowder (1989). For this reason there is a risk

that a small part of the whipping motion may be a result of a self-excited instability. However, the present tufts can qualitatively be used to determine the flow stability, since the motion of each tuft clearly depends on the flow conditions in that point. This is shown by the fact that the motion of the tufts changes in a sensible way as the volume flow or the shape of the tongue is altered. Thus the motion of the tufts depends mainly on the flow conditions and less on self-excitation.

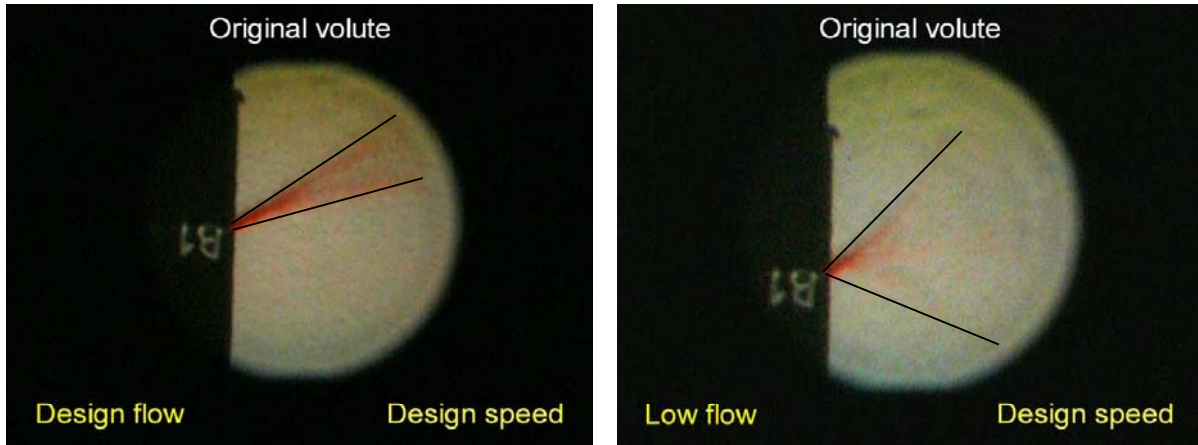


Figure 51. View of a surface tuft on the video. Steady turbulent flow on the left and unstable flow on the right.

The angle of the whipping motion of each tuft is presented in figure 52. Negative angles indicate a fixed reverse flow. The interpretation of the tuft motion has been adapted from Moore and Kline (1958) and Yadav and Yahya (1980), whose descriptions are presented in appendix B. In the present study the flow is considered as steady turbulent flow, when the angle is below $25^\circ - 30^\circ$. As the angle of the oscillation increases, the more turbulent and unstable the flow at that point becomes.

At low volume flow the static pressure in the beginning of the volute is lower than in the exit cone as shown by the pressure measurements. This causes recirculation of the flow from the exit cone back to the volute and is seen as steady reverse flow in tuft A2 in the original volute and in tuft A3 in the modified circular volute. Tuft A3 in the circular volute points downstream only because it is not located directly on the tongue, but some 20 mm further downstream due to the longer tongue of that volute. In the original volute tufts B2 and C2 are sucked to the small gap between the volute and the bottom plate due to the same pressure difference.

At low volume flow moderate instabilities are present in the original volute. It is easily noticed that the tufts close to the rectangular lower inner corner exhibit the largest motions. In the circular volute the flow is fairly steady apart from the wake of the tongue, which is seen as increased movement in tufts A4, B5 and C6. In the modified circular volute the flow is steady according to the surface visualisation, apart from the recirculation around the tongue.

	Low				Design				High							
	A	B	C		A	B	C		A	B	C		A	B	C	
Original volute	6	50*	45*	50	6	35*	30*	35	6	30*	25*	45	6	30*	25*	45
	5	30	35*	40*	5	30	30*	30*	5	30	30*	35*	5	30	30*	35*
	4	30	25	40*	4	25	25	25*	4	30	30	40*	4	30	30	40*
	3	50	35	60	3	25	20	20	3	25	30	50	3	25	30	50
	2	-10	G	G	2	20	15	20	2	30	30	90	2	30	30	90
	1	70	70	65	1	20	25	25	1	25	25	35	1	25	25	35
	0	40	50	50	0	20	25	25	0	25	25	30	0	25	25	30
Circular volute	7	30	25		7	25	25		7	35	45		7	35	45	
	6	25	30	45	6	25	30	30	6	35	45	65	6	35	45	65
	5	20	40	35	5	30	35	30	5	25	60	40	5	25	60	40
	4	45	30	30	4	45	30	25	4	150	45	35	4	150	45	35
	3	35	30	30	3	25	30	25	3	50	45	30	3	50	45	30
	2	30	30	30	2	30	30	25	2	35	40	35	2	35	40	35
	1	30	30	30	1	25	30	30	1	30	35	35	1	30	35	35
Modified circular volute	7	25			7	25			7	35			7	35		
	6	20	20	25	6	25	30	30	6	30	38	35	6	30	38	35
	5	25	25	25	5	30	30	25	5	30	30	30	5	30	30	30
	4	25	25	30	4	33	25	30	4	30	30	30	4	30	30	30
	3	-10	35	30	3	30	30	25	3	35	30	30	3	35	30	30
	2	35	30	25	2	30	25	30	2	35	30	30	2	35	30	30
	1	30	30	25	1	25	30	25	1	30	30	35	1	30	30	35

* The flow is locally disturbed by an uneven joint between the volute and bottom plate.

G The tuft was sucked into the gap between the volute and bottom plate.

Figure 52. The results of the surface flow visualisation in the exit cone. The numbers indicate the angle of the whipping motion of each tuft.

At the design volume flow the surface visualisation shows fairly steady flow in each volute. In the original volute slight local disturbances exist close to the uneven joint between the volute and compressor bottom plate. In the circular volute a small vortex is dispatched from the hump of the sharp tongue, which is seen as increased motion in tufts A4 and B5.

At high volume flow instabilities and considerable differences between the volutes arise. In the original volute the flow is stable on tuft rows A and B but becomes more unsteady on row C. The biggest disturbances occur next to the rectangular inner corner close to tufts C2 and C3, but all of the tufts still point constantly downstream. In the circular volute clear disturbance is dispatched from the sharp tongue due to the large incidence angle. This is indicated by tuft A4, which oscillates violently and is on the edge of pointing upstream. The vortex moves downstream along the swirling streamline hitting next tuft B5 and then tuft C6. This disturbance is almost completely eliminated in the modified circular volute, in which the tuft motion at high flow is only slightly increased in comparison to the design flow.

After the surface flow visualisation was carried out the surface tufts were removed and an internal flow visualisation was made. A tuft was attached to the end of a thin stick and was traversed across the exit cone starting from the position of the surface tuft B5. The movement of the tuft was recorded and interpreted in a similar manner as that of the surface tufts. The results of the internal flow visualisation are presented in table 2.

Table 2. The results of the internal flow visualisation in the exit cone. The height is measured from the bottom of the exit cone, and the numbers indicate the angle of the whipping motion of the tuft attached to the end of the stick.

Height	Original volute			Circular volute			Modified circular volute		
	Low	Design	High	Low	Design	High	Low	Design	High
0.80	30	30	25	45	35	30	360	25	-
0.75	35	35	35	60	35	35	360	30	30
0.50	45	35	45	360	35	50	360	45	45
0.25	40	30	25	50	15	35	70	25	25
0.00	35	20	25	30	25	40	30	25	30

The internal flow visualisation (table 2) reveals additional information on the flow. At the design flow rate the flow in the exit cone is fairly steady in all volutes, as the surface visualisation already showed. A small increase in the whipping angle is observed in the middle of the cone. This is a result of two factors: firstly the shear stress and total pressure

loss present in the vortex core is likely to cause some instability and additional turbulence, and secondly the tuft begins to swirl with the flow when its attachment point is in the vortex core. This swirling motion is seen as an increased angle of oscillation.

At high flow rate the flow behaviour resembles quite much that observed already in the surface visualisation. The flow is fairly steady in the original volute apart from the somewhat increased tuft movement in the middle of the cone. In the circular volute moderate disturbances are observed throughout the exit cone. These disturbances are almost eliminated in the modified circular volute. The increased tuft movement in the vortex core in all the volutes is a direct result from the increased swirl velocity at high volume flow.

At low volume flow clear differences are seen in comparison to the surface visualisation. In the circular volute the flow is very unstable in the middle of the exit cone and at times the tuft even points upstream in the vortex core. This unsteadiness is increased in the modified circular volute, where steady forward flow is seen only close to the bottom wall of the exit cone. For some reason the exit cone of the circular and modified circular volutes stalls at low flow according to the internal flow visualisation. The same tendency was also observed in the static pressure measurements shown in figure 41. In the original volute some disturbances are also present, but their order of magnitude is small.

4.7 Conclusions from the experimental work

A radial compressor with three different volutes was analysed experimentally. The overall performance of the compressor as well as the static pressure distribution after the impeller and on the volute surface were measured. The flow entering the volute was measured using a three-hole Cobra-probe, and flow visualisations were carried out in the exit cone of the volute.

Only small differences in the performance of the compressor with the different volutes exist according to the performance map and efficiency measurements. All the volutes performed equally at the design point. The biggest differences were observed at low speeds and high volume flows, i.e. when the flow entered the volute most radially. In this operating regime the efficiency of the compressor with the modified circular volute was about two percentage points higher than with the other volutes.

The circumferential static pressure distribution measured on the volute surface showed a typical behaviour for the volute. The pressure increased at small flow, stayed almost constant at the design flow and decreased at high flow. The small decrease observed in the pressure at the design flow indicates that the volute was slightly too small for the design flow of the impeller.

The non-uniform static pressure distribution of the volute was transmitted backwards across the vaneless diffuser and was observed at the impeller exit. At low volume flow a strong two-wave pattern developed into the static pressure distribution at the impeller exit due to the response of the impeller to the non-uniformity of pressure.

The static pressure measurements in the exit cone showed a desired pressure rise in the exit cones of all volutes at most operating points. However, two small problem areas were found. The pressure rise fell short from the desired in the end of the exit cone of the circular and modified circular volutes at low volume flow and in the beginning of the exit cone of the original volute at high flow.

The flow field at the volute inlet was measured in three circumferential locations with a three-hole Cobra-probe. The circumferential static pressure distribution at the volute inlet followed well the distribution measured on the volute surface. The distribution of the total pressure, in turn, was noticed to be more uneven and a notch in the total pressure was found at the 180° circumferential position at low flow. For these reasons the circumferential averaging of the total pressure using only three points is questionable, but was performed in order to get an estimate for the average static and total pressures at the volute inlet.

In order to judge the overall performance of the volutes and exit cones the total pressure loss and static pressure recovery coefficients were calculated using the average pressures at the volute inlet and exit cone outlet. The total pressure loss in each volute was seen to be lowest at the design flow and to increase at high and low flows. When comparing the pressure loss of the different volutes with each other, the modified circular volute was seen to perform best at high and design flows, while the original volute had the smallest loss at low flow.

The surface flow visualisation in the exit cone showed steady turbulent flow at the design volume flow in all volutes. Only a small vortex behind the sharp tongue of the circular volute

was seen. At high volume flow some unsteadiness was seen in the original volute. In the circular volute a notable disturbance originating from the sharp tongue was clearly present, while the flow behind the rounded tongue of the modified circular volute was fairly steady. At low volume flow the recirculation of the flow from the exit cone back to the beginning of the volute was seen, but otherwise the flow was steady in all volutes.

The results of the internal flow visualisation were quite close to those of the surface visualisation apart from the behaviour at low volume flow. At low flow the unsteady flow in the exit cone of the circular and modified circular volutes was clearly demonstrated by the violently oscillating tuft at the end of the stick.

5 NUMERICAL CALCULATION

5.1 General

The compressor was analysed also numerically in the course of this study. This was done to get a more detailed picture of the flow inside the compressor and volute than what could be obtained experimentally. The computational domain consisted of the entire compressor including the inlet pipe, inlet cone, full impeller, vaneless diffuser, volute, exit cone and the exit pipe. Thus the boundary conditions could be given in the same locations where the instrumentation of the test stand was. The analysis was performed only for the compressor equipped with the circular volute. Therefore the computational results can be used to analyse the flow in the compressor and volute, but not to compare the different volutes with each other. The main targets of the numerical analysis were to find out reasons for the not so optimal performance of the circular volute and to gain more information on effect of the volute on the compressor and impeller flow.

The fully three-dimensional, viscous, turbulent flow was calculated using Finflo, a Navier-Stokes solver developed at Helsinki University of Technology (HUT). The program was obtained from the Laboratory of Applied Thermodynamics at HUT as a working package, so the author of this thesis has not contributed to the programming of the flow solver.

The simplest way to calculate a radial impeller would have been to model one blade passage only and to use periodic boundary conditions. This approach, however, cannot account for the circumferentially varying conditions due to the volute, and therefore was not selected for the present research.

The flow in this study was calculated using a so called quasi-steady approach, in which the entire compressor was modelled. This accounts for the circumferentially varying conditions, but demands a massively larger grid and more computational time than the analysis of one blade passage only. The rotation of the impeller is accomplished by calculating the moving parts in a rotating co-ordinate system. In other words the co-ordinate axes rotate, but no part of the grid rotates. For this reason this method is sometimes called also frozen rotor calculation. The drawback of the quasi-steady method is that no time-dependent phenomena

can be calculated. In addition, strong wakes of the blades are present in stationary parts. In reality the flow would be naturally mixed out in the diffuser as the impeller rotates.

The most accurate and complicated method would have been a time-accurate analysis, in which the entire compressor would have been modelled. In that method the rotor mesh actually rotates and the moving and stationary parts of the grid are connected using a sliding mesh technique. In this way large scale time dependent phenomena can be captured. The calculation is, however, time averaged as regards to the calculation of turbulence, since Reynolds-averaged Navier-Stokes equations and an appropriate turbulence model are used. The time-accurate method has been incorporated in Finflo and some calculations have already been performed (Pitkänen et al. 1999, Reunanen et al. 2000). However, the requirement for computational time is huge, and thus the use of that method is still limited. The quasi-steady calculation performed in this work serves as a starting point for the time-accurate analysis, because the grid is the same and the quasi-steady solution is used as an initial guess in the time-accurate analysis. The purpose is to calculate the same case with the time-accurate method in the near future.

5.2 Governing equations and their solution method

Finflo solves Reynolds-averaged Navier-Stokes equations (RANS-equations) utilising the Finite Volume Method in a Cartesian co-ordinate system. Only an overview of the governing equations and their solution mechanism is presented here. More details can be found for example in Siikonen and Pan (1992), Siikonen (1995), Kaurinkoski and Hellsten (1998) and Rautaheimo et al. (1999).

The RANS equations and the equations for the kinetic energy and dissipation of turbulence can be written in a conservative form

$$\frac{\partial U}{\partial t} + \frac{\partial(F - F_v)}{\partial x} + \frac{\partial(G - G_v)}{\partial y} + \frac{\partial(H - H_v)}{\partial z} = Q \quad (27)$$

where the solution vector U is a vector of conservative variables

$$U = [\rho, \rho u, \rho v, \rho w, E, \rho k, \rho \varepsilon]^T \quad (28)$$

and the inviscid fluxes are

$$F = \begin{pmatrix} \rho \hat{u} \\ \rho u \hat{u} + p + \frac{2}{3} \rho k \\ \rho v \hat{u} \\ \rho w \hat{u} \\ E \hat{u} + pu + \frac{2}{3} \rho k \hat{u} \\ \rho \hat{u} k \\ \rho \hat{u} \varepsilon \end{pmatrix} \quad G = \begin{pmatrix} \rho \hat{v} \\ \rho u \hat{v} \\ \rho v \hat{v} + p + \frac{2}{3} \rho k \\ \rho w \hat{v} \\ E \hat{v} + pv + \frac{2}{3} \rho k \hat{v} \\ \rho \hat{v} k \\ \rho \hat{v} \varepsilon \end{pmatrix} \quad H = \begin{pmatrix} \rho \hat{w} \\ \rho u \hat{w} \\ \rho v \hat{w} \\ \rho w \hat{w} + p + \frac{2}{3} \rho k \\ E \hat{w} + pw + \frac{2}{3} \rho k \hat{w} \\ \rho \hat{w} k \\ \rho \hat{w} \varepsilon \end{pmatrix} \quad (29)$$

Here ρ is the density, u , v , and w are the absolute velocity components in a Cartesian coordinate system, p is the pressure, E is the total energy, k is the kinetic energy of turbulence and ε the dissipation of the kinetic energy of turbulence. The co-ordinate system rotates around the x -axis with an angular velocity Ω . Thus the rotational speed of the domain is

$$\vec{\Omega} \times \vec{r} = [0, -\Omega z, \Omega y]^T \quad (30)$$

The convective i.e. relative speeds are given by

$$\hat{u}_i = u_i - (\vec{\Omega} \times \vec{r})_i \quad (31)$$

thus the individual components of the relative speeds are

$$\begin{aligned} \hat{u} &= u \\ \hat{v} &= v + \Omega z \\ \hat{w} &= w - \Omega y \end{aligned} \quad (32)$$

The total energy E is defined as

$$E = \rho e + \rho \frac{u^2 + v^2 + w^2}{2} + \rho k \quad (33)$$

where e is the specific internal energy. The pressure is calculated from the equation of state of perfect gas

$$p = (\gamma - 1) \rho e \quad (34)$$

where γ is the ratio of specific heats. The source term Q on the right hand side of equation (27) is a vector of conservative variables.

$$Q = [0, 0, \rho \Omega w, -\rho \Omega v, 0, Q_k, Q_\varepsilon]^T \quad (35)$$

It has got non-zero components for the equations of y - and z -momentum due to the rotation. Also the equations of turbulence need source the terms Q_k and Q_ε which are described in chapter 5.3.

The viscous fluxes in equation (27) are

$$F_v = \begin{pmatrix} 0 \\ \tau_{xx} \\ \tau_{xy} \\ \tau_{xz} \\ u\tau_{xx} + v\tau_{xy} + w\tau_{xz} - q_x \\ \mu_k(\partial k/\partial x) \\ \mu_\varepsilon(\partial \varepsilon/\partial x) \end{pmatrix} \quad G_v = \begin{pmatrix} 0 \\ \tau_{xy} \\ \tau_{yy} \\ \tau_{yz} \\ u\tau_{xy} + v\tau_{yy} + w\tau_{yz} - q_y \\ \mu_k(\partial k/\partial y) \\ \mu_\varepsilon(\partial \varepsilon/\partial y) \end{pmatrix} \quad H_v = \begin{pmatrix} 0 \\ \tau_{xz} \\ \tau_{yz} \\ \tau_{zz} \\ u\tau_{xz} + v\tau_{yz} + w\tau_{zz} - q_z \\ \mu_k(\partial k/\partial z) \\ \mu_\varepsilon(\partial \varepsilon/\partial z) \end{pmatrix} \quad (36)$$

where q_i is the heat flux, μ_k is the diffusion coefficient of k , μ_ε is the diffusion coefficient of ε and the viscous stress tensor is

$$\tau_{ij} = \mu \left[\frac{\partial u_j}{\partial x_i} + \frac{\partial u_i}{\partial x_j} - \frac{2}{3}(\nabla \cdot \vec{V})\delta_{ij} \right] - \left(\overline{\rho u_i u_j} - \frac{2}{3}\rho k\delta_{ij} \right) \quad (37)$$

where μ is molecular viscosity and $\overline{\rho u_i u_j}$ the Reynolds Stresses. The Kronecker's Delta function δ_{ij} is defined as

$$\begin{cases} \delta_{ij} = 0, & \text{if } i \neq j \\ \delta_{ij} = 1, & \text{if } i = j \end{cases} \quad (38)$$

For the finite volume method, equation (27) is written in an integral form for a fixed region V with a boundary S

$$\frac{d}{dt} \int_V U \, dV + \int_S \vec{F}(U) \cdot d\vec{S} = \int_V Q \, dV \quad (39)$$

where U is the vector of conservative variables defined in equation (28) and $\vec{F}(U)$ is the flux vector. A discrete form of equation (39) is obtained by performing the integrations for a computational cell i

$$V_i \frac{dU_i}{dt} = \sum_{\text{faces}} -S\hat{F} + V_i Q_i \quad (40)$$

where S is the area of the cell face and the sum is taken over the faces of the computational cell i . The flux \hat{F} for each face is defined by

$$\hat{F} = n_x(F - F_v) + n_y(G - G_v) + n_z(H - H_v) \quad (41)$$

where n_x , n_y and n_z are the x -, y - and z -components of the unit normal vector. F , G and H are the inviscid and F_v , G_v and H_v the viscous fluxes in the x , y and z -directions as defined by equations (29) and (36).

The inviscid i.e. convective fluxes F , G and H are evaluated using Roe's flux difference splitting in a moving grid (Roe 1981). A MUSCL-type approach has been adopted for the evaluation of the primary flow variables (ρ , u , v , w , p) on the cell surfaces (Siikonen 1998).

The viscous i.e. diffusive fluxes F_v , G_v and H_v are evaluated using a thin-layer approximation (Siikonen 1998). The thin-layer model is activated in all co-ordinate directions.

Equation (40) is integrated in time implicitly by applying the *DDADI*-factorization (Lombard et al. 1983). The resulting implicit stage consists of a backward and forward sweep in every co-ordinate direction. The boundary conditions are treated explicitly, and a spatially varying time step is utilised. Furthermore, a multigrid acceleration of convergence is used. Hence, the integration is not accurate in time, but provides an iterative way to approach the steady-state.

5.3 Turbulence modelling

The calculation of turbulence is the most problematic part of computational fluid dynamics. In practical engineering calculations direct numerical simulation (DNS) is out of question and large eddy simulation (LES) practically impossible due to the vast amount of computational resources required. Reynolds-stress models are complicated and require also extensive computational power. The simpler methods, like two equation models or algebraic models, are often too simple and inaccurate in describing turbulence.

Rautaheimo et al. (1999) have compared the following three different turbulence models in a radial compressor calculation:

- Algebraic model of Baldwin and Lomax (1978)
- Two equation k - ε model of Chien (1982)
- Reynolds-stress model of Speziale et al. (1991)

Rautaheimo et al. (1999) conclude that the overall performance of the compressor was well predicted with the Baldwin-Lomax and Chien's $k-\varepsilon$ models, whereas the Reynolds-stress model slightly under-predicted the pressure ratio and efficiency. However, the vortices due to the tip clearance flow were best captured using the Reynolds-stress model. An interesting conclusion is that Chien's $k-\varepsilon$ model predicted the overall performance of the compressor relatively correctly even with a very coarse grid. The Reynolds-stress model is reported to be the most sensitive to grid size. All of the comparisons were made at the design point and no separation of the flow was observed. This contributes to the good results and small differences observed between the models.

Turunen-Saaresti (2001) has calculated the present case with the Baldwin-Lomax and Chien's $k-\varepsilon$ models. He concludes that in general Chien's $k-\varepsilon$ model gave better results than the Baldwin-Lomax. This was observed both in the overall performance of the compressor and in the pressure distribution and pressure loss of the volute. The Baldwin-Lomax model was also found to be more sensitive to grid size than Chien's $k-\varepsilon$ model.

For the above-mentioned reasons the final results for the present case were calculated using Chien's $k-\varepsilon$ model and only those results are presented in this work. Chien's $k-\varepsilon$ model is a low Reynolds number turbulence model, which means that the flow is calculated all the way to the surface i.e. no wall functions are used. This approach requires the grid to be dense near the surface, since the velocity gradients in a turbulent flow are strong close to the walls. The number of computational cells in the boundary layer should be 20 - 30 and the non-dimensional height of the first cell $y^+ \approx 1$, if the boundary layer is to be calculated correctly. In the model the Boussinesq approximation i.e. the eddy-viscosity assumption is made for the Reynolds-stresses.

$$-\overline{\rho u_i u_j} = \mu_T \left[\frac{\partial u_j}{\partial x_i} + \frac{\partial u_i}{\partial x_j} - \frac{2}{3} (\nabla \cdot \vec{V}) \delta_{ij} \right] - \frac{2}{3} \rho k \delta_{ij} \quad (42)$$

where μ_T is the turbulent viscosity. The source terms for equation (35) in Chien's model are

$$\begin{aligned} Q_k &= P - \rho \tilde{\varepsilon} - 2\mu \frac{k}{y_n^2} \\ Q_\varepsilon &= C_1 \frac{\tilde{\varepsilon}}{k} P - C_2 \frac{\rho \tilde{\varepsilon}^2}{k} - 2\mu \frac{\tilde{\varepsilon}}{y_n^2} e^{-\frac{y^+}{2}} \end{aligned} \quad (43)$$

where y_n is the normal distance from the wall and y^+ is the non-dimensional distance from the wall defined as

$$y^+ = y_n \frac{\rho u_\tau}{\mu_w} = y_n \sqrt{\frac{\rho \tau_w}{\mu_w}} \quad (44)$$

where u_τ is the friction velocity, μ_w is the molecular viscosity on the wall and τ_w is the shear stress on the wall. In Chien's model $\tilde{\varepsilon}$ is solved instead of the commonly used ε . $\tilde{\varepsilon}$ is defined so that it obtains zero value on the wall and the normal dissipation ε can be solved from

$$\varepsilon = \tilde{\varepsilon} + 2 \frac{\mu}{\rho} \frac{k}{y_n^2} \quad (45)$$

The production of turbulent kinetic energy P is modelled using the Boussinesq approximation

$$P = \left(-\frac{\overline{\rho u_i'' u_j''}}{\rho} \right) \frac{\partial u_i}{\partial x_j} = \left[\mu_T \left(\frac{\partial u_i}{\partial x_j} + \frac{\partial u_j}{\partial x_i} - \frac{2}{3} \frac{\partial u_k}{\partial x_k} \delta_{ij} \right) - \frac{2}{3} \rho k \delta_{ij} \right] \frac{\partial u_i}{\partial x_j} \quad (46)$$

In the k - ε model the turbulent viscosity μ_T is calculated from

$$\mu_T = C_\mu \frac{\rho k^2}{\tilde{\varepsilon}} \quad (47)$$

In order to avoid unphysical growth of the turbulent viscosity, the production of turbulent kinetic energy is limited as suggested by Menter (1994)

$$P = \min(P, 20 \rho \tilde{\varepsilon}) \quad (48)$$

The diffusion coefficients μ_k and μ_ε used in the viscous fluxes, see equation (36), are calculated as

$$\mu_k = \mu + \frac{\mu_T}{\sigma_k} \quad \text{and} \quad \mu_\varepsilon = \mu + \frac{\mu_T}{\sigma_\varepsilon} \quad (49)$$

The empirical coefficients used in the equations for k and ε are

$$\begin{aligned} C_1 &= 1.44 & \sigma_k &= 1.0 \\ C_2 &= 1.92 \left(1 - 0.22 e^{-\frac{\text{Re}_T^2}{36}} \right) & \sigma_\varepsilon &= 1.3 \\ C_\mu &= 0.09 \left(1 - e^{-0.0115 y^+} \right) \end{aligned} \quad (50)$$

where the turbulence Reynolds number is defined as $\text{Re}_T = \rho k^2 / \mu \tilde{\varepsilon}$. More details on the application of Chien's k - ε model in Finflo are given in Siikonen (1995).

5.4 Geometry and grid

As already mentioned, the calculation domain included all parts between the inlet and outlet measurement planes of the test stand. In other words the inlet boundary was located 1.05 m before the impeller and the outlet boundary 1.60 m behind the exit cone of the volute. The geometry was modelled and the grid generated in the Laboratory of Applied Thermodynamics at Helsinki University of Technology.

The main geometrical parameters of the compressor and circular volute were described in chapter 3. Some details of the geometry are shown in figure 53. The inner diameters of the inlet and exit pipes are 10 mm greater than the corresponding diameters of the inlet and exit cones, because the compressor mounting requires the outer diameters to be the same and the cast parts have greater wall thickness than the pipes. This causes a small step at the compressor inlet and outlet and was taken into account in the computational model as shown in figure 53. For simplicity, the impeller tip clearance was not modelled. Also, the hub surface at the impeller exit is located slightly higher than the diffuser hub wall due to the manufacturing tolerances in the test compressor. Thus the impeller blade passage height is 17.5 mm, but the vaneless diffuser height is 20.4 mm. The difference in height was assumed to be wholly on the hub surface in the computational model and was modelled as a step at the impeller exit, figure 53 on the right.

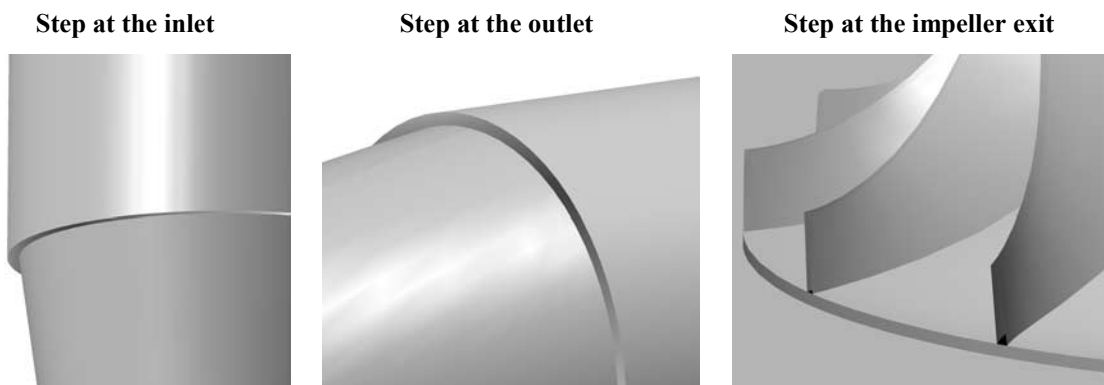


Figure 53. Three details of the geometry. From left to right: forward facing step at the inlet cone inlet, backward facing step at the exit cone outlet and backward facing step at the impeller exit.

The grid is structured and constructed of 33 different blocks, see figure 54. The inlet pipe and inlet cone were modelled with blocks 1 - 13, the impeller was modelled with blocks 14 - 27, the diffuser with blocks 28 and 29, the volute with block 30, the exit cone with block 31 and the exit pipe with blocks 32 and 33. The grid size was about 5 000 000 computational cells on

the finest i.e. on the first grid level. The surface grid on the coarsest i.e. on the third level is shown in figure 55. A view of the diffuser and volute grid on the first level at the 360° location is seen in figure 56. All of the calculations in this work were first calculated on the third, then on the second and finally on the first level. In this way a rather accurate initial guess was quickly calculated for the large grid of the first level. The detailed information on the grid size in different blocks and on different levels is given in appendix C.

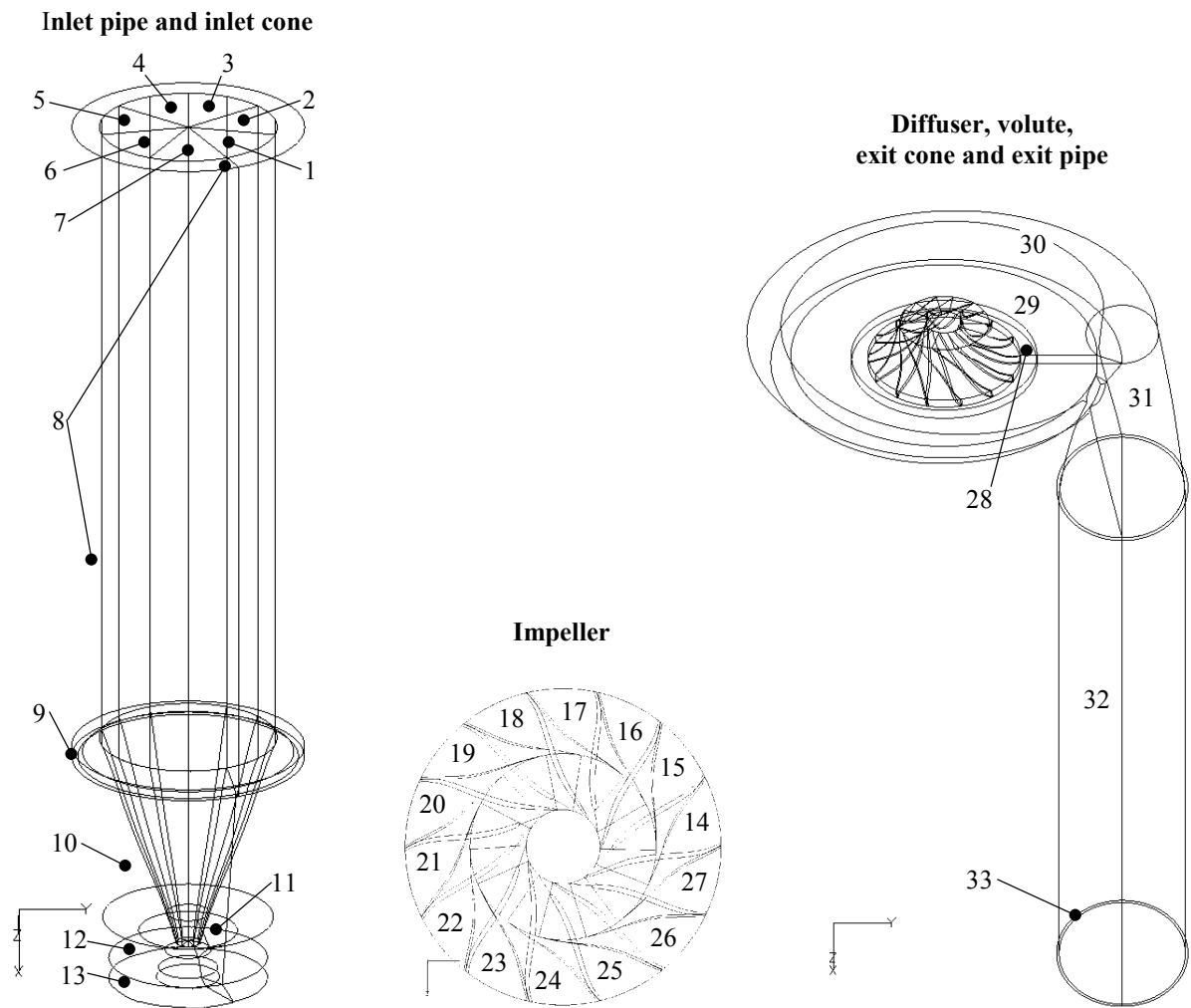


Figure 54. The location of the different blocks of the grid.

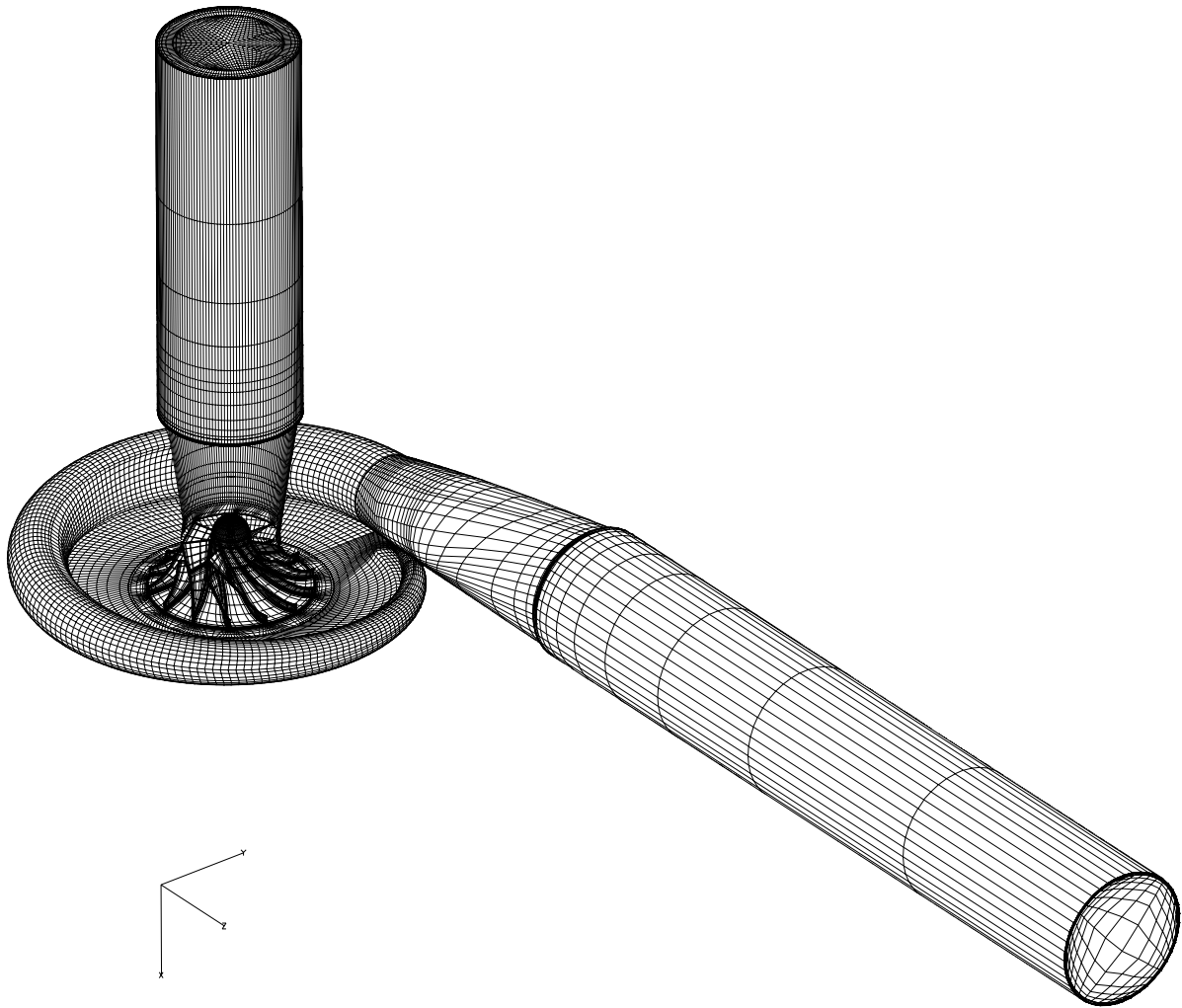


Figure 55. Surface grid of the whole computational domain on the third i.e. coarsest grid level.

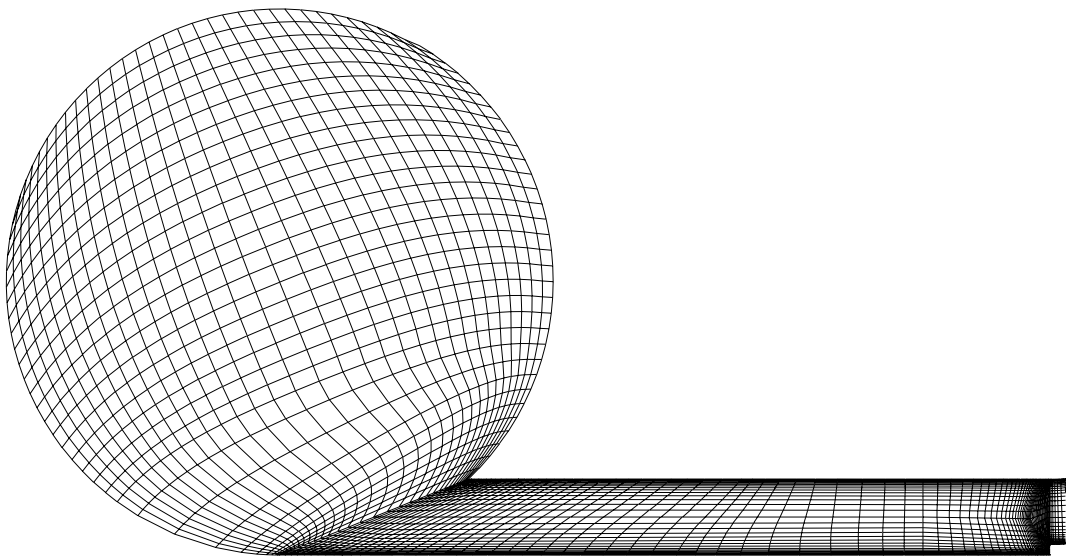


Figure 56. Grid of the volute and diffuser cross-section on the first i.e. finest grid level at the 360° circumferential position. The step at the impeller exit is seen in the bottom right corner.

The grid was clustered on the surfaces in all blocs except in the volute and the exit cone. The grid of the volute was constructed of one H-type block only due to the complexity of the volute and tongue modelling, thus it could not be clustered on the surfaces. The adjoining block of the exit cone had to be constructed in a similar way. The grid density on the surfaces is shown in figure 57 using the non-dimensional distance y^+ defined by equation (44). The y^+ is taken from the design flow calculation on the first grid level in the following locations:

- inlet pipe wall at the 0° circumferential location
- inlet cone wall at the 0° circumferential location
- impeller full blade suction side in block 14 about half way between the hub and shroud (at about 0° circumferential location)
- diffuser shroud wall at the 0° circumferential location
- volute top along the circumference
- exit cone top
- exit pipe top

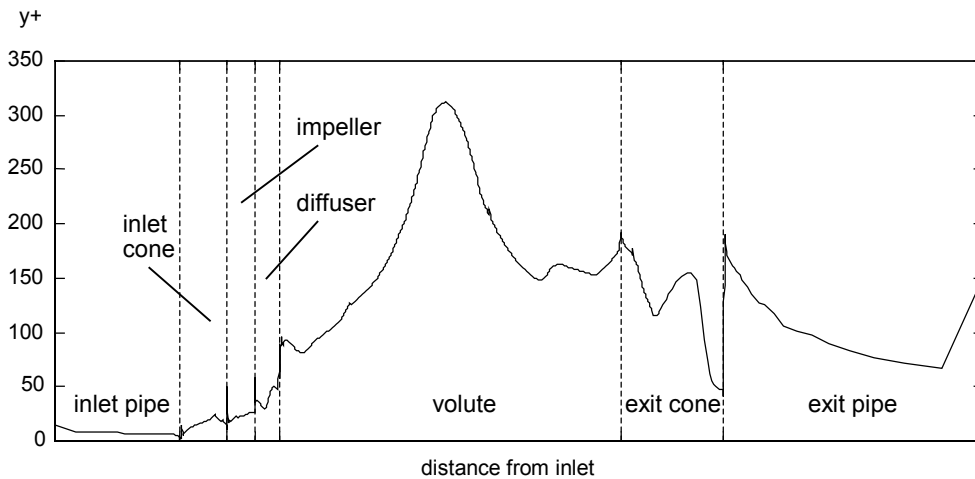


Figure 57. Surface y^+ throughout the computational domain.

The y^+ is around 10 in the inlet pipe, 10 - 20 in the inlet cone, 20 - 30 in the impeller, 30 - 50 in the diffuser, 100 - 300 in the volute, 50 - 200 in the exit cone and 50 - 200 in the exit pipe. The grid density near the surfaces would be adequate except in the volute, exit cone and exit pipe, if a high Reynolds number turbulence model with a wall function were used. For a low Reynolds number model the grid is far too coarse. It is evident that the boundary layer cannot be calculated correctly with the current grid density, since the low Reynolds number $k-\varepsilon$ turbulence model used in the calculations requires y^+ to be about 1. The coarse grid causes problems especially in the diffuser, volute and exit cone, because the boundary layer tends to separate due to the pressure gradient. Also the effect of the backward facing step at the impeller outlet and exit cone outlet cannot be estimated correctly due to the coarse grid.

However, the grid was generated in this way in order to get a sufficiently good qualitative result with the computational resources available. The number of cells is already big and the computational time relatively long. Also the results from Rautaheimo et al. (1999) show that it is possible to get relatively good results even with a coarse grid using the selected turbulence model. Naturally this is by no means a guarantee that the calculation would always work with a coarse grid.

5.5 Boundary conditions and numerical parameters

The inlet boundary condition was given 1.05 meters before the impeller leading edges. The mass flow, total enthalpy and flow direction were given as the boundary conditions. The inlet static pressure was extrapolated from the calculated flow field and the density was calculated using the static pressure and the given total enthalpy. The turbulence intensity was assumed to be $T_u = 2\%$ and the non-dimensional turbulent viscosity $\mu_T/\mu = 10$. The flow was assumed to be fully axial and the velocity as well as the turbulence quantities were assumed to have a constant distribution at the inlet. The velocity and turbulence profiles will develop a natural form before the impeller thanks to the relatively long inlet pipe.

The outlet boundary condition was defined at the end of the exit pipe 1.60 meters downstream from the exit cone of the volute. A constant distribution of static pressure was given as the outflow boundary condition. The rest of the flow variables were assumed to have a constant gradient at the outlet. The use of the rather long exit pipe allows a non-uniform distribution of the flow variables to exist at the end of the exit cone.

Each calculation was started with the first order discretisation of the convective fluxes, to increase robustness. When the solution had converged enough, second, and finally third order discretisation was used in all calculations. The Courant number, which controls the local time step, was varied according to the convergence between 1 and 2. Multigrid acceleration in levels 1 - 3 was used in all blocks.

6 NUMERICAL RESULTS

6.1 Calculated cases and convergence

The calculation was performed at the design speed at three volume flows denoted with low, design and high. Originally, the same volume flows that were used in the measurements were selected. However, during the calculation it was noticed that the calculation at low flow did not converge at all. For this reason the volume flow for the low flow calculation was increased from $q_v/q_{v, des} = 0.65$ to $q_v/q_{v, des} = 0.74$. This specific flow was chosen because the radial force, diffuser static pressure and volute static pressure measurements were also carried out at that flow. Thus only the Cobra-probe and detailed efficiency measurements were not available for direct comparison at low flow.

Figure 58 shows the convergence history of the calculations at low, design and high flows. The convergence criterion was based on the L_2 -norm of the residuals of density, L_2 -norm of the residuals of momentum in y -direction, averaged pressure and averaged temperature. In practise it has been observed that the averaged temperature is usually the last quantity to reach a constant value in compressor calculations. The number of iteration cycles required was about 14 000 for the design, 24 000 for the high and 45 000 for the low flow. The computation was performed at CSC - Scientific Computing Ltd with a Silicon Graphics Origin 2000 equipped with R12000 processors. The calculation was run in a parallel mode with six processors. The computational time was about one minute for one cycle, thus the total wall clock time required was as much as 230 hours for the design, 400 hours for the high and 750 hours for the low flow. Naturally the overall CPU-time consumed was about six times greater.

It can be seen that the solution at the design and high flows is reasonably well converged, but at low flow oscillations still exist. An attempt was made to dampen the oscillations by switching on the flux limiters after 24 000 cycles. This was of little help, as the convergence history shows, so the limiters were switched off at 31 000 cycles and the calculation was let to converge as much as possible. This attempt partially contributes to the requirement of large number of iterations at low flow. It has to be concluded, however, that the calculation at low flow is not fully converged and the result must be treated with extreme caution.

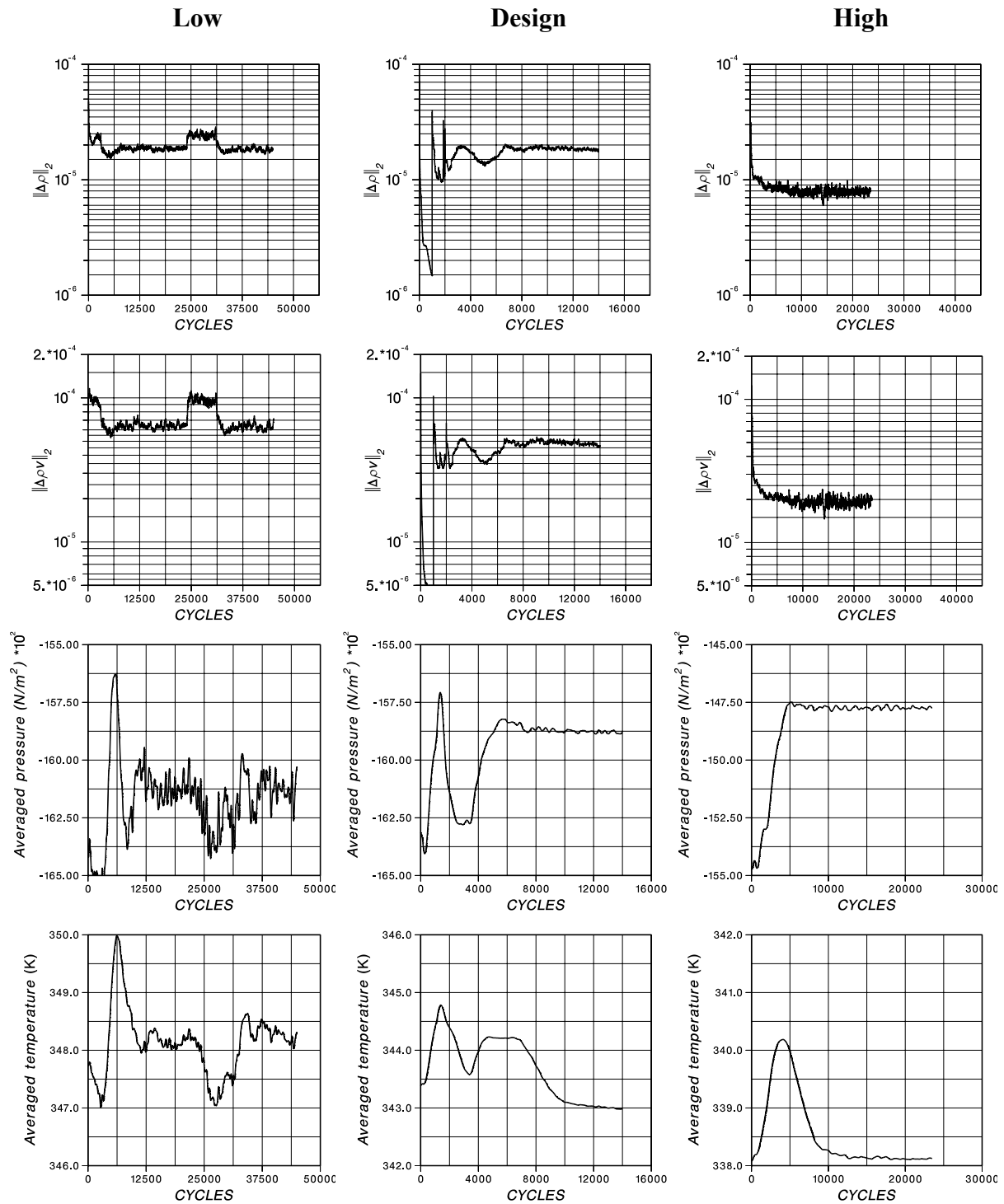


Figure 58. Convergence history of the density residual, momentum residual, averaged pressure and averaged temperature at low, design and high flow.

The presumed reason for the oscillations at low flow can be seen in figure 59. The step at the impeller exit causes the flow to separate on the hub surface at the diffuser inlet. Due to the far too coarse grid in the diffuser, the separation and re-attachment of the flow cannot be calculated correctly. At low flow the pressure gradient in the diffuser is so strong that a large area of reverse radial velocity forms onto the hub wall of the diffuser. According to the

monitor file, the biggest residuals at low flow were always in this region, which indicates that the solution oscillated in the separated area.

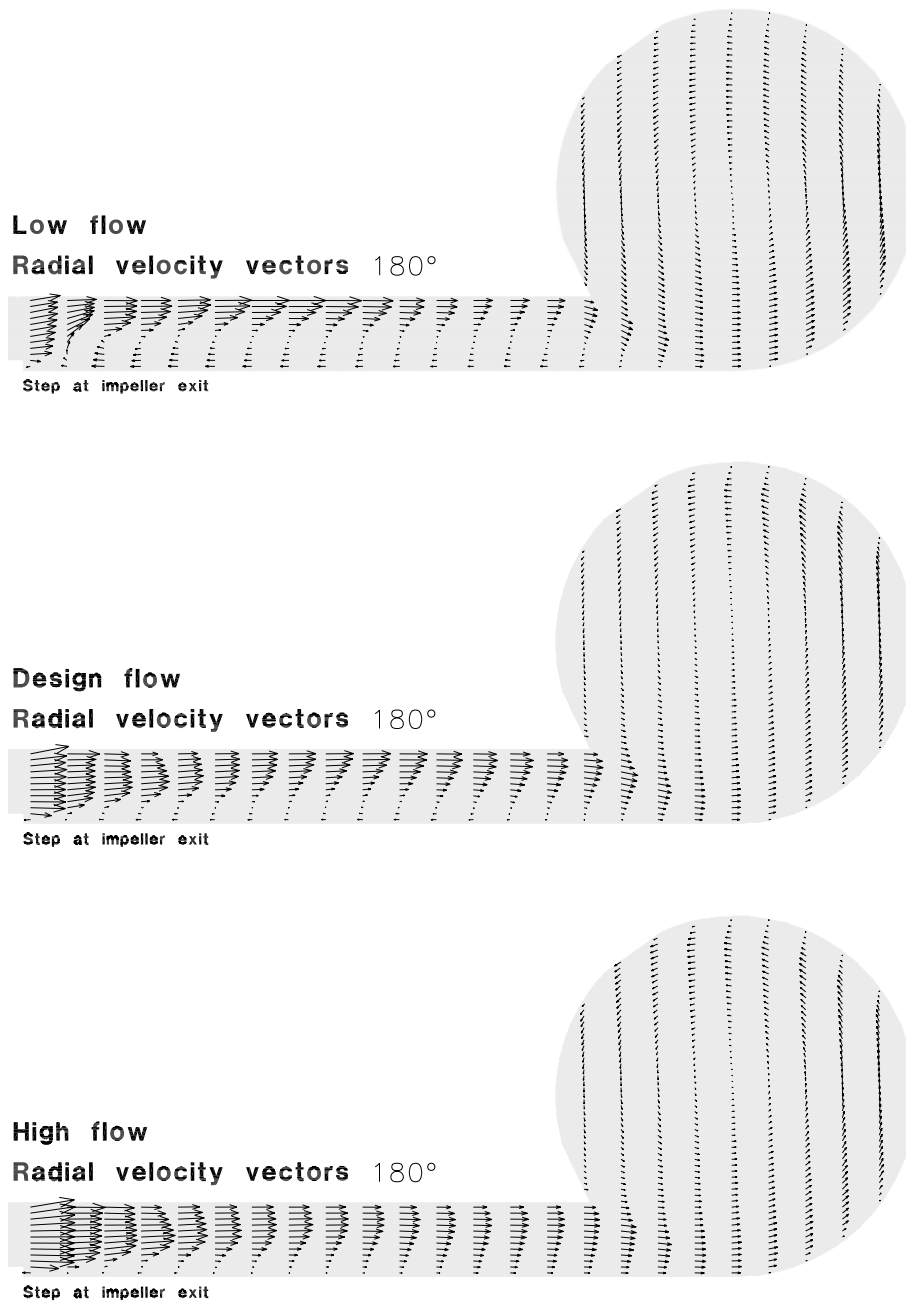


Figure 59. Radial velocity vectors in the diffuser and volute at the circumferential location of 180° at low, design and high flow.

Certainly the step causes a small separation in the reality as well, but such a large area of negative radial velocity is not supported by the measurements made at the diffuser outlet (see chapter 4.4). The separated region becomes the smaller the higher the flow is, but it is over-predicted at all flows. This results in an incorrect volute inflow condition. Contrary to the

reality, the radial velocity at the volute inlet increases as the volume flow decreases, since the reverse flow blocks most of the diffuser flow area and forces the forward flow close to the shroud wall to a narrow high speed jet. As a result of this the swirl inside the volute is too strong at low flow. The intensity of the swirl can be characterised by the non-dimensional swirl number, S , which is defined as a ratio of the axial flux of swirl momentum to the axial flux of axial momentum (Gupta et al. 1984).

$$S = \frac{\int_0^{\infty} \left(\rho c_{through} c_{swirl} + \overline{\rho c''_{through} c''_{swirl}} \right) r^2 dr}{r_w \int_0^{\infty} \left(\rho c_{through}^2 + \overline{\rho c''_{through}^2} + (p - p_{\infty}) \right) r dr} \quad (51)$$

where ρ is the density, $c_{through}$ the through flow velocity, c_{swirl} the swirl velocity, r the radius from the centre of the volute cross-section to each point, r_w the radius from the centre of the cross-section to the volute wall and p the static pressure. If the contributions of the fluctuating components and the pressure gradient to the momentum fluxes are assumed to be negligible, equation (51) can be simplified to

$$S = \frac{\int_0^{\infty} \left(\rho c_{through} c_{swirl} \right) r^2 dr}{r_w \int_0^{\infty} \left(\rho c_{through}^2 \right) r dr} \quad (52)$$

The swirl number in the whole volute channel calculated according to equation (52) is 0.054 at low flow, 0.043 at the design flow and 0.046 at high flow. Figure 60 shows the swirl number in the different volute cross sections for the low, design and high flows. It is seen that the swirl is the strongest at low flow and about equally strong at the design and high flows.

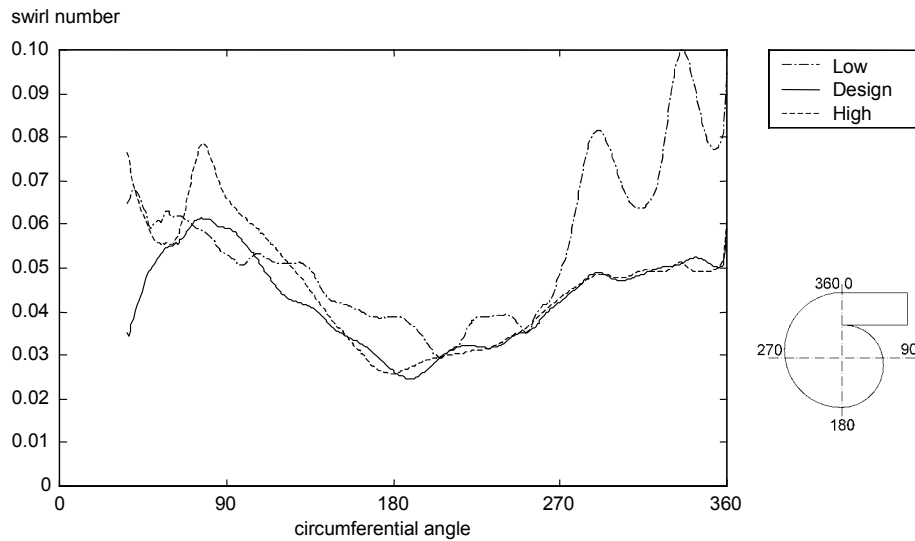


Figure 60. Swirl number in the different volute cross-sections at low, design and high flow.

6.2 Overall performance of the compressor and the volute

In order to calculate the overall performance of the compressor and its specific parts, the numerical results were averaged using mass flow -based weighting

$$\bar{x} = \frac{\sum \rho_i A_i c_{ni} \cdot x_i}{\sum \rho_i A_i c_{ni}} \quad (53)$$

where x_i is the quantity to be averaged, ρ_i the density, A_i the area and c_{ni} the velocity normal to the area A_i in each computational cell i . The mass flow averaged values were calculated for the compressor inlet and outlet as well as for the states 2, 3, 4 and 4'.

Table 3 shows the calculated and measured overall isentropic total-to-total efficiency and pressure ratio of the compressor at three volume flows. The measured values in table 3 are taken from the detailed efficiency measurements described in chapter 4 except for the low flow, which is higher than the low flow in the detailed measurements. Thus the measured overall performance of the compressor for the calculated low flow is taken from the performance map by interpolating the required point.

Table 3. Calculated and measured isentropic total-to-total efficiency and pressure ratio of the compressor at low, design and high flow.

	$q_{v\ ref} [-]$		$\pi_{t-t} [-]$		$\eta_{s\ t-t} [\%]$	
	CFD	measured	CFD	measured	CFD	measured
Low flow	0.74	0.74	2.07	2.12	76.1	76.3
Design flow	0.99	1.00	2.01	2.01	79.3	76.0
High flow	1.15	1.17	1.87	1.85	76.5	68.8

It is seen that the pressure ratio is predicted extremely well at the design and high flows and reasonably well at low flow. The isentropic efficiency is correct at low flow, but is over-predicted at the design and high flow. The discrepancies are most likely due to the too coarse grid especially near the surfaces and in the volute. The over-predicted efficiency and correct pressure ratio at high and design flows indicate that the temperature rise is slightly under-predicted in the calculation. As the flow rate decreases, the increased loss in the diffuser due to the flow separation compensates this. At low flow the pressure ratio falls short of the measured one due to the high loss in the diffuser. This together with a slightly under-predicted temperature rise results in correct efficiency at low flow.

The numerical calculation and averaging allows the different components and their parts to be examined separately. A good overview of the overall performance of the compressor and its different components can be seen in the h,s -diagram presented in figure 62. The calculated performance of the diffuser, volute and exit cone is presented in table 4 using the static pressure recovery coefficient and the total pressure loss coefficient. In addition, figure 61 shows the overall performance of the volute and the exit cone as a function of the volume flow, as well as comparison to the experimental data.

The following conclusions can be made from table 4 and h,s -diagrams:

- The impeller performance is high at the design and low flows (the most vertical line in the h,s -chart) and decreases at high flow.
- The diffuser (2→3) is not performing very well, and the losses in the diffuser increase as the flow decreases. The phenomenon is mainly due the flow separation on the hub surface and is exaggerated in the calculation.
- The calculated loss of the volute (3→4) is the highest at low flow and has an equal value at the design and high flows. This is contradictory to the trend reported for example by Ayder (1993), but corresponds well with the calculated swirl number in the volute. When the performance is examined between states 3 and 4', the losses increase only slightly at low and design flows, but moderately at high flow indicating that the tongue region causes additional losses at high flow. When the exit cone is added to the examination, the main increase of losses occurs at high flow and a moderate increase at low flow. Thus the calculated total pressure loss in the volute and exit cone combination (states 3→5) is the highest at low flow, the smallest at the design flow and moderate at high flow. This kind of behaviour differs somewhat from those reported by other researchers, see figure 2, due to the incorrect swirl. The calculated loss corresponds fairly well with the measured one, however, although the level of the loss is slightly under-predicted. This is most likely due to the far too coarse grid in the volute, especially near the surfaces.
- The static pressure in the volute (3→4) increases at low flow, stays practically constant at the design flow and decreases at high flow as expected. When the volute and the exit cone are analysed together (3→5), the static pressure rises at all flows due to the pressure recovery of the exit cone. Also, the variation of the pressure rise as a function of the volume flow is smaller than for the volute alone. The calculated trend follows reasonably

well the measured one, although the calculation slightly over-predicts the static pressure rise between states 3 and 5.

- The static pressure rises considerably in the beginning of the exit cone (4→4') at all volume flows. This part is, however, connected to the diffuser through the tongue gap, causing this high pressure to significantly increase the static pressure non-uniformity around the diffuser circumference.

Table 4. Calculated total pressure loss and static pressure recovery coefficients of the diffuser, volute, exit cone beginning, exit cone end and volute-exit cone combination at low, design and high flow.

Component	States	Total pressure loss, K_p			Static pressure recovery, C_{pr}		
		Low	Design	High	Low	Design	High
Diffuser	2→3	0.36	0.30	0.27	0.39	0.50	0.56
Volute	3→4	0.32	0.21	0.21	0.32	0.04	-0.37
Exit cone beginning	4→4'	0.07	0.02	0.05	0.56	0.60	0.48
Exit cone end	4'→5	0.32	0.11	0.17	0.49	0.67	0.63
Exit cone total	4→5	0.19	0.06	0.13	0.74	0.86	0.78
Volute + exit cone beg.	3→4'	0.34	0.22	0.27	0.53	0.49	0.19
Volute + exit cone total	3→5	0.39	0.25	0.36	0.59	0.69	0.53

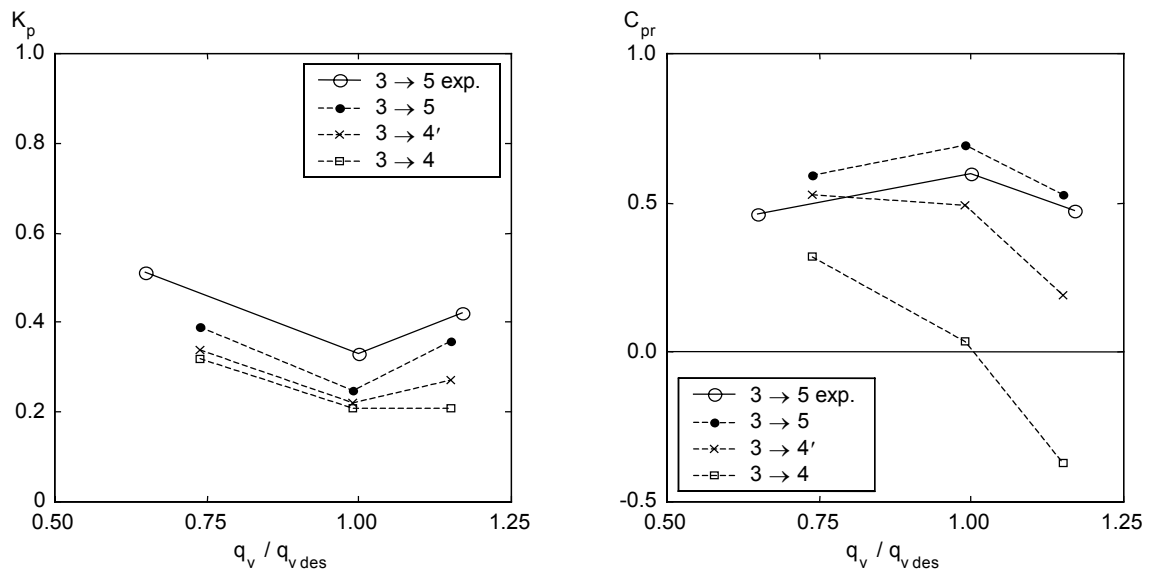


Figure 61. The calculated overall performance of the volute (3→4), the volute + exit cone beginning (3→4') and the volute + exit cone (3→5) as well as comparison to the experimental data.

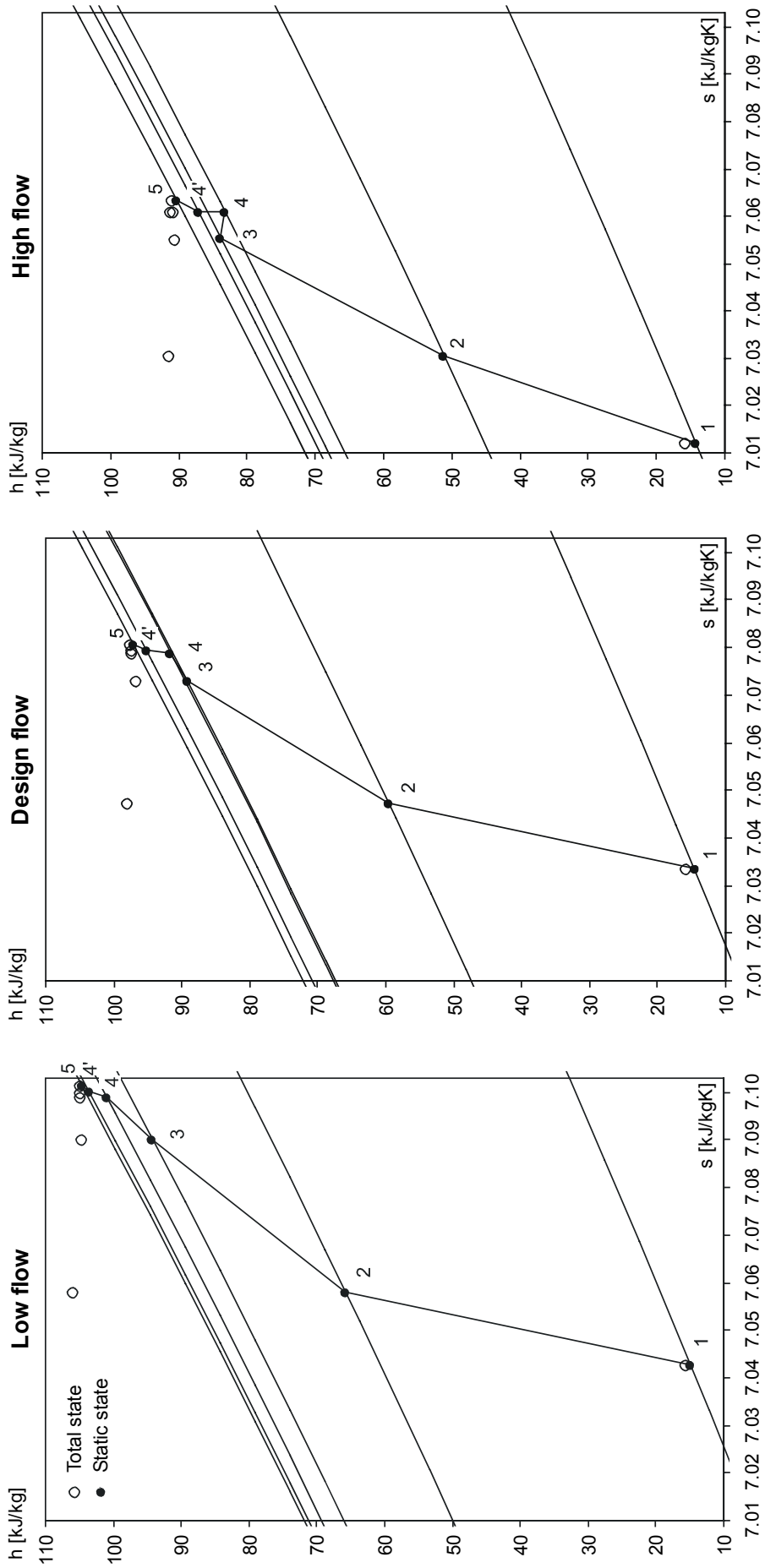


Figure 62. Calculated h,s -diagram of the compressor at low, design and high flow.

6.3 Circumferential distribution of the flow variables in the diffuser and the volute

The calculated total and static pressures at the vaneless diffuser inlet and outlet were averaged spanwise across the diffuser height using mass flow -based averaging in order to examine the circumferential distortion caused by the volute.

Figure 63 shows the circumferential distribution of the spanwise averaged static and total pressure at the diffuser inlet at radius ratio $r/r_2 = 1.01$. The static pressure measured on the shroud wall is shown for comparison. Both the calculated and measured pressures are made non-dimensional by dividing them by the total pressure at the compressor inlet. The wakes of the 14 blades are distinct both in the static and total pressure. The calculated static pressures agree well with the measured ones, although straight comparison is slightly difficult, since the measured static pressure is time averaged. The non-uniformity of the volute can be seen at the diffuser inlet. The static pressure along the circumference is almost constant at the design flow, decreases at high flow and increases at low flow, when the individual wakes are filtered out. The same trend can be found in the total pressure as well, but the strong wakes make it difficult to see. It is also seen that the two-wave pattern of the static pressure at low flow is not captured by the calculation. The reason for this is most likely the inability of the quasi-steady calculation to capture the time-dependent phenomena, which determine the impeller response to the non-uniform pressure distribution.

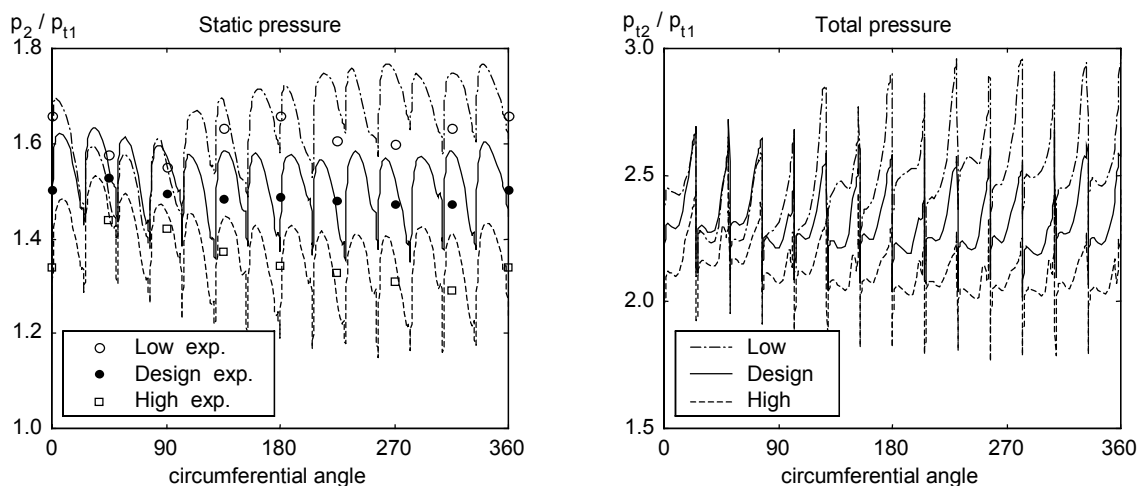


Figure 63. Circumferential distribution of the spanwise averaged non-dimensional static and total pressure at the vaneless diffuser inlet at radius ratio $r/r_2 = 1.01$. The static pressure measured on the shroud wall is shown for comparison.

The circumferential distribution of the calculated spanwise averaged static and total pressure at the diffuser outlet at radius ratio $r/r_2 = 2.02$ is shown in figure 64. The spanwise averaged static and total pressures measured with the Cobra-probe are shown for comparison, but it has to be remembered that the low flow during the measurement was smaller than during the calculation. The wakes have been attenuated considerably in the diffuser. It is interesting to note that only 7 wakes corresponding to the number of full blades can be seen in the total pressure. The wakes are clearly smaller in the static pressure, as was the case at the inlet of the diffuser as well. The calculated static and total pressures agree very well with the measured ones at high flow, at the design flow the agreement is still fairly good, but at low flow discrepancies exist. The calculated static pressure rise falls short from the measured one due to the incorrect flow separation in the diffuser. The difference is enhanced by the fact that the flow in the calculation was 14% bigger than during the measurement.

The non-uniformity of the static pressure is clearly seen at the diffuser outlet. At high flow the static pressure is at the highest in the beginning of the volute and decreases steadily along the circumference until a rise just before the 360° location begins. At low flow the static pressure is at the lowest around the tongue and increases first strongly and then moderately along the circumference. At the design flow the static pressure is fairly constant apart from a small peak in the area between 350° and 45°. This peak is caused by the strong diffusion in the beginning of the exit cone (states 4→4'). Since the beginning of the exit cone is connected to the diffuser, the local pressure rise is transmitted over to the diffuser. This phenomenon augments the circumferential pressure gradient in the same location at low and high flows as well.

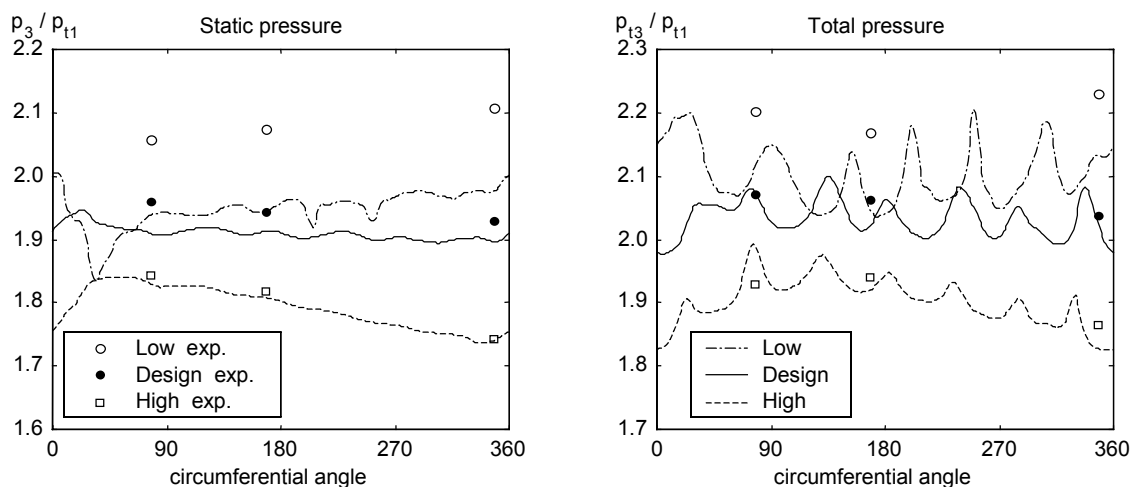


Figure 64. Circumferential distribution of the spanwise averaged non-dimensional static and total pressure at the vaneless diffuser outlet at radius ratio $r/r_2 = 2.02$.

The total pressure decreases at high flow, stays fairly constant at the design flow, and increases slightly at low flow, as expected. However, the peak point is no longer situated in the same location as the peak of the static pressure. This phase shift is discussed below in connection with figure 66.

The calculated and measured distribution of static pressure on the volute and exit cone top surface is shown in figure 65. The length of the exit cone is transformed into angles in order to present the pressures in the same figure, thus the angles between 0 and 360° represent the volute and the angles between 360° and 457° represent the exit cone. The pressure is again non-dimensionalized by dividing it by the total pressure at the compressor inlet. The agreement between the calculated and measured pressures is very good except at low flow. At low flow the trend is correct, but the pressure level in the volute is too low due to the too small static pressure rise in the diffuser. The separation observed already in the experiments in the exit cone of the circular volute at low flow is seen as poor static pressure rise also in the calculation. The non-uniformity of the pressure at off design conditions is clearly seen on the volute top, too. The beginning of the exit cone, which is connected to the diffuser, is located between 360° and 389°. Static pressure rise in this area is evident, and it increases the pressure asymmetry at the diffuser outlet. It is interesting to note that the calculated pressure drops sharply in the 360° location. The same drop is seen in the measurements, but more weakly. The apparent reason for the local pressure drop is the rather sharp transition from the volute to the exit cone.

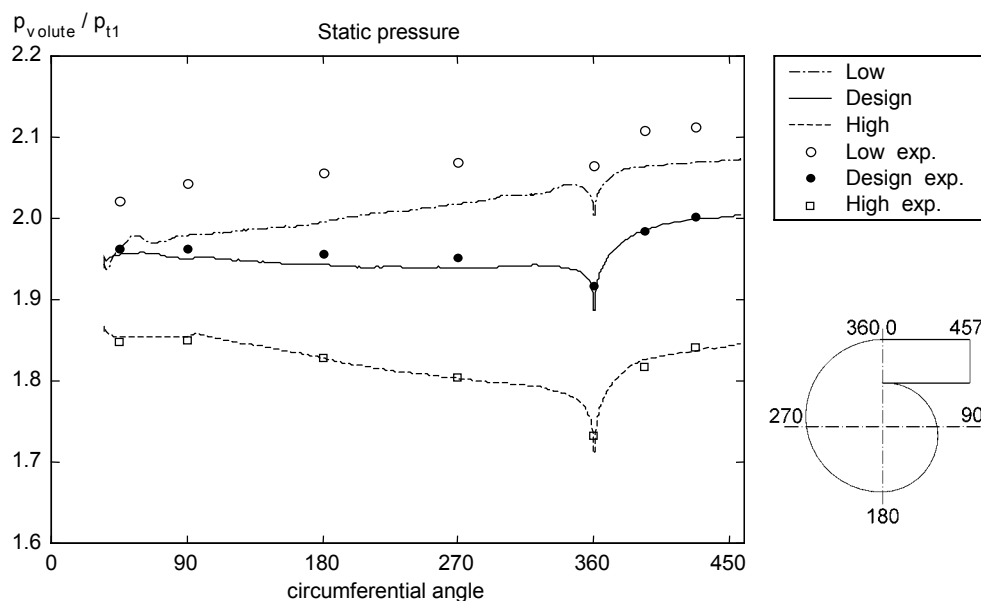


Figure 65. Circumferential distribution of the non-dimensional static pressure on the volute and exit cone top.

Figure 66 shows the calculated static and total pressures at the impeller exit at $r = r_2$ and at the vaneless diffuser outlet at $r/r_2 = 2.02$ at low, design and high flow. The pressures at the diffuser outlet are spanwise averaged, and are the same ones as presented in figure 64. The pressures at the impeller exit are averaged in each blade passage, thus only 14 values are presented along the circumference. In this manner the wakes are eliminated and the circumferential variation is seen better. It can be noted that only a small variation in the static pressure between the adjacent blade passages is present. The total pressure, however, fluctuates more between the neighbouring passages. A small difference between the full and splitter blade would be physically viable, but such a large variation as observed at low flow is an indication of poor convergence.

The distribution of the static pressure is transmitted from the volute across the diffuser to the impeller exit without a phase shift. In other words the high and low static pressures are located at the same angles both at the impeller and diffuser outlets. The distribution of the total pressure, in turn, shows a phase shift between the impeller exit and diffuser outlet. The high static pressure at the impeller blade passage exit causes that blade passage to produce high total pressure. The high total pressure released at the impeller exit hits the diffuser outlet about 150° later at low flow, some 90° later at design flow and approximately 50° later at high flow. This delay corresponds to the shape of the logarithmic spiral stream lines in the diffuser, and is actually a result of the same phenomenon as shown in figure 47. The same behaviour has also been reported by Hillewaert and Van den Braembussche (1999). In the present analysis only time averaged simulation was performed, and thus not all the time-dependent phenomena were captured as was the case in Hillewaert and Van den Braembussche (1999). Also the strong wakes in the total pressure due to the quasi-steady analysis make the phase shift more difficult to see.

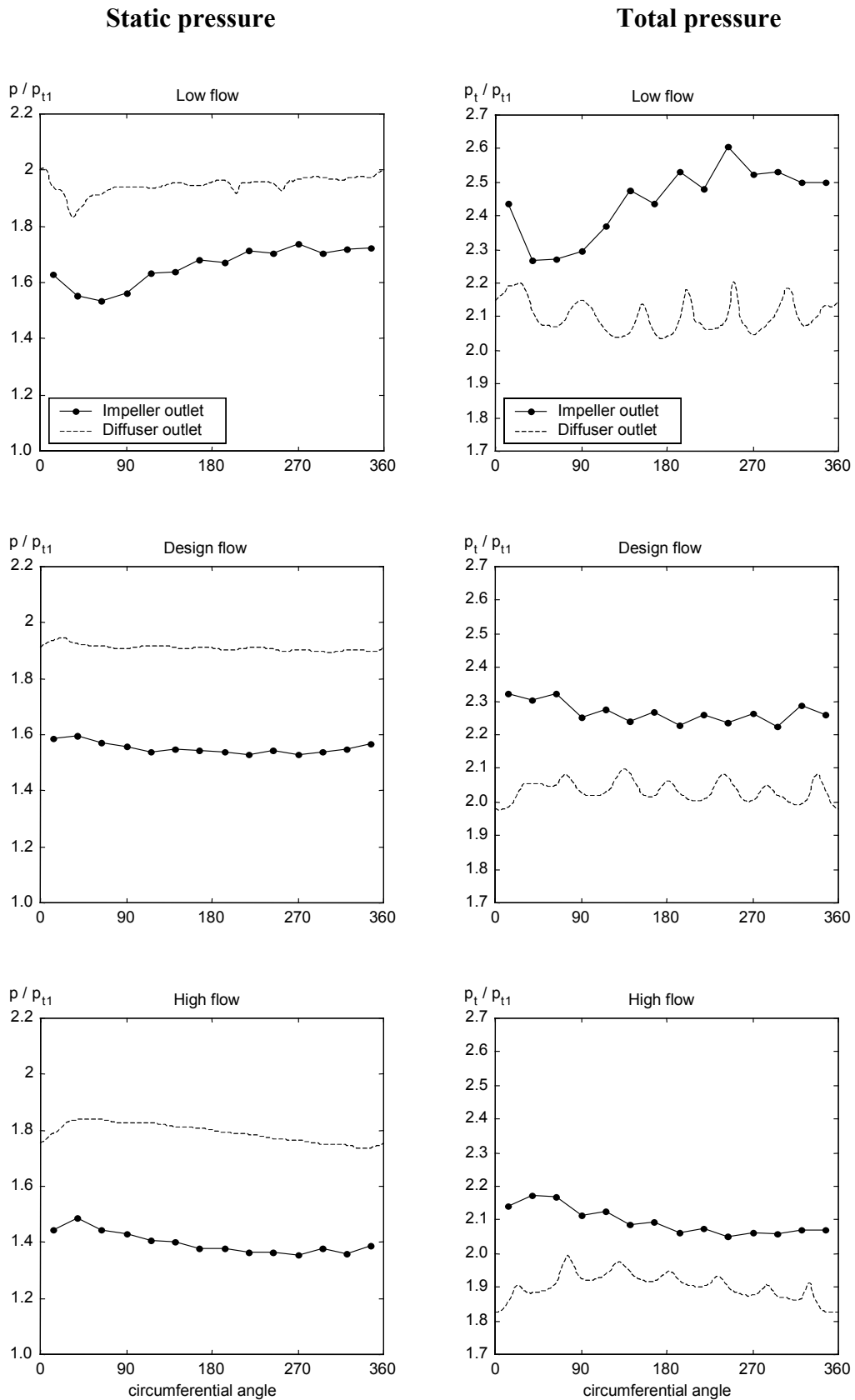


Figure 66. Circumferential distribution of the static and total pressure at the impeller and diffuser outlet. The pressure at the impeller outlet is mass flow averaged in each blade passage and the pressure in the diffuser outlet is spanwise averaged.

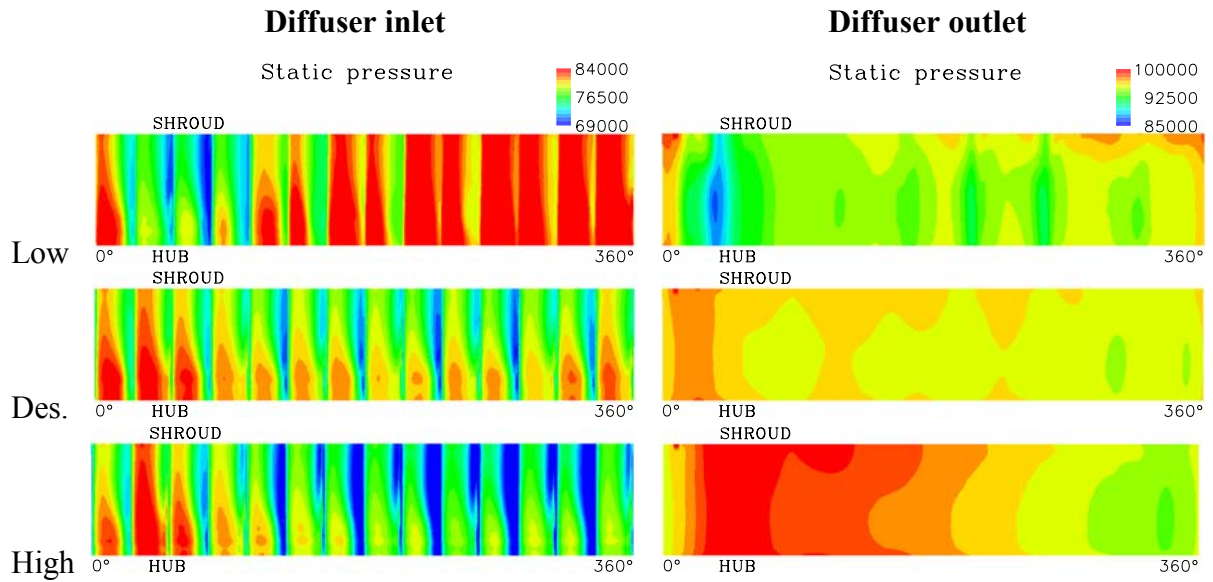


Figure 67. Static pressure at the vaneless diffuser inlet (left) and outlet (right).

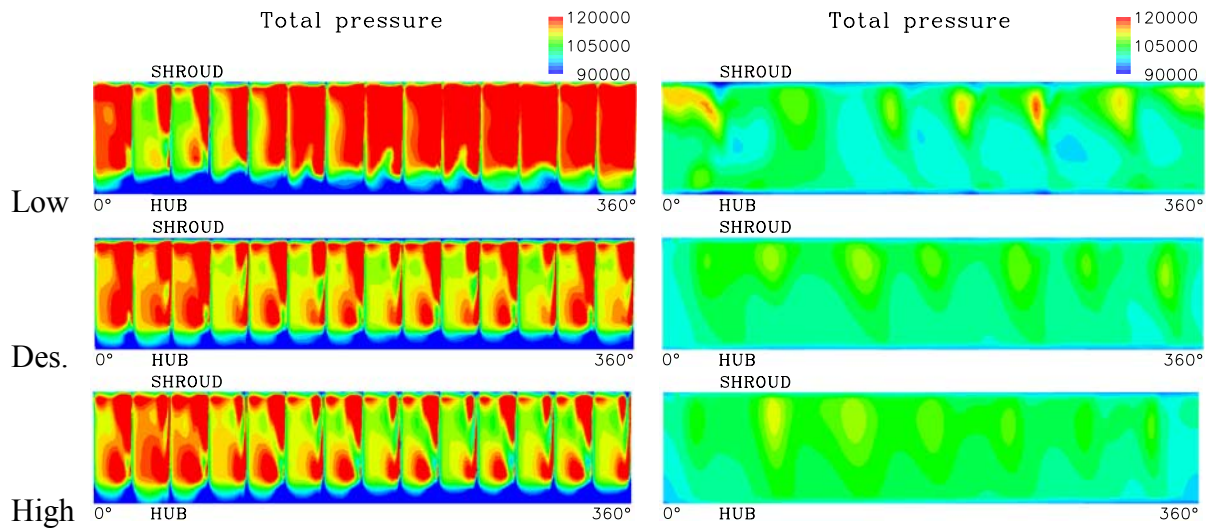


Figure 68. Total pressure at the vaneless diffuser inlet (left) and outlet (right).

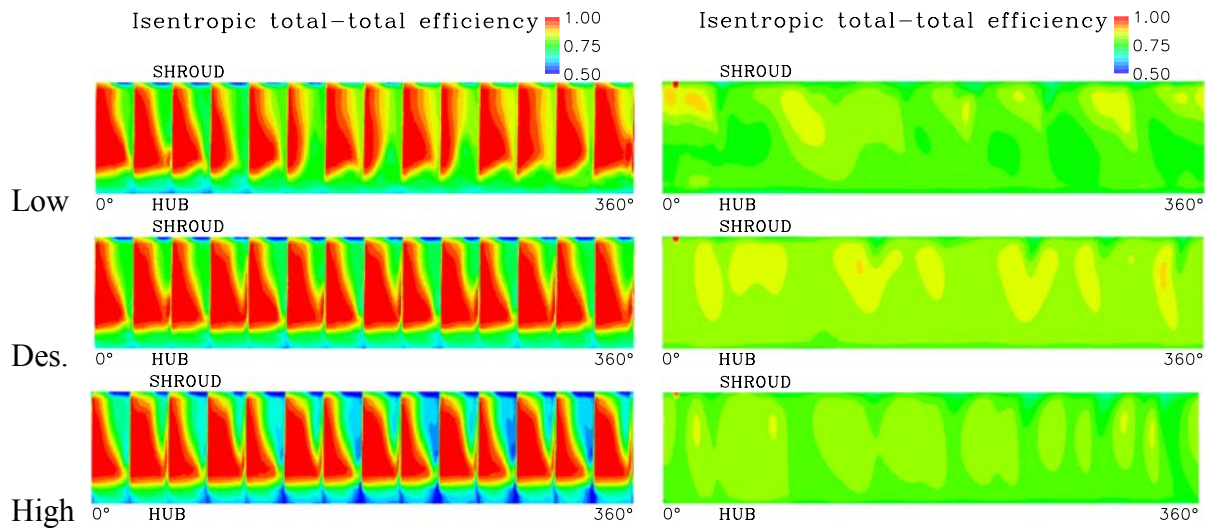


Figure 69. Isentropic total-to-total efficiency at the vaneless diffuser inlet (left) and outlet (right).

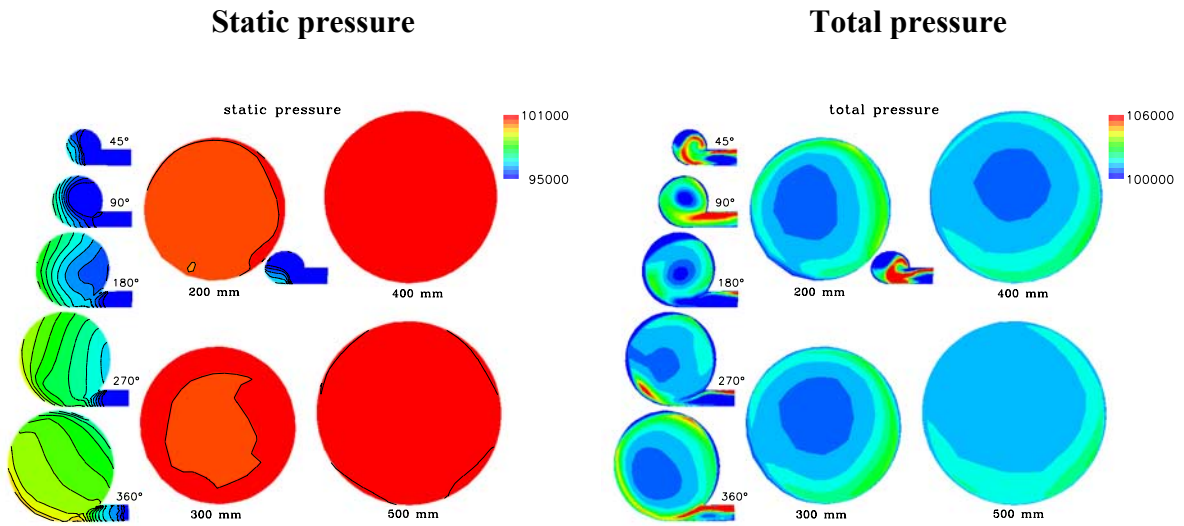


Figure 70. Static pressure (left) and total pressure (right) in the volute and exit cone at **low flow**.

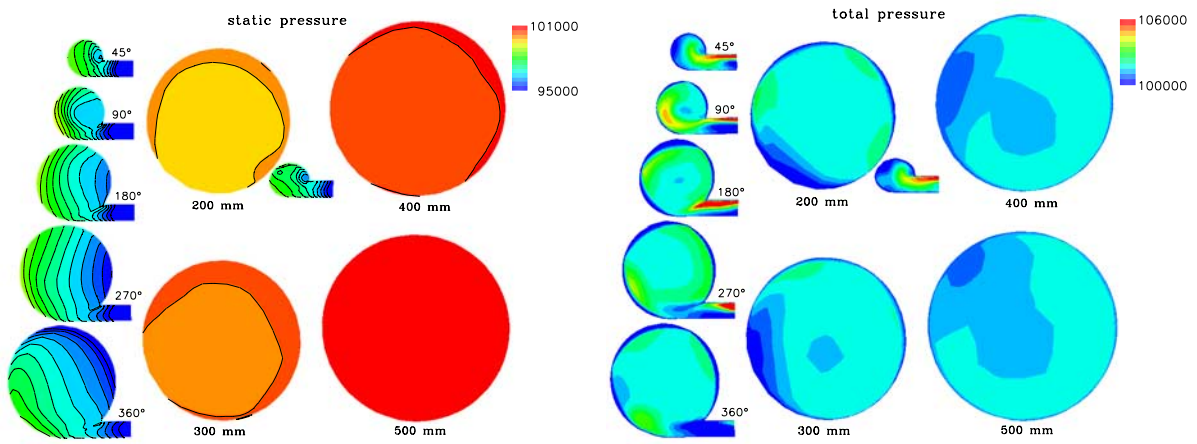


Figure 71. Static pressure (left) and total pressure (right) in the volute and exit cone at the **design flow**.

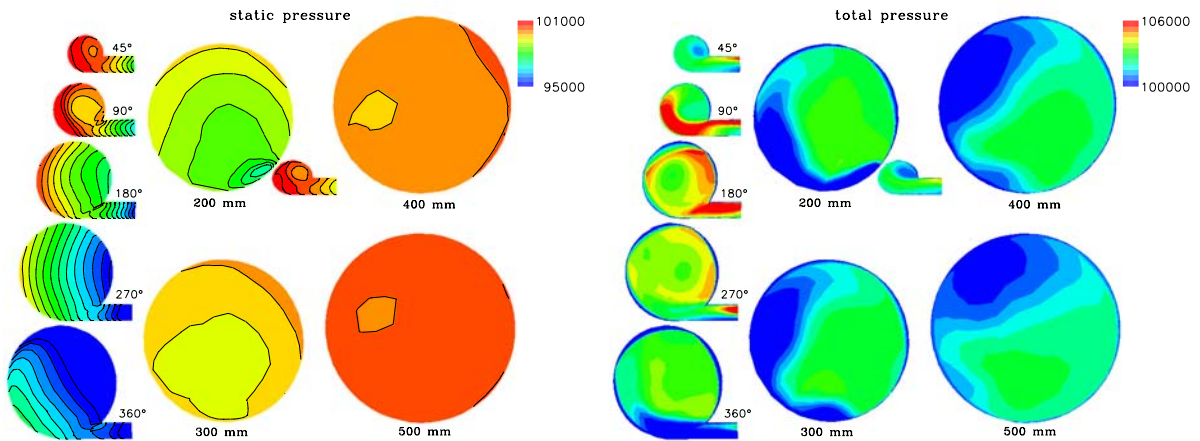


Figure 72. Static pressure (left) and total pressure (right) in the volute and exit cone at **high flow**.

Figures 67 - 69 show detailed distribution of the flow variables at the vaneless diffuser inlet at $r/r_2 = 1.01$ and outlet at $r/r_2 = 2.02$. The cylinder surfaces are transformed to a plane in such a manner that the view is from inside out and the impeller rotates from left to right. A full blade is located at 0° and a splitter at 25.7° .

Figure 67 shows the static pressure. In the hub-shroud direction the highest static pressure at the diffuser inlet is near the hub surface. This is due to the curvature of the flow as it turns from axial to radial direction in the impeller. This distribution evens out in the diffuser resulting in a fairly constant distribution in the hub-shroud direction at the diffuser outlet, which was also confirmed by the measurements (see chapter 4.4). In the circumferential direction the non-uniformity caused by the beginning of the exit cone and volute is clearly seen at the diffuser outlet and inlet. At the diffuser inlet the variation between the pressure and suction sides of the 14 blades is also easily seen. The static pressure is at the lowest on the suction side of the splitter blade near the shroud. The individual wakes are evened out very much in the diffuser.

Figure 68 shows the total pressure. At the diffuser inlet the backward facing step is seen as a low total pressure zone near the hub surface. The step causes the boundary layer on the hub wall to grow and the flow to funnel towards the shroud, which is seen as a high total pressure near the shroud at the diffuser outlet. This phenomenon is exaggerated in the calculation, since the measurements (chapter 4.4) show almost symmetric distribution of the total pressure in the hub-shroud direction at the diffuser outlet. At the diffuser inlet two maxima in the total pressure can be seen in the hub-shroud direction. The total pressure is high near the hub wall above the step, as the static pressure is high in that area. However, the total pressure is at the highest on the suction side of a splitter blade near the shroud. This is an indication of a high velocity in that area. The well-known behaviour of a radial impeller is that the relative velocity becomes almost zero or in some cases even negative near the suction side at the impeller exit (Japikse 1996). This results in a high absolute velocity as the local flow velocity becomes almost equal to the peripheral speed of the impeller.

Figure 69 shows the total-to-total isentropic efficiency. The step at the impeller exit and the boundary layer growth and separation due to the step is seen as low efficiency zones near the hub. At the diffuser inlet the efficiency is low on the blade suction side near the shroud, as expected. The efficiency on the suction side of the splitter blade seems to be slightly lower

than on the suction side of the full blade. However, at low flow another low efficiency zone develops onto the suction side of a full blade near the hub. It is uncertain whether the impeller really operates in this way or whether it is only a result of incorrect diffuser calculation and convergence problems. In the circumferential direction the effect of the individual blades can easily be seen, but it is interesting to note that the efficiency varies fairly little along the circumference. At high flow the efficiency decreases and at low flow increases along the circumference, but as already mentioned, the variation is small. The volute distorts the pressure distribution, but the total temperature distribution follows quite well the total pressure distribution, resulting in fairly average total-to-total efficiency along the circumference.

Contrary to the above result, Ayder et al. (1993) report a circumferentially constant tangential velocity distribution, which is an indication of circumferentially constant energy input of the impeller. Since the total pressure varies along the circumference, Ayder et al. (1993) conclude that the impeller efficiency varies along the circumference. However, the measurements of Hübl (1975) show a clear variation in the tangential velocity along the circumference. In the areas of low total pressure also the tangential velocity is reported to be lower. The measurements of Hagelstein et al. (2000) also show that the circumferential variation of the total pressure and total temperature follow each other quite well. These findings support the result of a rather constant impeller efficiency along the circumference.

6.4 Flow structure in the volute and the exit cone

The distribution of the static and total pressure inside the volute and the exit cone at different volume flows is presented in figures 70, 71 and 72. Five cross-sections of the volute channel, marked with the angle θ , are seen on the left and four cross sections of the exit cone, marked with the distance from the cone origin, on the right side of each figure. Also a small part of the very beginning of the volute channel is seen next to the cross-section of the exit cone at the 200 mm position. That part is not, however, correctly projected to the plane of the paper.

The static pressure variation is seen on the left. The radial pressure gradient caused by the through flow velocity and the circumferential curvature of the volute is clearly seen in the volute channel. The lowest static pressure is always close to the inner wall. The pressure

gradient caused by the swirl in the volute channel is far weaker. A few circular-like contours in the volute cross section are present in the beginning of the volute only.

In the straight exit cone the radial static pressure gradient naturally disappears. Thus the weak pressure gradient caused by the swirl (i.e. low static pressure in the middle and high static pressure close to the walls) can be observed. At high flow the disturbance of the sharp tongue is seen also in the static pressure distribution as a low-pressure zone.

The total pressure distribution is seen on the right. First, a comment must be made concerning the present quasi-steady calculation method. The wakes of the impeller full blades are distinct at the volute inlet, see figure 64. This is also seen in the total pressure distribution of the volute. For example a high-pressure wake enters the volute at $\theta = 45^\circ$ at low flow, at $\theta = 90^\circ$ and at $\theta = 180^\circ$ at the design flow and at $\theta = 90^\circ$, at $\theta = 180^\circ$ and at $\theta = 270^\circ$ at high flow. This fluid with high total pressure is wrapped around the volute cross section and carried through the volute by the swirl and through flow velocities. For this reason no exact comparison between the consecutive cross-sections can be made.

A low total pressure zone is always present in the middle of the volute channel. At the design flow the total pressure distribution seems to be more uniform than at low and high flows.

In the exit cone a very co-centric distribution of total pressure is seen at low flow. The low total pressure zone in the middle of the cone corresponds to the area of the highest unsteadiness observed in the internal flow visualisation. The low total pressure zone caused apparently by the separation at the tongue is seen right in the beginning of the small volute channel at low flow.

At the design flow the total pressure distribution in the exit cone is fairly constant apart from the low-pressure zone in the lower and left side of the cone. At high flow this area of low total pressure grows considerably and leads to unstable flow in the upper left part of the exit cone at the end of the cone. Also, the sharp tongue causes a small area of low total pressure behind the tongue at high flow. This is seen clearly in the bottom of the cross sections of 200 mm and 300 mm. However, it is interesting to note that the low total pressure zone originating from the tongue is far smaller than the other low total pressure zone in the exit cone.

The swirl velocity vectors in the volute and the exit cone are shown in figures 73 - 75. However, the vectors in the very beginning of the volute (next to the cross-section of the exit cone at the 200 mm position) should not be considered, since they are falsely projected. The same comment that was made for the total pressure applies for the swirl velocity as well. At certain cross sections a high swirl velocity wake enters the volute, which makes the vector plot to look a little uneven.

The swirl velocity vectors correspond relatively well with the swirl number presented in figure 60. At low flow the swirl for example at $\theta=180^\circ$ and at $\theta=360^\circ$ is stronger than at the design or high flows. A single vortex is observed in all cross-sections at all flow rates, which is typical for a volute with a tangential inlet (Hübl 1975, Ayder 1993, Hagelstein et al. 2000). In most cross-sections a forced vortex flow is seen. The deviation from it at low flow and in some cross-sections at the design and high flows is very likely due to the high and low swirl wakes that enter the volute. At high flow the disturbance of the tongue is seen in the exit cone as a reverse swirl next to the tongue in the 200 mm cross-section and as a locally reduced swirl in the bottom of the 300 mm cross-section.

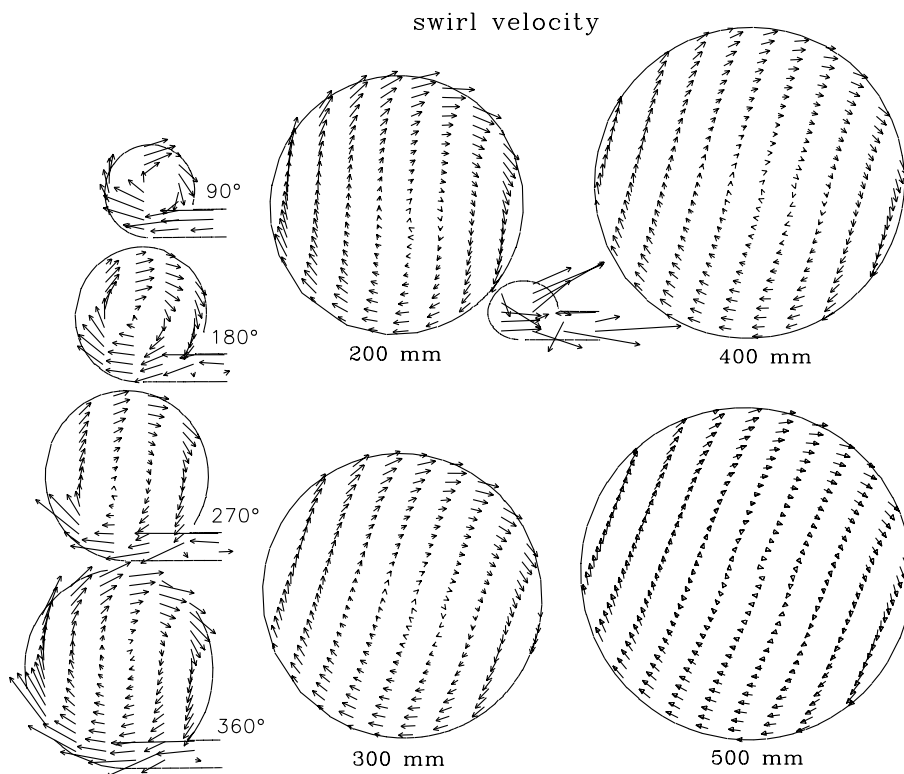


Figure 73. Swirl velocity vectors in the volute and exit cone at **low flow**.

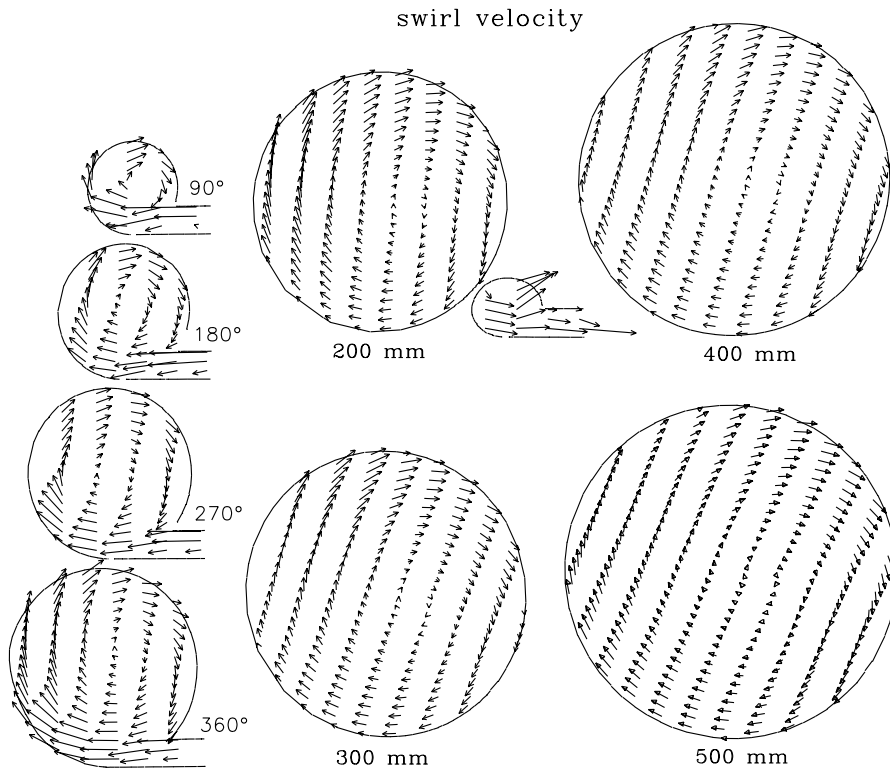


Figure 74. Swirl velocity vectors in the volute and exit cone at the **design flow**

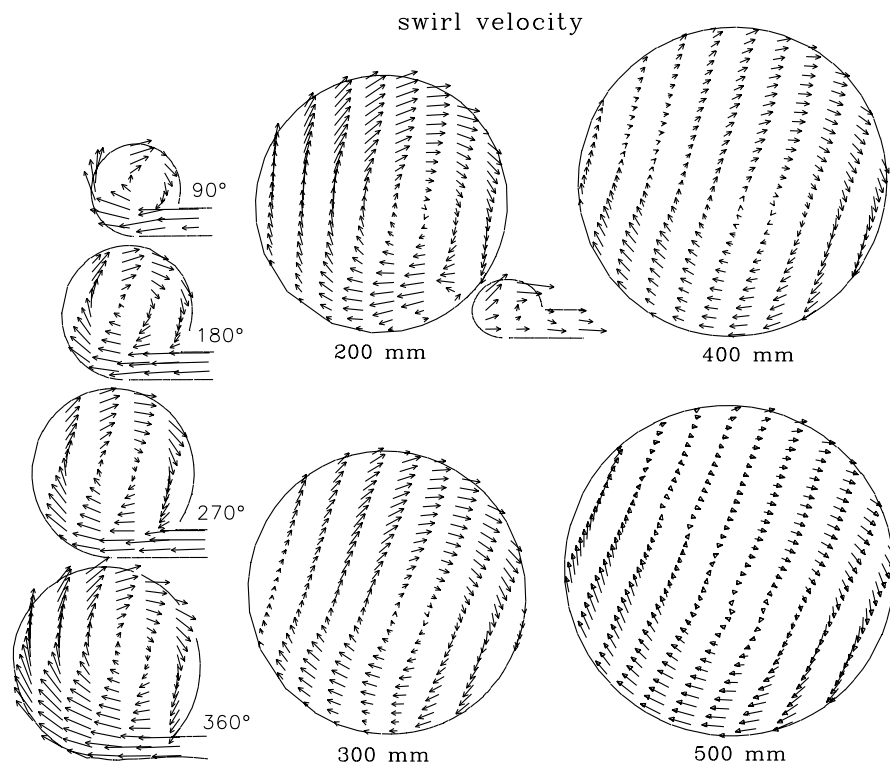


Figure 75. Swirl velocity vectors in the volute and exit cone at **high flow**.

6.5 Conclusions from the numerical analysis

The complete compressor with the circular volute (inlet pipe, full impeller, diffuser, volute and outlet pipe) was analysed using computational fluid dynamics (CFD). A fully three-dimensional viscous flow was solved using a Navier-Stokes solver, Finflo, developed at Helsinki University of Technology. The simulation was made at three different flow rates, and was based on the quasi-steady i.e. frozen rotor approach, in which the whole grid is stationary, but the co-ordinate axes rotate. Chien's $k-\varepsilon$ model was used to take account of the turbulence.

The modelling of the entire compressor required a large grid of about 5 000 000 computational cells, but even then the grid was too coarse in the boundary layers particularly in the diffuser, volute and exit cone. This led to over-predicted separation of the flow in the diffuser and convergence problems especially at low flow rate. The problems in the diffuser calculation reflected also to the volute, since the volute inflow condition is produced by the diffuser.

The overall pressure ratio of the compressor was very well predicted at high and design flows, but under-predicted at low flow due to the separation in the diffuser. The overall efficiency of the compressor was slightly over-predicted at high and design flows but correctly calculated at low flow.

The total pressure loss of the volute and exit cone combination (states 3→5) was the highest at low flow, the lowest at the design flow and moderate at high flow. The trend corresponds well with the measured one, although the level of the loss was slightly under-predicted. The static pressure rises in the volute and exit cone combination at all flow rates due to the diffusion in the exit cone. The static pressure rise was the highest at the design flow and the lowest at high flow. Again the predicted trend followed well the measured one, but the level of the pressure rise was slightly over-predicted. The small discrepancies were mainly due to the too coarse grid in the boundary layer and inaccurate volute inflow condition at low flow.

The modelling of the entire compressor allowed the non-uniformity caused by the volute to be examined. The circumferential distribution of static pressure at the diffuser inlet, diffuser outlet and in the volute showed increase at low flow, almost constant distribution at the design flow and decrease at high flow. No phase shift was seen in the static pressure distributions at

the diffuser inlet and outlet. The trend corresponded very well with the measured one. At low flow, however, the two-wave pattern observed in the measurements was not reproduced by the calculation, most likely because the quasi-steady method cannot account for time-dependent phenomena that determine the impeller response to the static pressure non-uniformity. At the design and high flows the level of the static pressure was also correct, but at low flow the pressure level at the diffuser outlet and in the volute was under-predicted due to the separation in the diffuser.

The calculated circumferential total pressure distribution at the diffuser inlet followed the trend of the static pressure distribution. Between the vaneless diffuser inlet and outlet, however, a phase shift was observed. A peak in the total pressure at the diffuser inlet was seen as a peak at the diffuser outlet at a bigger circumferential angle. The delay corresponds to the logarithmic flow paths of the fluid particles in the diffuser.

The isentropic total-to-total efficiency at the impeller outlet was seen to vary along the circumference only little, because the total temperature distribution followed that of the total pressure.

The flow structure in the volute channel consisted of a single vortex at all cross sections at all flow rates. Mainly a forced vortex was present. The observed deviations from the forced vortex flow were probably due to the high and low swirl velocity wakes that entered the volute at the different circumferential positions. In the static pressure distribution the effect of the through flow velocity was strong and the effect of the swirl velocity weak. Thus the lowest static pressure was close to the inner wall of the volute and only a few co-centric pressure contours were seen. The total pressure distribution showed a minimum in the middle of the volute channel. At high flow rate the disturbance of the tongue was seen in the beginning of the exit cone as a local reverse swirl and total pressure loss.

7 RADIAL FORCES

The non-uniform pressure distribution in the circumferential direction causes a radial force on the impeller as described in chapter 2. This radial force can cause blade vibrations or noise (Fatsis et al. 1997), or excessive bearing loading (Moore and Flathers 1998), and should thus be minimised. In this research compressor, however, the radial force is very small, as a result of the low operating pressure typical for a vacuum compressor. Anyhow, the existence of even a small radial force is an indication of non-uniformity of the flow, which in turn has a negative effect on the aerodynamic performance of the compressor. The aim of the radial force measurement in this case was to investigate the aerodynamic behaviour of the compressor through the force measurement.

7.1 Force measurement using magnetic bearings

7.1.1 Magnetic bearings as force measuring devices

The compressor is equipped with active magnetic bearings, which are controlled by an analogue control unit. The radial bearings are located at both ends of the electric motor. Each bearing consists of two pairs of pulling actuators. The bearing close to the compressor wheel is denoted with "d" and the one in the bottom end of the shaft with "n". The axial bearing is divided in two pulling magnetic actuators, which are located close to the radial ones. A sketch of the rotor is presented in figure 76.

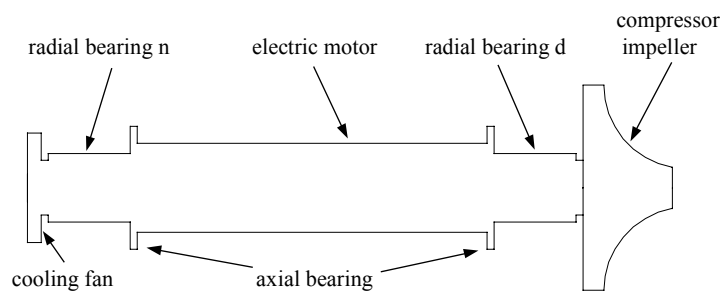


Figure 76. The rotor of the compressor and the locations of the bearings.

The force of the magnetic bearing depends almost linearly on the control current of the actuator pair, provided that the location of the shaft and the actuator (air gap) is unchanged. Thus the force F can be calculated from the following simple equation.

$$F = f(I - I_0) \quad (54)$$

Where I is the control current of the actuator and I_0 is the control current of the actuator at zero load. The function f is found by calibration. The currents of the bearings were measured and recorded by the control unit, which was connected to a personal computer via RS-232 serial cable in order to process and save the bearing data. Only time averaged values of the current could be saved with the analogue version of the control unit, thus the force information was updated every 2 - 3 seconds. This was accepted to be satisfactory, since the bearing currents or voltages are difficult to measure by any external device due to considerable electro-magnetic disturbances caused by the inverter, electric motor and the magnetic bearings themselves.

7.1.2 Calibration of the magnetic bearings

The co-ordinate axes of the radial bearings are shown in figure 77 on the left. The view is from above the volute. It is seen that the axes of the bearings are rotated 45° clockwise in comparison to the axes commonly used in volute analyses.

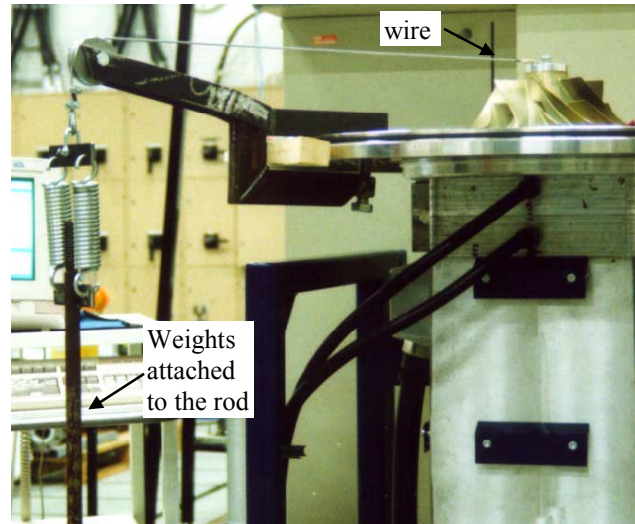
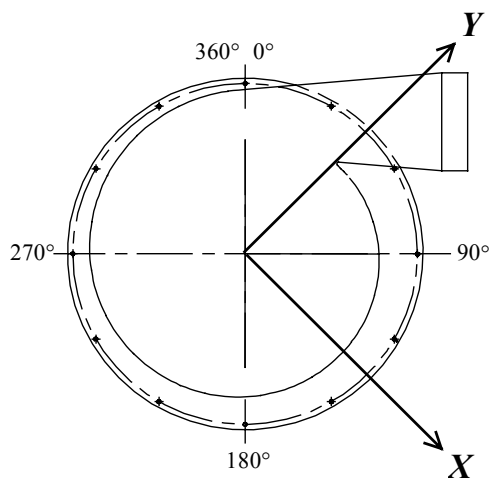


Figure 77. Direction of the co-ordinate axes in the magnetic bearing force measurement (left). The pulley mechanism used for the calibration of the magnetic bearings (right). Photo: Petri Sallinen / LUT

For the calibration the volute was removed and a wire was attached to the end of the shaft at the top of the impeller. Force was applied to the shaft by using a pulley mechanism and calibrated weights as shown in figure 77 on the right. The exact direction of the bearing co-ordinate axes was found by monitoring the bearing currents under a varying load while

moving the pulley. The direction of the X -axis was established, when the Y -current stayed constant regardless of the pull on the wire. This direction was marked on the compressor. The direction of the Y -axis was found in a similar way.

After the pulling directions were established, the calibration was carried out. In the beginning, the pulley mechanism was fitted to the direction of the positive X -axis. The zero load currents were recorded at first. Then weights were added one by one and the increasing currents were recorded each time until the maximum weight was reached. Then the weights were removed one by one and the decreasing current was recorded. When the load was wholly removed, the zero load currents were recorded again. At this point the pulley was quickly changed to the opposite direction and good care was taken as not to apply any force to the shaft during this operation. Then a similar pulling procedure was conducted to the negative direction of the X -axis. In this manner the hysteresis of the bearings could also be found out. Finally the same procedure was repeated for the Y -axis.

The free-body diagram of the shaft during the calibration is shown in figure 78. The force of the pull F_p on the bearings can be solved from simple equilibrium equations. The equilibrium of the forces is

$$F_n + F_d + F_p = 0 \quad (55)$$

The equilibrium of the moments is

$$-a \cdot F_d - (a + b_p) \cdot F_p = 0 \quad (56)$$

Solving for the bearing forces F_d and F_n gives

$$\begin{cases} F_d = \frac{(a + b_p)}{-a} \cdot F_p \\ F_n = \left(\frac{(a + b_p)}{a} - 1 \right) \cdot F_p \end{cases} \quad (57)$$

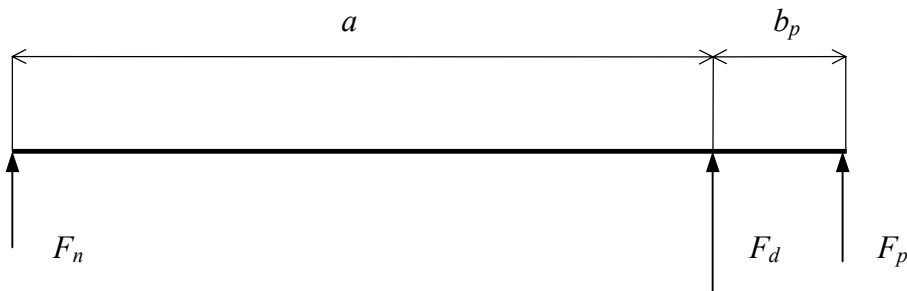


Figure 78. Free-body diagram of the rotor during the calibration pull.

The measured force of the d-bearing F_d versus the current difference $I - I_0$ is shown in figure 79. The zero load current I_0 was slightly different before and after the pull due to the hysteresis. For this reason the average value was used. In order to calculate the bearing force from the current measurement, a third degree polynomial function was fitted to the calibration results by the method of least squares. The calibration curves for the lower bearing n were found to be quite similar to those of the upper bearing d.

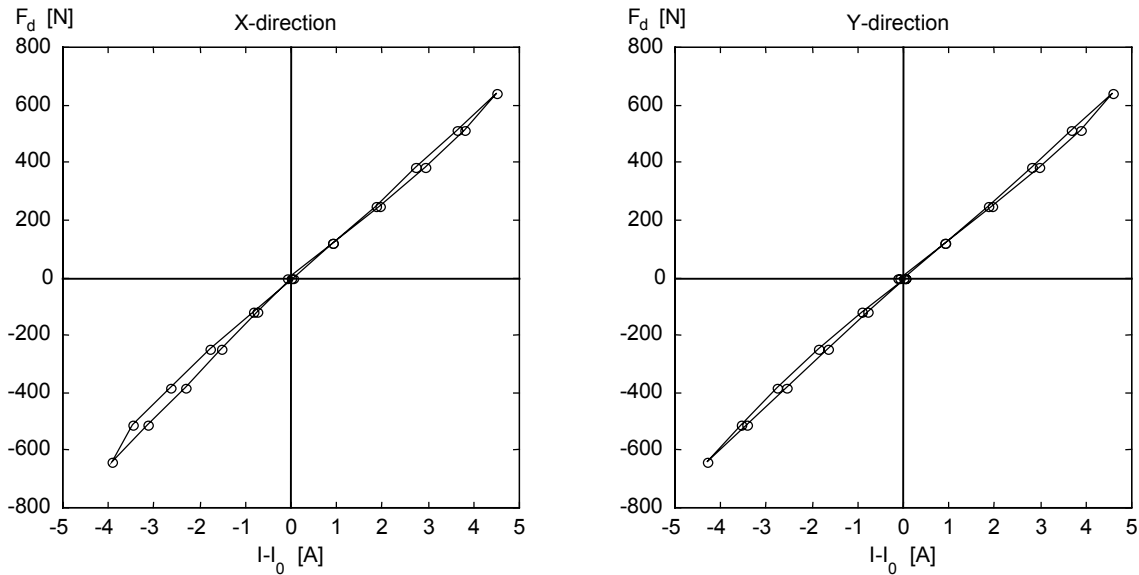


Figure 79. Calibration curves for the magnetic bearing d.

The slight difference in the increasing and decreasing currents is a sign of the hysteresis, which is the main source of inaccuracy in the bearing force measurement. Other possible sources of error include the warming of the electronics, which may cause drifting of the calibration, and thermal expansion of the bearings, their support and shaft, which causes small displacement of the parts in comparison to their locations during the calibration. For these reasons the error in the radial force measurement is $\pm (10 \text{ N} + 5\% \text{ of the measured value})$ according to the calibration experiences. When calculating the force on the compressor impeller, additional forces arising from the electric motor must be considered, too. This adds the uncertainty of the measurement as described in the next chapter.

7.1.3 Magnetic bearing force measurement

The compressor was let to run for about a half an hour to warm up before the bearing force measurement. Then the correct speed and volume flow were adjusted and the operation point

was allowed to stabilise. The measurement was begun at high volume flow close to the choking limit. At first the bearing current recording was turned on. Then the static pressures in the volute and in the diffuser were scanned. When all of the pressures were measured, the recording of the bearing currents was turned off. Then the compressor was throttled from the inlet and the same procedure was repeated for a smaller volume flow. In this way over 50 current measurements in each operating point could be made and the average bearing currents could be calculated, which increased accuracy. The measurement was carried out for all different volute geometries at two different speeds, the design rpm and 0.8 times the design rpm.

The radial force of the bearings can now be calculated using the calibration functions. The force on the impeller is computed on the basis of the rotor structure shown in figure 76. It is assumed that the force of the cooling fan is negligible since the fan is small and it exhausts in two opposite directions. The electric motor, however, may cause a force in radial direction and must therefore be considered. The free-body diagram of the rotor is shown in figure 80, in which F_m is the force of the motor and F_i is the radial force of the impeller. The force F_m is assumed to be in the centre of the motor.

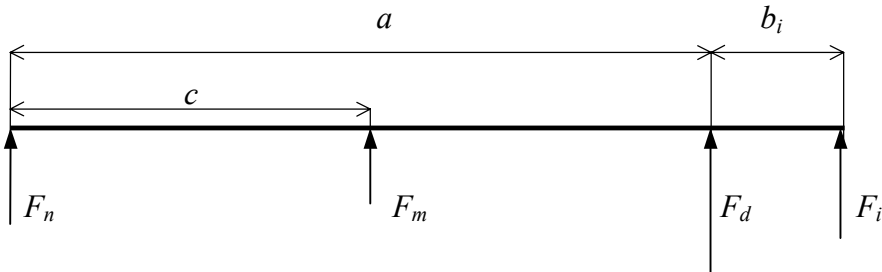


Figure 80. The free-body diagram of the rotor during the force measurement.

The equilibrium of the forces is

$$F_n + F_m + F_d + F_i = 0 \quad (58)$$

The equilibrium of the moments is

$$-c \cdot F_m - a \cdot F_d - (a + b_i) \cdot F_i = 0 \quad (59)$$

Solving for the unknown forces we get

$$\begin{cases} F_i = \frac{(a - c) \cdot F_d - c \cdot F_n}{(c - a - b_i)} \\ F_m = -F_n - F_d - F_i \end{cases} \quad (60)$$

In a simplified approach the force of the motor is assumed to be negligible. In this case the force on the impeller F_i can be calculated using the d-bearing measurement only with equation (61).

$$F_i = \frac{-a}{(a+b_i)} \cdot F_d \quad (61)$$

The force on the impeller in both X - and Y -direction is calculated using the above described methods. The direction of the force is then determined. The force vector is expressed as a complex number $F_{iX} + F_{iY}i$, see figure 81.

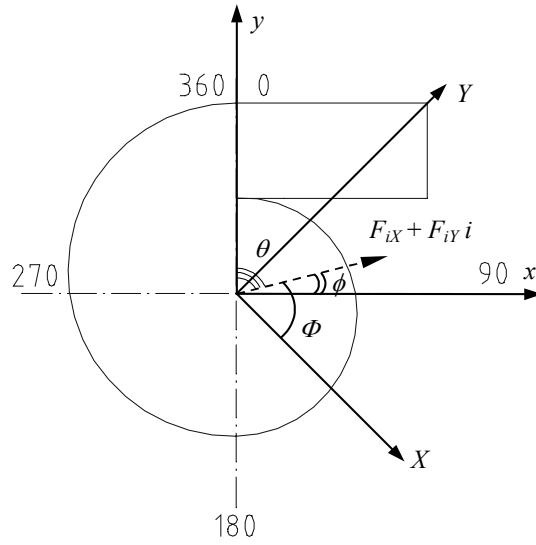


Figure 81. Force vector, co-ordinate axes and angles used in the radial force analyses.

The argument of the complex number $F_{iX} + F_{iY}i$ gives the direction Φ in the magnetic bearing X,Y co-ordinates.

$$\Phi = \arg(F_{iX} + F_{iY}i) = \tan^{-1}\left(\frac{F_{iY}}{F_{iX}}\right) \quad (62)$$

The absolute value of the complex number gives the length of the vector i.e. the magnitude of the force.

$$F_i = |F_{iX} + F_{iY}i| = \sqrt{F_{iX}^2 + F_{iY}^2} \quad (63)$$

The direction of the force ϕ in the volute co-ordinates x,y is found by subtraction

$$\phi = \Phi - 45^\circ \quad (64)$$

Finally the components of the impeller force in the volute x,y co-ordinates can be calculated

$$\begin{cases} F_{ix} = F_i \cos \phi \\ F_{iy} = F_i \sin \phi \end{cases} \quad (65)$$

The direction of the force of the motor is determined in a similar manner. The results of the radial force analyses are presented using the angle of the force θ , $\theta \in [0, 360]$, which is counted in the direction of the rotation starting from the exit cone origin, see figure 81.

7.1.4 Results of the magnetic bearing measurements

The results of the bearing force measurements with the different volutes at the design speed and at 0.8 speed are shown in figures 82 and 83. The impeller force in figure 82 is calculated according to the simplified method, equation (61), in which the force of the electric motor is not taken into account. Figure 83 shows the force of the motor and the impeller force calculated using equation (60), in which the force of the motor is accounted for. It is seen that the force of the motor is considerably big in comparison to the impeller force. According to the investigations by the motor manufacturer, the magnitude and direction of the radial force of the motor should stay rather constant at a given speed regardless of the volume flow. Figure 83 shows that the magnitude of the motor force is fairly constant increasing only slightly towards high flow, but the direction of the motor force varies somewhat. Most likely the assumptions in equation (60) are so rough that the motor force calculated according to it includes also a small amount of impeller force. However, the measured impeller force behaves quite similarly regardless of the calculation method, so the motor force does not ruin the impeller force measurement. Close to the design flow, however, the impeller force is so small that reliable bearing force measurement is almost impossible due to the motor force and other inaccuracies.

The radial force of the impeller is seen to be the greatest at the choke limit, the smallest close to the design flow and moderate at low flow. At the 0.8 speed the minimum of the force is at slightly smaller flow than at the design speed, as suggested already by the pressure measurements. An interesting observation is that the force increase at low flow is quite mild, whereas the increase at high flow is very rapid. The conclusion is that in the test compressor the pressure non-uniformity and negative effects related to it are strong especially at high flow. This was observed also in the static pressure distribution of the volute.

The direction of the force can be seen from the polar plots in figures 82 and 83. It behaves in a logical way, when compared to the static pressure measurements of the volute. The direction of the force is about 360° at choke. The force vector then turns counter-clockwise, i.e. opposite to the direction of the rotation of the impeller, as the flow is decreased, and points approximately to 90° at stall. Moore and Flathers (1998) report a similar trend, but the directions in their experiment are turned about 120° more to the direction of rotation.

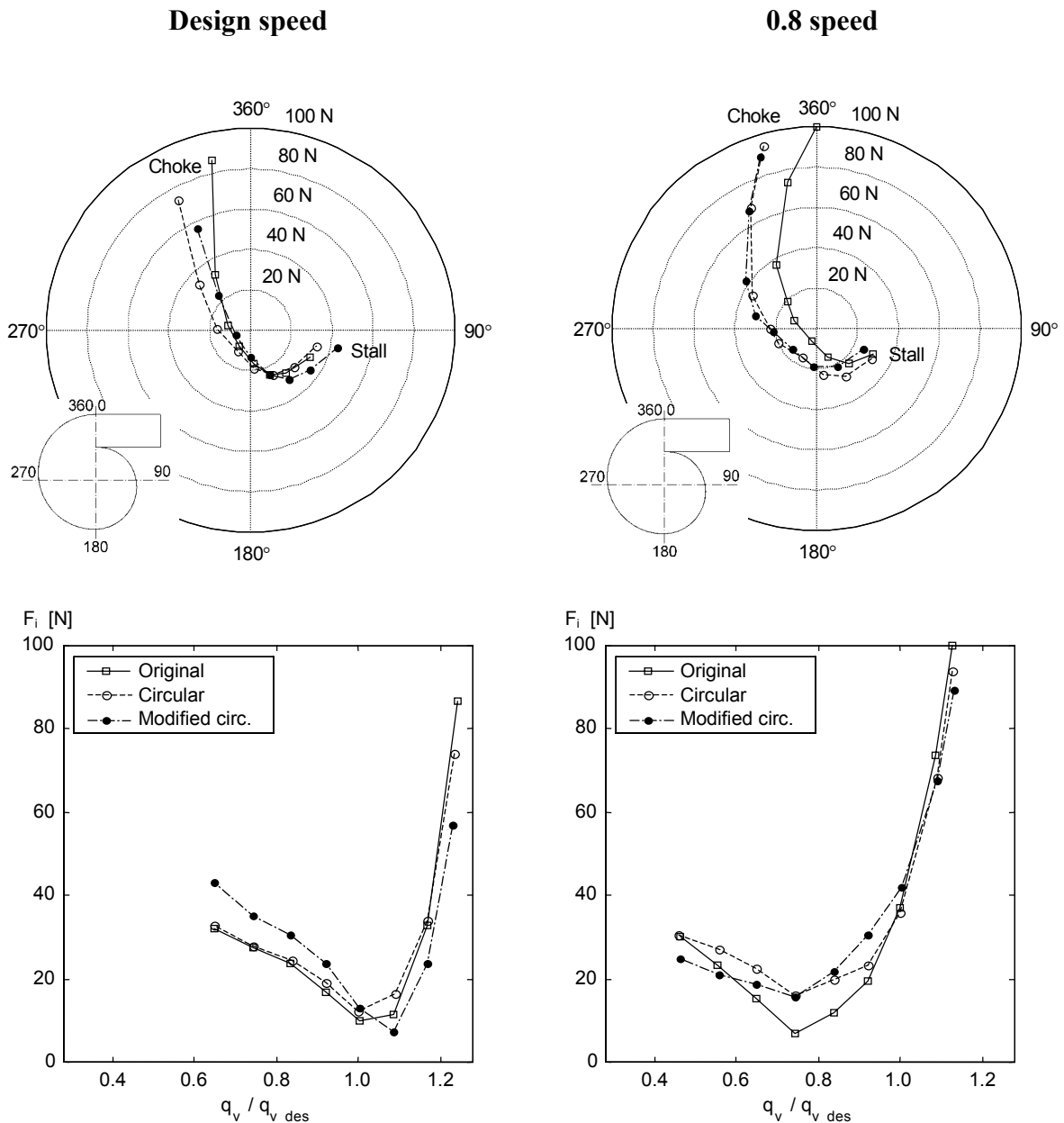


Figure 82. Comparison of the measured radial force with the different volutes using the simplified method, equation (61), in which the force of the motor is neglected.

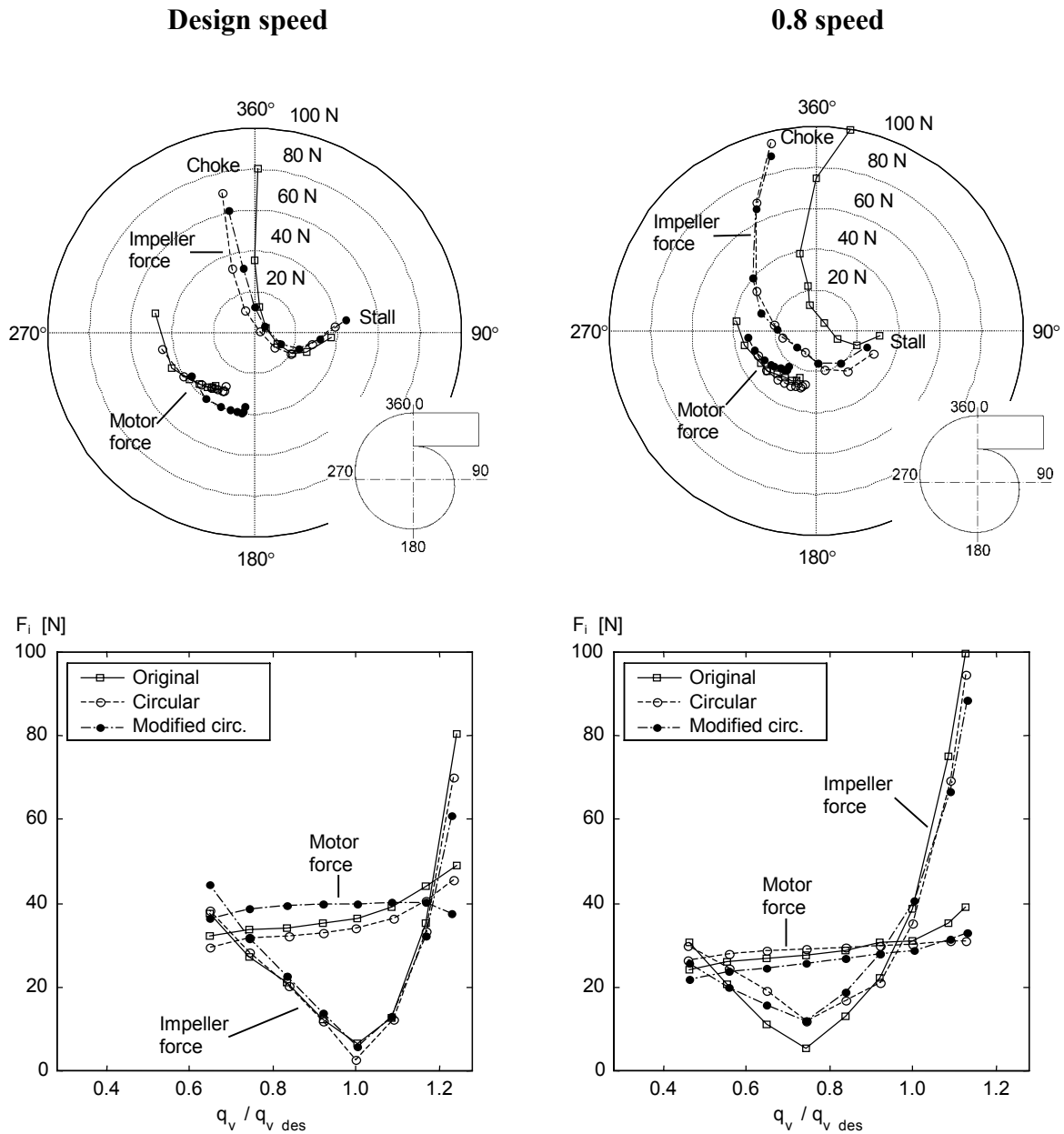


Figure 83. Comparison of the measured radial force with the different volutes calculated using equation (60), which takes the force of the motor into account. The force of the electric motor is shown as well.

Some, although small, differences are seen between the impeller forces measured with the different volutes. At high flow the original volute seems to cause the strongest radial force and the modified circular the weakest. This indicates that the modified circular volute causes the least non-uniformity at choke. At low flow at the design speed the modified circular volute causes the strongest force. Overall it looks as if the behaviour of the modified circular volute as a function of the volume flow was the most symmetric.

At the 0.8 speed the direction of the radial force with the original volute points more into the direction of the rotation. No exact reason can be given for this phenomenon.

7.2 Impeller force from the pressure measurements

An estimate for the radial force on the impeller can also be calculated on the basis of the diffuser static pressure measurements. Since the static pressure distribution at the inlet of the diffuser i.e. at the exit of the impeller is known, the force caused by the pressure non-uniformity can be calculated. This method has been applied to centrifugal pumps for example by Wesche (1987) and Iversen et al. (1960). According to Fatsis et al. (1997) the radial force of a centrifugal compressor can quite accurately be determined from the static pressure distribution at the impeller exit, if the impeller blades have high backsweep. If the impeller has got radially ending blades, the pressure measurement alone is not adequate, since the radial momentum contributes to the radial force to a great extent. In the present test compressor the impeller blades have 30° backsweep, whereas Fatsis used an impeller with 40° backsweep. Thus the radial force can be determined from the pressure distribution, if not correctly, at least with a reasonable accuracy.

The circumference around the impeller is divided into eight equally large sectors. The static pressure in each sector n is assumed to have a constant measured value p_n . The components of the pressure force in the volute x,y co-ordinates in each sector are

$$\begin{cases} F_{x_n} = -\cos \phi \frac{b_2 \pi d_2}{8} p_n \\ F_{y_n} = -\sin \phi \frac{b_2 \pi d_2}{8} p_n \end{cases} \quad (66)$$

and the total force acting on the impeller is

$$\begin{cases} F_{i_x} = \sum_{n=1}^8 F_{x_n} \\ F_{i_y} = \sum_{n=1}^8 F_{y_n} \end{cases} \quad (67)$$

Figure 84 shows the radial forces calculated from the measured static pressure distribution with the different volutes at the design speed and at 0.8 speed. Only small differences are observed between the volutes. The differences are, however, quite similar to those seen from the bearing measurements. At choke the modified circular volute causes the smallest radial force and at stall at the design speed the modified circular volute causes the strongest force. At both speeds the direction of the force points more into the direction of the rotation with the original volute than with the other volutes.

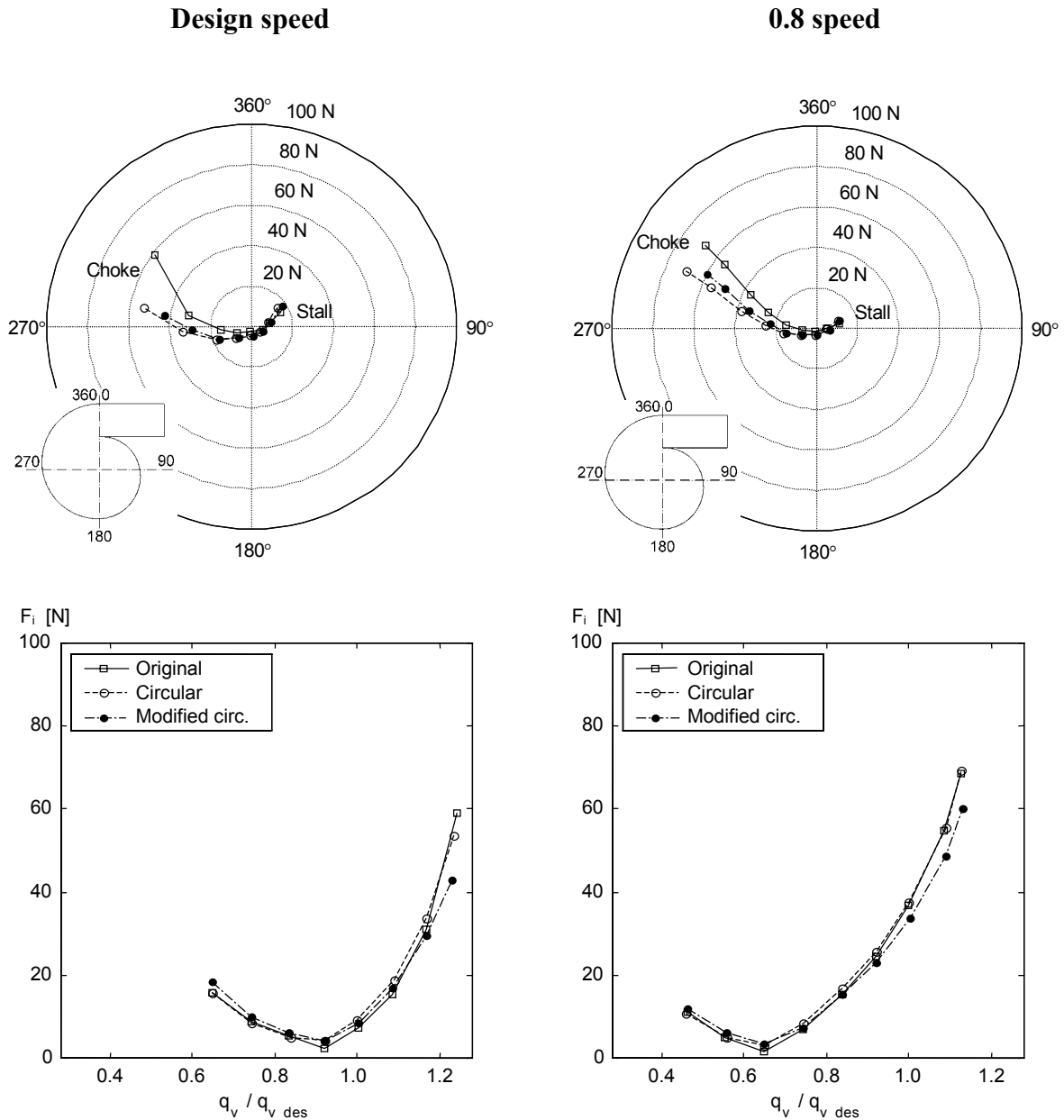


Figure 84. Radial force according to the pressure measurement with the different volutes.

7.3 Analysis of the force measurement and comparison of different methods

In order to compare the force measurements with each other and especially with the results gained by other researchers, the effect of the compressor outlet pressure and impeller dimensions is reduced out using the non-dimensional radial force coefficient K_r ,

$$K_r = \frac{F_r}{p_{t\ out} d_2 b_2} \quad (68)$$

which is derived from equation (21).

Figure 85 shows the K_r for the modified circular volute calculated from the bearing and pressure measurements at two different speeds. For the determination of the force from the bearing measurements, equation (60), which takes the motor force into account, is used. Reasonable agreement is seen between the methods. Especially at 0.8 speed the agreement is good. The minimum of the force is located at slightly lower flow when it is calculated from the pressure measurements. Also the variation of the radial force as a function of the volume flow is more gradual when the pressure measurements are used. At both low and high flows the pressure measurements yield to a weaker radial force than the bearing measurements. Perhaps the most distinct difference is seen in the direction of the forces, see figures 83 and 84. The force vector points considerably more into the direction of the rotation when it is determined from the bearing measurements. The differences can be explained by two reasons: Firstly, the bearing measurement includes numerous inaccuracies. Especially close to the minimum the force is so small that accuracy is questionable. Secondly, the impeller outlet static pressure measurement alone cannot account for all of the factors contributing to the radial force.

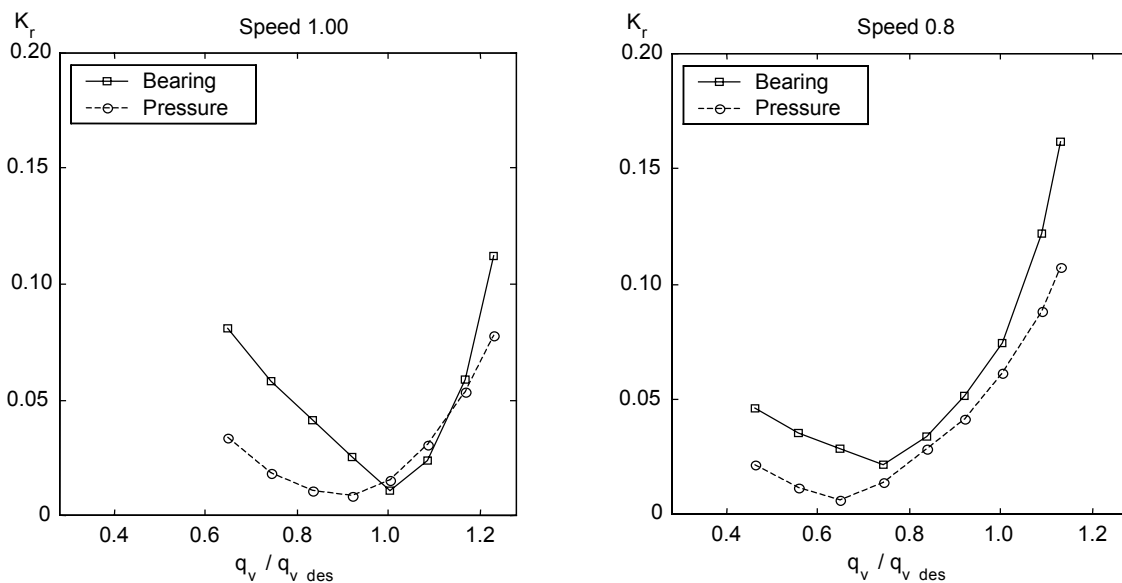


Figure 85. Radial force coefficient with the modified circular volute calculated from the bearing and pressure measurements.

Moore and Flathers (1998) report a somewhat different behaviour of the radial force as a function of the volume flow, see figure 86. One can compare the trend, but not so much the absolute values in figures 86 and 88, since the compressor size and outlet pressure was far greater than in the present measurements and English units were used to determine the

dimensionless coefficients by Moore and Flathers (1998). In their measurements the radial force of the compressor was strongest at stall and increased only little from the minimum at choke. That kind of behaviour can only partially be explained by the fact that they were investigating an overpressure compressor, in which the outlet pressure increases as the flow decreases. The higher outlet pressure causes a stronger force even if the non-uniformity was the same, see equation (21). However, the non-dimensional radial force coefficient K_r reported by Moore and Flathers (1998) reduces out the effect of the varying outlet pressure and shows also high force at stall and relatively weak force at choke. Perhaps the compressor was not run all the way into the choke by Moore and Flathers, or then the differences in the compressor construction (inlet volute, inlet guide vanes and shrouded mixed flow impeller) explain the different behaviour.

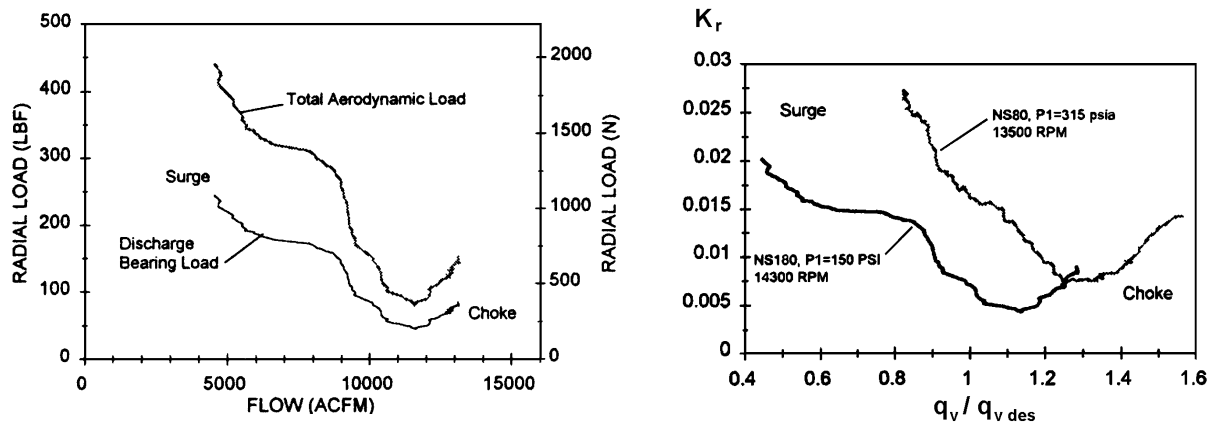


Figure 86. Radial force (left) and radial force coefficient K_r (right) reported by Moore and Flathers (1998).

The effect of the rotational speed on the radial force has been addressed by Moore and Flathers (1998). In order to reduce out the effect of the speed on the flow, the results are plotted against the flow coefficient ϕ as suggested by Moore and Flathers.

$$\phi = \frac{q_{v1}}{d_2^3 N} \quad (69)$$

where q_{v1} is the inlet volume flow, d_2 in the impeller outlet diameter and N the rotational speed. Figure 87 shows the results of the present force measurements with the modified circular volute against the flow coefficient at the design and 0.8 speeds. The results of Moore and Flathers are shown in figure 88 for comparison. The present measurements, see figure 87, show that the speed indeed affects the force. At low speed the minimum of the force is located at a smaller flow coefficient. At low speed also the force versus flow coefficient varies more gradually than at the design speed. However, the maximum force at choke is stronger at low

speed. This is due to the fact that at low speed the maximum attainable flow coefficient is greater than at the design speed. At a given flow coefficient the force is stronger at the design speed apart from the area close to the minimum force. The results of Moore and Flathers show a partially similar trend. In their experiments the lower speed results always in a smaller force. The variation in the slope of the force vs. flow coefficient was not observed by Moore and Flathers.

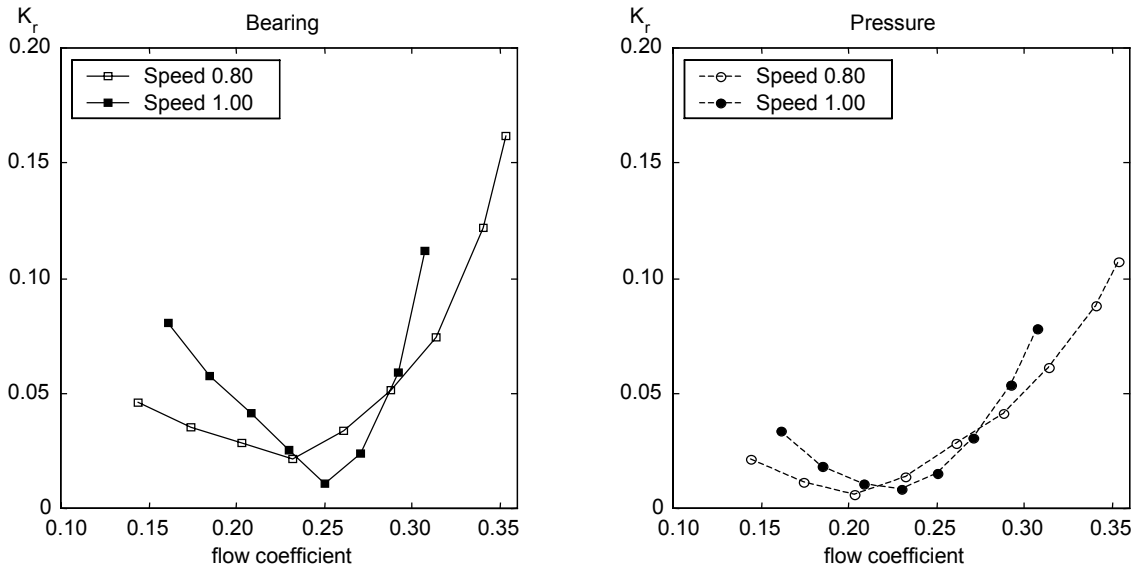


Figure 87. Radial force coefficient as a function of the flow coefficient with the modified circular volute calculated from the bearing and pressure measurements.

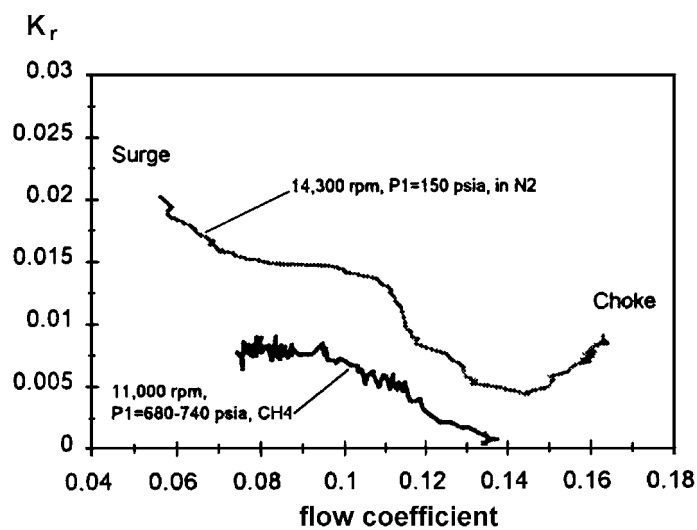


Figure 88. Radial force coefficient K_r against the flow coefficient at two different speeds reported by Moore and Flathers (1998).

7.4 Conclusions from the radial force measurements

The radial force acting on the impeller was measured using magnetic bearings. In addition, the radial force was estimated using the static pressure distribution measured at the impeller outlet.

The impeller force according to the bearing measurements was the highest at choke, the lowest at the design flow and moderate at stall. However, the exact location of the minimum force was difficult to establish, since the force around the design flow was below the measurement uncertainty. At low flow the force increase was quite mild, whereas the increase at high flow was rapid. Thus, the pressure non-uniformity and force related to it was strong especially at high flow. The force caused by the modified circular volute was weaker at choke and more symmetric as a function of the volume flow than the force caused by the other volutes.

The radial force determined from the pressure measurements was only slightly different from the force obtained from the bearing measurements. The magnitude of the force was a little smaller, the minimum of the force was at slightly lower flow rate and the variation of the force as a function of the flow rate was more gradual, when the force was calculated from the pressure distribution. The biggest difference was in the direction of the force. The force vector pointed more against the direction of the rotation when it was determined from the pressure measurements. The trend observed and conclusions made from the bearing force measurements apply also for the pressure force measurements.

The rotational speed was seen to affect the force somewhat. At 0.8 speed the minimum of the force was at a smaller flow rate and also at a smaller flow coefficient than at the design speed. Also the variation of the force as a function of the flow rate and flow coefficient was more gradual at lower speed.

8 CONCLUSION

A radial compressor with three different volutes was analysed experimentally. The compressor was first equipped with the original volute, the cross-section of which was a combination of a rectangle and semi-circle. Next a new volute with a fully circular cross-section was installed. Finally, the circular volute was modified by rounding the tongue and smoothing the tongue area. In addition, the entire compressor with the circular volute was analysed numerically. The detailed conclusions from the experimental and numerical as well as from the radial force analyses are presented in chapters 4.7, 6.5 and 7.4. and thus only a brief overall conclusion is presented here.

Only small differences in the performance of the compressor with the different volutes were observed. According to the overall efficiency measurements the compressor performed equally with each volute at the design point. The biggest differences were observed at low speeds and high flow rates, i.e. when the flow enters the volute most radially. In this operating regime the efficiency of the compressor with the modified circular volute was about two percentage points higher than with the other volutes.

The total pressure loss and static pressure recovery coefficients were used to judge the performance of the volutes and the exit cones. The measured total pressure loss in each volute and exit cone was seen to be the highest at low flow, the lowest at the design flow and moderate at high flow. A similar trend was observed also in the numerical analysis of the compressor with the circular volute. When comparing the measured pressure loss of the different volutes and exit cones with each other, the modified circular volute was seen to perform best at high and design flows, while the original volute had the smallest loss at low flow.

At off-design conditions each volute produced a non-uniform static pressure distribution, which was observed also at the impeller exit. The distortion was moderate at stall, the smallest close to the design flow and the strongest at choke. Even at the design flow the beginning of the exit cone, which was connected to the diffuser through the tongue gap, caused some pressure distortion. A trend similar to that of the pressure distortion was observed in the measured radial force with each volute. The force caused by the modified circular volute was

weaker at choke and more symmetric as a function of the volume flow than the force caused by the other volutes.

By rough generalisation the three volutes can be put in the following order with the first having the best performance:

1. modified circular volute
2. original volute
3. circular volute.

The results show that the fully circular cross-section is beneficial when the radial velocity at the volute inlet is high, i.e. when the swirl in the volute is strong. However, the through flow velocity was higher than the swirl velocity at all the operating points that were chosen for the detailed measurements. Thus the optimal design of the volute and exit cone in relation to the through flow velocity was a more important factor for the performance than the optimal cross-sectional shape of the volute. In particular, the rounding and smoothening of the tongue improved the performance of the circular volute at off-design conditions.

REFERENCES

Agostinelli, A., Nobles, D. and Mockrigde, C. R. 1960. An Experimental Investigation of Radial Thrust in Centrifugal Pumps. Transactions of the ASME, Journal of Engineering for Power. Vol. 82, No. 2, April 1960, pp. 120 - 126.

Antila, M., Lantto, E., Saari, J., Esa, H., Lindgren, O. and Säily, K. 1996. Design of Water Treatment Compressors Equipped with Active Magnetic Bearings. Fifth International Symposium on Magnetic Bearings, Kanazawa, Japan, 28. - 30.8. 1996. Department of electrical and computer engineering, Kanazawa University, Japan. pp. 389 - 394.

ASME PTC 10. 1965. ASME Power Test codes, Compressors and Exhausters. The American Society of Mechanical Engineers. 83 p.

Ayder, E. 1993. Experimental and Numerical Analysis of the Flow in Centrifugal Compressor and Pump Volute. Universiteit Gent, Fakulteit van de Toegepaste Wetenschappen / Von Karman Institute for Fluid Dynamics. 390 p. Diss.

Ayder, E. and Van den Braembussche, R. 1991. Experimental Study of the Swirling Flow in the Internal Volute of a Centrifugal Compressor. ASME Paper No. 91-GT-7.

Ayder, E. and Van den Braembussche, R. 1994. Numerical Analysis of the Three-Dimensional Swirling Flow in Centrifugal Compressor Volute. Transactions of the ASME, Journal of Turbomachinery. Vol. 116, July 1994, pp. 462 - 468.

Ayder, E., Van den Braembussche, R. and Brasz, J. J. 1993. Experimental and Theoretical Analysis of the Flow in a Centrifugal Compressor Volute. Transactions of the ASME, Journal of Turbomachinery. Vol. 115, July 1993, pp. 582 - 589.

Backman, J. 1996. On the Reversed Brayton Cycle with High Speed Machinery. Lappeenranta, Lappeenranta University of Technology, Research papers 56. 103 p. Diss.

Baldwin, B. and Lomax, H. 1978. Thin Layer Approximation and Algebraic Model for Separated Turbulent Flows. AIAA Paper 78-275.

Baun, D. O. and Flack, R. D. 1999. A Plexiglas Research Pump with Calibrated Magnetic Bearings / Load Cells for Radial and Axial Hydraulic Force Measurement. Transactions of the ASME, Journal of Fluids Engineering. Vol. 121, March 1999, pp. 126 - 132.

Bowerman, R. D. and Acosta, A. J. 1957. Effect of the Volute on Performance of a Centrifugal-Pump Impeller. Transactions of the ASME. Vol. 79, No. 5, July 1957, pp. 1057 - 1069.

Brown, W. B. and Bradshaw, G. R. 1947. Design and Performance of Family of Diffusing Scrolls with Mixed-Flow Impeller and Vaneless Diffuser. Cleveland, Ohio, National Advisory Committee for Aeronautics, Technical Report NACA-TR-936.

Chien, K.-Y. 1982. Predictions of Channel and Boundary Layer Flows with a Low Reynolds Number Turbulence Model. AIAA Journal. Vol. 20, Jan. 1982, pp. 33 - 38.

Copley, D. M., Worster, R. C. and Zanker, K. J. 1962. The Flow in Pump Volutes and Its Effect on Performance. Presented at the 8th Conference on Hydromechanics, Cranfield, April 9th - 11th, 1962. Paper No. BHRA SP 724.

Crowder, J. P. 1989. Tufts. In: Yang, W.-J. (ed.) Handbook of Flow Visualization. New York, Hemisphere Publishing Corporation. pp. 125 - 175.

Cui, M. M. 2000. Comparative Study of Vaneless and Vaned Diffusers in a Transonic Centrifugal Compressor with Real Gas. ASME Paper No. 2000-GT-450.

Dilin, P., Sakai, T., Wilson, M. and Whitfield, A. 1998. A Computational and Experimental Evaluation of the Performance of a Centrifugal Fan Volute. Proceedings of the Institution of Mechanical Engineers, Part A: Journal of Power and Energy. Vol. 212, No. 4, pp. 235 - 246.

DIN 1952. 1971. Durchflußmessung mit genormten Düsen, Blenden und Venturidüsen. Deutsches Institut für Normung e.V. 14 p.

Dong, R., Chu, S. and Katz, J. 1997. Effect of Modification to Tongue and Impeller Geometry on Unsteady Flow, Pressure Fluctuations and Noise in a Centrifugal Pump. Transactions of the ASME, Journal of Turbomachinery. Vol. 119, July 1997, pp. 506 - 515.

Eck, B. 1957. Ventilatoren. Dritte erweiterte Auflage, Berlin, Springer Verlag. 493 p.

Fahua, G., Engeda, A., Cave, M. and Di Liberti, J-L. 2000. A Numerical Investigation on the Volute/Diffuser Interaction Due to the Axial Distortion at Impeller Exit. In: Engeda, A. et al. (eds). Challenges and Goals in Industrial and Pipeline Compressors. ASME, PID-Vol. 5, pp. 71 - 80.

Fatsis, A., Pierret, S. and Van den Braembussche, R. 1997. Three-Dimensional Unsteady Flow and Forces in Centrifugal Impellers With Circumferential Distortion of the Outlet Static Pressure. Transactions of the ASME, Journal of Turbomachinery. Vol. 119, Jan. 1997, pp. 94 - 102.

Flathers, M. B. and Bache, G. E. 1996. Aerodynamically Induced Radial Forces in a Centrifugal Gas Compressor - Part 2: Computational Investigation. ASME Paper No. 96-GT-352.

Gupta, A. K., Lilley, D. G. and Syred, N. 1984. Swirl Flows. Turnbridge Wells, Kent, Abacus Press. 475 p.

Hagelstein, D., Hillewaert, K., Van den Braembussche, R., Engeda, A., Keiper, R. and Rautenberg, M. 2000. Experimental and Numerical Investigation of the Flow in a Centrifugal Compressor Volute. Transactions of the ASME, Journal of Turbomachinery. Vol. 122, Jan. 2000, pp. 28 - 31.

Hagelstein, D., Van den Braembussche, R., Keiper, R. and Rautenberg, M. 1997. Experimental Investigation of the Circumferential Static Pressure Distortion in Centrifugal Compressor Stages. ASME Paper No. 97-GT-50.

Hillewaert, K. and Van den Braembussche, R. 1999. Numerical Simulation of Impeller - Volute Interaction in Centrifugal Compressors. Transactions of the ASME, Journal of Turbomachinery. Vol. 121, July 1999, pp. 603 - 608.

Hosangadi, A., Ahuja, V. and Lee, Y. T. 2000. Simulations of Transonic Diffuser-Volute System Using Hybrid Unstructured Grid. In: Engeda, A. et al. (eds). Challenges and Goals in Industrial and Pipeline Compressors. ASME, PID-Vol. 5, pp. 55 - 62.

Hübl, H. P. 1975. Beitrag zur Berechnung des Spiralgehäuses von Radialverdichtern und Vorherbestimmung seines Betriebsverhaltens. Wien, Technische Universität Wien, Mitteilungen des Institutes für Dampf und Gasturbinen, Nr. 7. 122 p.

ISO 5389. 1992. Turbocompressors - Performance test code. International Standardization Organization. 172 p.

Iversen, H. W., Rolling, R. E. and Carlson, J. J. 1960. Volute Pressure Distribution, Radial Force on the Impeller, and Volute Mixing Losses of a Radial Flow Centrifugal Pump. Transactions of the ASME, Journal of Engineering for Power. Vol. 82, No. 2, April 1960, pp. 136 - 144.

Japikse, D. 1982. Advanced diffusion levels in turbocharger compressors and component matching. Proceedings of the first International Conference on Turbocharging and Turbochargers, 26 - 28 April, 1982. London, IMechE. pp. 143 - 155.

Japikse, D. 1984. Turbomachinery Diffuser Design Technology. Vermont, USA, Concepts ETI Inc. 330 p.

Japikse, D. 1996. Centrifugal Compressor Design and Performance. Vermont, USA, Concepts ETI Inc. 452 p.

Kaurinkoski, P. and Hellsten, A. 1998. FINFLO: the Parallel Multi-Block Flow Solver. Helsinki, Helsinki University of Technology, Laboratory of Aerodynamics, Report No. A-17. 43 p.

Larjola, J. 1988. Radiaalikompressorin suunnittelun perusteet (in Finnish), (Centrifugal Compressors, the Fundamentals of Design). Lappeenranta, Lappeenranta University of Technology, Department of Energy Technology, Research Report EN B-61. 57 p.

Lee, Y. and Bein, T. W. 1997. Three-Dimensional Numerical Simulation of a Compressor Volute. ASME Paper No. FEDSM97-3444.

Lendorff, B. and Meienberg, H. 1944. Detail-Entwicklung im Bau von Turboverdichtern. Escher Wyss Mitteilungen. Vol. 17/18, 1944/45, pp. 60 - 67.

Lipski, W. 1979. The Influence of Shape and Location of the Tongue of Spiral Casing on the Performance of Single-Stage Radial Pumps. In: Proceedings of the Sixth Conference on Fluid Machinery, Vol. 2. Budapest, Akademiai Kiado, pp. 673 - 682.

Lombard, C., Bardina, J., Venkatapathy, E. and Olinger, J. 1983. Multi-Dimensional Formulation of CSCM - An Upwind Flux Difference Eigenvector Split Method for the Compressible Navier-Stokes Equations. In: 6th AIAA Computational Fluid Dynamics Conference, Danvers, Massachusetts, July 1983. pp. 649-664. AIAA Paper 83-1895-CP.

Menter, F. R. 1994. Two-Equation Eddy-Viscosity Turbulence Models for Engineering Applications. AIAA Journal. Vol. 32, No. 8, Aug. 1994, pp.1598 - 1605.

Mishina, I. and Gyobu, I. 1978. Performance Investigations of Large Capacity Centrifugal Compressors. ASME Paper No. 78-GT-3.

Moore, C. A. and Kline, S. J. 1958. Some Effects of Vanes and of Turbulence in Two-Dimensional Wide-Angle Subsonic Diffusers. Washington, National Advisory Committee for Aeronautics, Technical Note NACA TN 4080. 139 p.

Moore, J. J. and Flathers, M. B. 1998. Aerodynamically Induced Radial Forces in a Centrifugal Gas Compressor: Part 1 - Experimental Measurement. Transactions of the ASME, Journal of Engineering for Gas Turbines and Power. Vol. 120, April 1998, pp. 383 - 390.

Pitkänen, H., Esa, H., Sallinen, P., Larjola, J., Heiska, H. and Siikonen, T. 1999. Time-Accurate CFD Analysis of a Centrifugal Compressor. In: Proceedings of the Fourth International Symposium on Experimental and Computational Aerothermodynamics of Internal Flows. Dresden, Aug. 31 - Sep. 2, 1999. Vol. 2, pp. 130 - 139.

Qi, D. T., Pomfret, M. J. and Lam, K. 1996. A new approach to the design of fan volutes. Proceedings of the Institution of Mechanical Engineers, Part C: Journal of Mechanical Engineering Science. Vol. 210, pp. 287 - 294.

Rautaheimo, P., Salminen, E. and Siikonen T. 1999. Numerical Simulation of the Flow in the NASA Low-Speed Centrifugal Compressor. Helsinki, Helsinki University of Technology, Laboratory of Applied Thermodynamics, Report No. 119. 61 p.

Reunanen, A., Pitkänen, H., Siikonen, T., Heiska, H., Larjola, J., Esa, H. and Sallinen, P. 2000. Computational and Experimental Comparison of Different Volute Geometries in a Radial Compressor. ASME Paper No. 2000-GT-469.

Roe, P. 1981. Approximate Riemann Solvers, Parameter Vectors and Difference Schemes. Journal of Computational Physics. Vol. 43, pp. 357 - 372.

Sallinen, P. 1999. Additional Information to the Report "Compressor Testing Facility", Uncertainty calculation. Lappeenranta, Lappeenranta University of Technology, Department of Energy Technology, Laboratory of Fluid Dynamics. Internal memo.

Schlichting, H. 1979. Boundary-Layer Theory. Kestin, J. (transl.) 7th ed. New York, McGraw-Hill. 817 p.

Siikonen, T. 1995. An Application of Roe's Flux Difference Splitting for the $k-\varepsilon$ Turbulence Model. International Journal for Numerical Methods in Fluids. Vol. 21, 1995, pp. 1017-1039.

Siikonen, T. 1998. FINFLO User Guide, Version 3.0. Helsinki, Helsinki University of Technology, Laboratory of Applied Thermodynamics. 63 p.

Siikonen, T. and Pan, H. 1992. An Application of Roe's Method for the Simulation of Viscous Flow in Turbomachinery. In: Hirsch et al. (eds) Computational Fluid Dynamics '92, Vol. 2, Proceedings of the First European Computational Fluid Dynamics Conference, Brussels, Sep. 7 - 11, 1992. Elsevier Science Publishers B.V. pp. 635 - 641.

Sorokes, J. M., Borer, J. C. and Koch, J. M. 1998. Investigation of the Circumferential Static Pressure Non-Uniformity Caused by a Centrifugal Compressor Discharge Volute. ASME Paper No. 98-GT-326.

Speziale, C., Sarkar, S. and Gatski, T. 1991. Modelling the Pressure-Strain Correlation of Turbulence: an Invariant Dynamical Systems Approach. Journal of Fluid Mechanics. Vol. 227, pp. 245 - 272.

Stepanoff, A. J. 1957. Centrifugal and Axial Flow Pumps, Theory, Design and Application. 2nd ed., New York, John Wiley & Sons Ltd. 462 p.

Stiefel, W. 1972. Experiences in the Development of Radial Compressors. Von Karman Institute for Fluid Dynamics, Lecture Series 50: Advanced Radial Compressors, May 15 - 19, 1972.

Turunen-Saaresti, T. 2001. Radiaalikompressorin spiraalivirtauksen numeerinen mallinnus (in Finnish), (Numerical Simulation of the Flow in the Volute of the Centrifugal Compressor). Lappeenranta, Lappeenranta University of Technology, Department of Energy Technology, Master's Thesis. 86 p.

Van den Braembussche, R. and Hande, B. M. 1990. Experimental and Theoretical Study of the Swirling Flow in Centrifugal Compressor Volutes. Transactions of the ASME, Journal of Turbomachinery. Vol. 112, Jan. 1990, pp. 38 - 43.

Van den Braembussche, R., Ayder, E., Hagelstein, D., Rautenberg, M. and Keiper, R. 1999. Improved Model for the Design and Analysis of Centrifugal Compressor Volutes. Transactions of the ASME, Journal of Turbomachinery. Vol. 121, July 1999, pp. 619 - 625.

VDI 2041. 1991. Durchflumessung mit Drosselgeraten, Blenden und Dusen fur Berondere Anwendungen. (Measurement of Fluid Flow with Primary Devices, Orifice Plates and Nozzles for Special Applications). Verein Deutscher Ingenieure. 24 p.

VDI 2045, Part 1. 1993. Abnahme- und Leistungsversuche an Verdichtern, Versuchsdurchfuhrung und Garantievergleich. (Acceptance and Performance Tests on Turbo Compressors and Displacement Compressors, Test Procedure and Comparison with Guaranteed Values). Verein Deutscher Ingenieure. 80 p.

VDI 2045, Part 2. 1993. Abnahme- und Leistungsversuche an Verdichtern, Grundlagen und Beispiele. (Acceptance and Performance Tests on Turbo Compressors and Displacement Compressors, Theory and Examples). Verein Deutscher Ingenieure. 78 p.

Weber, C. R. and Koronowski, M. E. 1986. Meanline Performance Prediction of Volutes in Centrifugal Compressors. ASME Paper No. 86-GT-216.

Wesche, W. 1987. Measurements on the Volute Casing of a Centrifugal Pump. World Pumps. Oct. 1987, pp. 321 - 324.

Whitfield, A. and Roberts, D. V. 1983. Alternative Vaneless Diffusers and Collecting Volute for Turbocharger Compressors. ASME Paper No. 83-GT-32.

Yadav, R. and Yahya, S. M. 1980. Flow Visualisation Studies and the Effect of Tongue Area on the Performance of Volute Casings of Centrifugal Machines. International Journal of Mechanical Sciences. Vol. 22, No. 10, Oct. 1980, pp. 651 - 660.

Young, M. Y. 1992. Internal Performance Audit of a Highly Backswept 91 mm Centrifugal Turbocharger Compressor. Presented at SAE International Congress and Exposition, Detroit, USA, Feb. 24 - 28, 1992. SAE Technical Paper Series, Paper No. 9200043.

INSTRUCTIONS FOR USE:

Cobra Probes

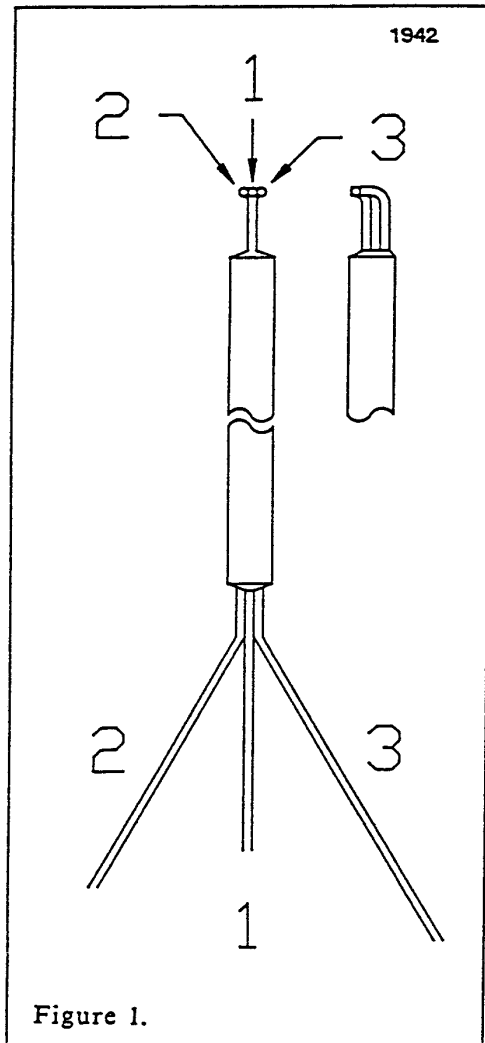


Figure 1.

Cobra probes are assembled as shown in Figure 1. The pneumatic connections are 1/16 inch diameter tubing for use with 0.0625 inch I.D. nylon tubing. The lengths of the connection tubes are set according to tap number. The shortest tube is tap 1, the center tap. The mid-length is tap 2, the left tap. The longest tube is tap 3, the right tap. Calibrations provided are valid for Mach numbers through 0.90. Calibrations are provided for the functions of $(p_1 - p_2)/p_0$ and p_1/p_0 vs. p/p_0 for each individual probe.

The probe is to be clamped in the collet of the manual traverse mechanism. Simultaneous measurements are to be made of p_1 , $(p_1 - p_2)$ and $(p_2 - p_3)$. The sensitivity of the $(p_2 - p_3)$ measurement device must be 7 N/m². The probe must be "nulled" before use.

The procedure for nulling is as follows:

Mount the traverse assembly such that the probe is centered in a good jet flow of Mach \approx 0.5. The probe should be turned into the flow until the pressure $(p_2 - p_3)$ is reduced to less than ($<$) 10 N/m². The probe holder is then fixed in place and the rotary scale of the traverser is then set at 0.0°.

The procedure for use is as follows:

Insert the probe into the flow passage with the traverser mounted appropriately. Position the probe head in the flow passage as desired. Rotate the probe into the direction of flow until $(p_2 - p_3) < 10$ N/m². Read the flow yaw angle (α)

from the rotary scale and pressures p_1 and $(p_1 - p_2)$. p_0 and p (shown in the calibration data sheets as p_t and p_s , respectively), local total and static pressures, can then be calculated, by applying the appropriate calibration for the probe in use. Note that Gracey et al. indicate that a probe of this type has a pitch (γ) acceptance angle of $\pm 20^\circ$. The pitch angle is orthogonal to the yaw angle and cannot be measured with a 3-hole cobra probe.

REFERENCE:

W. Gracey, W. Letko, and W. R. Russell, "Wind-Tunnel Investigation of a Number of Total-Pressure Tubes at High Angles of Attack," NACA TN 2331, Apr. 1951.

APPENDIX A Calibration documents for the Cobra-probe

10/20/98

4555-1a.xls

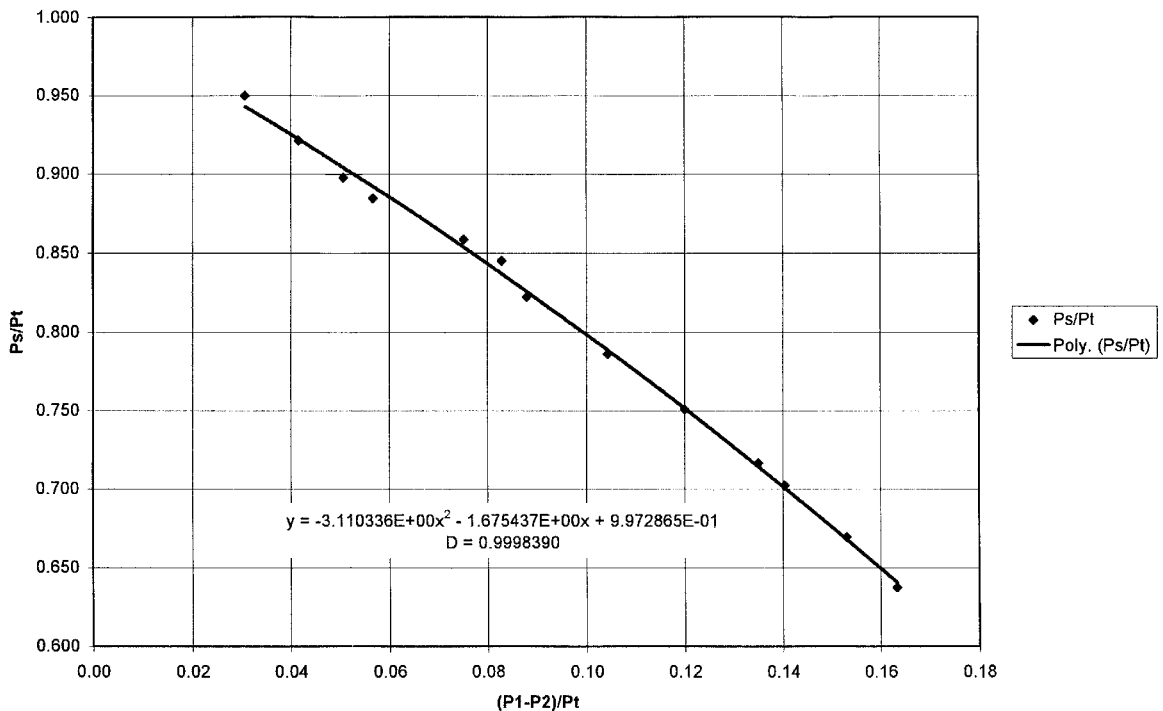
Pt (Psi)	Ps (Psi)	P1-P2 (Psi)	P1 (Psi)	Pt-Ps (Psi)	Ps/Pt	(P1-P2)/Pt	P1/Pt
14.8936065	14.1436065	0.4580000	14.8926065	0.7500000	0.9496428	0.0307515	0.9999329
15.1866065	13.9896065	0.6320000	15.1836065	1.1970000	0.9211805	0.0416156	0.9998025
15.4286065	13.8556065	0.7820000	15.4106065	1.5730000	0.8980465	0.0506851	0.9988333
15.6156065	13.8126065	0.8860000	15.6176065	1.8030000	0.8845386	0.0567381	1.0001281
15.9176065	13.6666065	1.1960000	15.9136065	2.2510000	0.8585843	0.0751369	0.9997487
16.1036065	13.6106065	1.3340000	16.1086065	2.4930000	0.8451900	0.0828386	1.0003105
16.4086065	13.4956065	1.4430000	16.4306065	2.9130000	0.8224712	0.0879417	1.0013408
16.8996065	13.2856065	1.7630000	16.9096065	3.6140000	0.7861489	0.1043220	1.0005917
17.4146065	13.0756065	2.0890000	17.4086065	4.3390000	0.7508413	0.1199568	0.9996555
17.9536065	12.8676065	2.4230000	17.9506065	5.0860000	0.7167143	0.1349590	0.9998329
18.2356065	12.8126065	2.5600000	18.2036065	5.4230000	0.7026148	0.1403847	0.9982452
18.8256065	12.6056065	2.8800000	18.8256065	6.2200000	0.6695990	0.1529831	1.0000000
19.4156065	12.3756065	3.1700000	19.4056065	7.0400000	0.6374051	0.1632707	0.9994850

10/20/98

4555-1a.xls

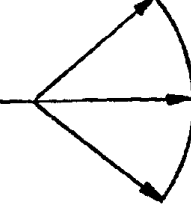
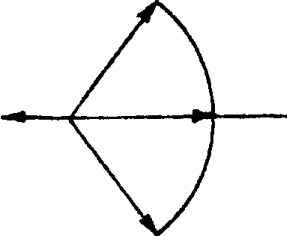
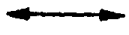
y = -3.110336E+00x ² - 1.675437E+00x + 9.972865E-01									
(P1-P2)/Pt	Ps/Pt	Order	Coeff.	corr.	Error	% Error	Bad (P1-P2)/Pt	Bad Ps/Pt?	
0.0307515	0.9496428	0.0000000	0.9972865	0.9428231	0.0068197	0.7181367			
0.0416156	0.9211805	1.0000000	-1.6754370	0.9221755	-0.0009949	-0.1080073			
0.0506851	0.8980465	2.0000000	-3.1103360	0.9043765	-0.0063300	-0.7048578			
0.0567381	0.8845386	3.0000000	0.0000000	0.8922125	-0.0076740	-0.8675653			
0.0751369	0.8585843	4.0000000	0.0000000	0.8538397	0.0047445	0.5525993			
0.0828386	0.8451900	5.0000000	0.0000000	0.8371518	0.0080381	0.9510449			
0.0879417	0.8224712	6.0000000	0.0000000	0.8258913	-0.0034201	-0.4158288			
0.1043220	0.7861489			0.7886516	-0.0025028	-0.3183574			
0.1199568	0.7508413	D=	0.9998390	0.7515499	-0.0007086	-0.0943697			
0.1349590	0.7167143	(This is the average of P1/Pt)		0.7145199	0.0021944	0.3061805			
0.1403847	0.7026148			0.7007827	0.0018321	0.2607475			
0.1529831	0.6695990			0.6681791	0.0014198	0.2120412			
0.1632707	0.6374051			0.6408235	-0.0034184	-0.5362932			

Cobra Probe Calibration



Yadav and Yahya (1980) present the following guidelines for the interpretation of the surface flow visualisation tufts.

Flow regions as interpreted from wool tuft movements. According to Moore and Kline[1]

Tuft pattern	Symbol	Flow region—Description
	S	Steady turbulent flow—tuft points downstream with only small amplitude oscillations.
	U	Unsteady flow—tuft points downstream with medium amplitude oscillations.
	T _I	Incipient transitory stall—tuft points downstream with large amplitude oscillations (Tuft is on verge of pointing upstream).
	IT	Intermittent transitory stall—tuft points upstream for short periods of time and when pointing downstream, displays large amplitude oscillations.
	T	Transitory stall—tuft points upstream for approximately the same periods of time as it points downstream.
	F	Fixed stall—tuft points upstream for long periods of time.

[1] refers to Moore and Kline (1958)

APPENDIX C Grid size in the different blocks

1

Table C.1. The number of computational cells in each block on the grid levels 1, 2 and 3.

Block	Level 1				Level 2				Level 3			
	I	J	K	total	I	J	K	total	I	J	K	total
1	32	32	80	81 920	16	16	40	10 240	8	8	20	1 280
2	32	32	80	81 920	16	16	40	10 240	8	8	20	1 280
3	32	32	80	81 920	16	16	40	10 240	8	8	20	1 280
4	32	32	80	81 920	16	16	40	10 240	8	8	20	1 280
5	32	32	80	81 920	16	16	40	10 240	8	8	20	1 280
6	32	32	80	81 920	16	16	40	10 240	8	8	20	1 280
7	32	32	80	81 920	16	16	40	10 240	8	8	20	1 280
8	24	32	448	344 064	12	16	224	43 008	6	8	112	5 376
9	16	16	448	114 688	8	8	224	14 336	4	4	112	1 792
10	24	32	448	344 064	12	16	224	43 008	6	8	112	5 376
11	8	16	448	57 344	4	8	224	7 168	2	4	112	896
12	32	16	448	229 376	16	8	224	28 672	8	4	112	3 584
13	32	16	448	229 376	16	8	224	28 672	8	4	112	3 584
14	32	32	64	65 536	16	16	32	8 192	8	8	16	1 024
15	32	32	64	65 536	16	16	32	8 192	8	8	16	1 024
16	32	32	64	65 536	16	16	32	8 192	8	8	16	1 024
17	32	32	64	65 536	16	16	32	8 192	8	8	16	1 024
18	32	32	64	65 536	16	16	32	8 192	8	8	16	1 024
19	32	32	64	65 536	16	16	32	8 192	8	8	16	1 024
20	32	32	64	65 536	16	16	32	8 192	8	8	16	1 024
21	32	32	64	65 536	16	16	32	8 192	8	8	16	1 024
22	32	32	64	65 536	16	16	32	8 192	8	8	16	1 024
23	32	32	64	65 536	16	16	32	8 192	8	8	16	1 024
24	32	32	64	65 536	16	16	32	8 192	8	8	16	1 024
25	32	32	64	65 536	16	16	32	8 192	8	8	16	1 024
26	32	32	64	65 536	16	16	32	8 192	8	8	16	1 024
27	32	32	64	65 536	16	16	32	8 192	8	8	16	1 024
28	560	32	40	716 800	280	16	20	89 600	140	8	10	11 200
29	560	32	40	716 800	280	16	20	89 600	140	8	10	11 200
30	32	32	496	507 904	16	16	248	63 488	8	8	124	7 936
31	32	32	96	98 304	16	16	48	12 288	8	8	24	1 536
32	32	32	32	32 768	16	16	16	4 096	8	8	8	512
33	128	16	32	65 536	64	8	16	8 192	32	4	8	1 024
	total 4 947 968				total 618 496				total 77 312			

73. LAURONEN, JARI. Spare part management of an electricity distribution network. 1998. 130 s. Diss.
74. PYRHÖNEN, OLLI. Analysis and control of excitation, field weakening and stability in direct torque controlled electrically excited synchronous motor drives. 1998. 109 s. Diss.
- ACTA UNIVERSITATIS LAPPEENRANTAENSIS 1999 -
75. SAARNIO, ANTTI. Choice of strategic technology investment - case of pulp production technology. 1999. 225 s. Diss.
76. MATTILA, HEIKKI. Merchandising strategies and retail performance for seasonal fashion products. 1999. 219 s. Diss.
77. KAUKONEN, JUKKA. Salient pole synchronous machine modelling in an industrial direct torque controlled drive application. 1999. 138 s. Diss.
78. MÄNTTÄRI, MIKA. Fouling management and retention in nanofiltration of integrated paper mill effluents. 1999. U.s. Diss.
79. NIEMELÄ, MARKKU. Position sensorless electrically excited synchronous motor drive for industrial use based on direct flux linkage and torque control. 1999. 142 s. Diss.
80. LEPPÄJÄRVI, SEPPO. Image segmentation and analysis for automatic color correction. 1999. U.s. Diss.
81. HAUTA-KASARI, MARKKU. Computational techniques for spectral image analysis. 1999. U.s. Diss.
82. FRYDRYCH, MICHAEL. Color vision system based on bacteriorhodopsin. 1999. 87 s. Diss.
83. MAKKONEN, MATTI. Size effect and notch size effect in metal fatigue. 1999. 93 s., liitt. Diss.
84. 7th NOLAMP Conference. 7th Nordic Conference in Laser Processing of Materials. Ed. by Veli Kujanpää and John Ion. Vol. I-II. 1999. 559 s.
85. Welding Conference LUT JOIN'99. International Conference on Efficient Welding in Industrial Applications (ICEWIA). Ed. by Jukka Martikainen and Harri Eskelinen. 1999. 418 s.
86. PARTANEN, TEUVO. On the application of beam on elastic foundation theory to the analysis of stiffened plate strips. 1999. 102 s. Diss.
87. ESKELINEN, HARRI. Tuning the design procedures for laser processed microwave mechanics. 1999. 172 s. Diss.
88. ROUVINEN, ASKO. Use of neural networks in robot positioning of large flexible redundant manipulators. 1999. 71 s. Diss.
89. MAKKONEN, PASI. Artificially intelligent and adaptive methods for prediction and analysis of superheater fireside corrosion in fluidized bed boilers. 1999. 187 s. Diss.
90. KORTELAJAINEN, JARI. A topological approach to fuzzy sets. 1999. U.s. Diss.
91. SUNDQVIST, SATU. Reaction kinetics and viscosity modelling in the fusion syntheses of Ca- and Ca/Mg-resinates. 1999. U.s. Diss.

92. SALO, JUSSI. Design and analysis of a transversal-flux switched-reluctance-linear-machine pole-pair. 1999. 156 s. Diss.
93. NERG, JANNE. Numerical modelling and design of static induction heating coils. 2000. 86 s. Diss.
94. VARTIAINEN, MIKA. Welding time models for cost calculations in the early stages of the design process. 2000. 89 s., liitt. Diss.
95. JERNSTRÖM, EEVA. Assessing the technical competitiveness of printing papers. 2000. 159 s., liitt. Diss.
96. VESTERINEN, PETRI. On effort estimation in software projects. 2000. U.s. Diss.
97. LUUKKO, JULIUS. Direct torque control of permanent magnet synchronous machines – analysis and implementation. 2000. 172 s. Diss.
98. JOKINEN, ARTO. Lobbying as a part of business management. 2000. 244 s. Diss.
99. JÄÄSKELÄINEN, EDUARD. The role of surfactant properties of extractants in hydrometallurgical liquid-liquid extraction processes. 2000. U.s. Diss.
100. Proceedings of 3rd Finnish-French Colloquium on Nuclear Power Plant Safety. 2000. 118 s.
101. TANSKANEN, PASI. The evolutionary structural optimization (ESO) method: theoretical aspects and the modified evolutionary structural optimization (MESO) method. 2000. 67 s., liitt. Diss.
102. JERNSTRÖM, PETTERI. The effects of real-time control of welding parameters on weld quality in plasma arc keyhole welding. 2000. 69 s., liitt. Diss.
103. KAARNA, ARTO. Multispectral image compression using the wavelet transform. 2000. U.s. Diss.
104. KOTONEN, ULLA. Rahavirta-analysit, erityisesti kassavirtalaskelma, kunnan talouden ohjauksen apuvälineenä. 2000. 209 s., liitt. Väitösk.
105. VARIS, JUHA. A novel procedure for establishing clinching parameters for high strength steel sheet. 2000. 84 s., liitt. Diss.
106. PÄTÄRI, EERO. Essays on portfolio performance measurement. 2000. 201 s. Diss.
107. SANDSTRÖM, JAANA. Cost information in engineering design – potentials and limitations of activity-based costing. 2001. 143 s., liitt. Diss.
108. TOIVANEN, JOUKO. Balanced Scorecardin implementointi ja käytön nykytila Suomessa. 2001. 216 s. Väitösk.
110. Proceedings of Fifth International Seminar on Horizontal Steam Generators. Ed. by Juhani Vihavainen. 2001. 255 s.
112. SILVENTOINEN, PERTTI. Electromagnetic compatibility and EMC-measurements in DC-voltage link converters. 2001. 115 s. Diss.
113. TERVONEN, ANTERO. Laadun kehittäminen suomalaisissa yrityksissä. 2001. 206 s. Väitösk.
115. HORTTANAINEN, MIKA. Propagation of the ignition front against airflow in packed beds of wood particles. 2001. U.s. Diss.
117. WU, HUAPENG. Analysis, design and control of a hydraulically driven parallel robot manipulator. 2001. U.s. Diss.